Symmetry and Topology at the Metasurface

Mark Lawrence

M.Sci

A thesis submitted to The
University of Birmingham
for the degree of
Doctor of Philosophy

Metamaterials Research Centre
School of Physics and Astronomy
College of Engineering and Physical Sciences
The University of Birmingham

May 2015

Abstract

Since the metamaterials ethos of geometry over chemistry was first conceived at the end of the last century, a great deal of effort has been directed towards the conceptual, computational and experimental development of myriad effective electromagnetic media. Having been greatly successful, the fruits of this labour are now ripe for use within new and exciting applications. However, instead of simply coming up with engineering solutions, here, we take inspiration from another discipline which centres on the physics of wave behaviour in complex environments, namely Quantum mechanics, to explore novel metamaterial systems. In particular, we exploit the possibility of independently controlling the elements of an effective polarisability matrix to reveal unique polarisation based phenomena.

Firstly, by employing resonant "meta-atoms" to selectively absorb specific polarisation states of THz radiation, while tuning the polarisation conversion efficiency via near-field coupling, spontaneous *Parity Time* symmetry breaking has been observed in polarisation space for the first time. Measurements have been carried in the THz frequency regime using THz-Time Domain Spectroscopy. Through this investigation we also reveal that anisotropic material as well radiative loss can be highly useful for tailoring the response of resonant metamaterials.

Secondly, the possibility of achieving a topologically non-trivial phase within an effectively homogeneous photonic medium is discussed. Originating from the inherent spin-orbit interaction for light, three dimensional metamaterials with chirality and hyperbolicity are shown to possess equal-frequency surfaces with non-zero topological indices. As a result, an interface formed between this and a trivial medium, such as a vacuum, supports robust

surface waves which are unidirectional and immune to backscattering. Building on the effective medium calculations, our predictions are confirmed by numerical studies of realistic meta-structures. These developments are therefore expected to represent a new direction for theoretical and experimental research into topological photonics.

Publications

M. Lawrence, S. Zhang, “A family of polarisation phase transitions in chiral *PT* symmetric metasurfaces” (in preparation)

M. Lawrence, T.-T Kim, M. Kenney, S. Zhang, “Observation of a polarisation phase singularity near metasurface exceptional point” (in preparation)

W. Gao*, **M. Lawrence***, B. Yang, F. Liu, F. Fang, B. Béri, J. Li, and S. Zhang, (* equally contributed first authors) “Topological photonic phase in chiral hyperbolic metamaterials”, ***Physical Review Letters***, 114, 037402 (2015)

M. Lawrence, N. Xu, X. Zhang, L. Cong, J. Han, W. Zhang & S. Zhang, "Manifestation of *PT* symmetry breaking in polarization space with terahertz metasurfaces", ***Physical Review Letters***, 113, 093901 (2014)

Declaration

This thesis, which documents the culmination of my own research, has been written entirely by myself, with every effort being made to accurately reference the work of others where appropriate. New results are contained within chapters three and four. Although I played a highly significant role, the corresponding investigations were of a collaborative nature.

My personal contribution to the work presented in chapter three was to conceive of anisotropic *Parity Time* symmetry, design the various metasurfaces, perform the THz-TDS transmission measurements shown in section 3.6 and analyse all of the measured data. The samples used in section 3.4 were fabricated by Ningning Xu at Oklahoma state university, under the supervision of Professor Weili Zhang, and measured by Xueqian Zhang and Longqing Cong at Tianjin university, under the supervision of Professors Weili Zhang and Jiaguang Han. The experiment discussed in section 3.6 was performed here in Birmingham with the sample being fabricated by Mitchel Kenney and measured by myself and Teun-Teun Kim.

In chapter four, Wenlong Gao and Biao Yang numerically solved for the dispersion of the surface waves shown in Figure 4.6 and Figure 4.8, while Fu Liu and Jensen Li produced Figure 4.7 by performing simulations using Comsol Multiphysics, all whilst residing at The University of Birmingham. I was responsible for analysing the topological origin of the surface behaviour and calculating the bulk Chern numbers, as well as designing the realistic topological metamaterial structures discussed in section 4.5, with results revealed in Figure 4.10 and Figure 4.11.

Acknowledgements

First and foremost I would like to thank Professor Shuang Zhang for allowing me to join him on the ground floor of metamaterials research at Birmingham. The wealth of ideas and suggestions in the early days was inspirational, if at times a little intimidating, and definitely made up for the lack of other group members. I am also grateful to Lingling for the many useful discussions had when I was getting to grips with the finer details of photonics and electromagnetic simulations. Towards the end of my time in the group afternoon coffee trips, or hot chocolate with cream and curls in my case, helped to relieve the stress of writing and so I would like to thank all the members of the coffee club, Teun-Teun, Guixin, Yao-Ting, Biao, Wenlong and Qinghua.

I am indebted to all of my friends and family for their love and support, not to mention the much needed rest bite from research, over the last four years. My parents most notably for enabling me to undertake such a journey due to their balanced approach to parenting, mum the eternal optimist and dad keeping me grounded by constantly reminding me that hard work and not innate ability is responsible for my previous achievements. Last, but definitely not least, I thank Caitlin for being such an amazing girlfriend and putting up with the third member in our relationship.

I also give thanks to the EPSRC and The University of Birmingham for providing the funding and facilities necessary to carry out the work presented in this thesis.

Contents

List of Figures

Chapter 1: Introduction

1.1: Background and Motivation

Scientific revolutions are often born out of a realisation that seemingly disparate phenomena are in fact intimately connected. Quantum mechanics is a prime example of this. By the start of the 20th century, thanks to the likes of Young, Fresnel and Thomson, the existence of light waves and negatively charged particles, known as electrons, had been firmly established. However, around this time physicists became troubled by certain phenomena involving the interaction between these fundamental excitations which would ultimately challenge their preconceptions. In a remarkable twist, great minds including Plank, Bohr and Einstein showed that a number of observations including discrete atomic spectra and the photoelectric effect could only be explained if light could also be made up of particles, known as photons, and matter were able to behave as a wave[*1*]. This mysterious insight lies at the heart of modern physics, chemistry and even biology. One area in which quantum mechanics has had a huge impact is condensed matter physics. Unlike photons, electrons spend most of their time bound within materials. When introducing wave behaviour to the description of such systems exciting properties including superconductivity and quantum tunnelling emerge.

More recently, electromagnetism has undergone its own transformation. Exploiting the scale invariance of Maxwell's equations, electrical engineering design principles have been combined with geometrical optics to form the field of metamaterials. John Pendry is often credited with proposing the general idea via two papers, one published in 1996 and the other in 1999, that if artificial elements are arranged on a subwavelength scale, collectively they would mimic the response of atoms within naturally occurring solids[*2*, *3*]. As a result,

these man-made materials can be described in terms of effective parameters such as an electric permittivity, a magnetic permeability and a refractive index. Importantly, these parameters can be controlled via the geometry of the elements used rather than being limited by the constitutive materials available, dramatically increasing the range of values that can be achieved. Interest in this new field exploded when D. R. Smith used Pendry's design principle to realise the first medium to simultaneously exhibit a negative permittivity and permeability[*4*]. The reason for this excitement was an earlier theoretical prediction by Victor Veselago, which was ignored at the time as it was regarded to be unphysical, revealing that such a material should be described as having a negative refractive index[*5*]. This simple result which implies that the corresponding waves possess group and phase velocities pointing in opposite directions can also be shown to produce remarkable phenomena including negative refraction[*6*], negative radiation pressure[*7*], backward Cerenkov radiation[*8*] and even super resolution imaging[*9*]. Due to the enormous amount of interest that the field has received since then, metamaterials research is just beginning to reach maturity, providing a vast array of not just novel but precise methods for manipulating all characteristics of electromagnetic radiation, heralding a new dawn for photonic science. A more thorough account of these developments can be found in section (2.3).

With such an increased level of freedom offered by metamaterials for controlling the behaviour of light waves, it is pertinent to search for interesting ways of harnessing this new power. One option is to look to the wealth of quantum condensed matter phenomena arising from complicated potential energy landscapes. While a number of studies have sought to replicate these potentials using spatially dependent refractive index variations, another intriguing possibility is the application of quantum principles to distinctly photonic behaviour. One such property is polarisation. By representing a uniform beam of light as the superposition of left and right handed circularly polarised waves, *i.e.* waves with

electromagnetic fields rotating in clockwise and anticlockwise directions, the intrinsic nature of the angular momentum carried by the beam is reminiscent of the spin degree of freedom for electrons. Unlike electrons however, the direction of photonic spin is fixed precisely by the linear momentum which will later be shown to have some surprising consequences. By exploring polarisation dependant light propagation with quantum inspired anisotropic metamaterials, we will reveal new physics as well as potentially useful functionalities.

1.2: Overview of Thesis

The main body of this thesis includes three chapters. Firstly, in chapter two, key background information is provided, forming the foundations for the new results presented later in the document. In particular, the physics behind *PT* symmetric and topological quantum problems as well as electromagnetic metamaterial design is outlined. Building on this initial discussion, *PT* symmetric metasurfaces are developed in chapter three with the prediction and experimental observation of polarisations phase transitions and topologically protected spectral singularities explained in detail. Chapter four then deals with the theoretical discovery of a topologically non-trivial phase in chiral hyperbolic metamaterials. While this final part of the thesis describes a purely theoretical study, it is concluded by presenting realistic designs which should allow experimental validation to be carried out in the future.

Chapter 2: Fundamental Concepts

The aim of this thesis is to explore novel polarisation based wave behaviour originating from anisotropic metamaterial designs inspired by quantum theory. Before embarking on such an endeavour, it is important to set the scene and present the physical and mathematical basis for this possibility. To start we will therefore discuss some key concepts in quantum mechanics, classical electromagnetism and metamaterials.

2.1: Symmetry and Topology in Quantum Mechanics

In this section, we introduce a few basic mathematical concepts that underpin some fairly recent developments in quantum physics. Specifically, our focus is on simple, non-interacting problems which depend on a set of parameters. By tracking the solutions of such systems while varying those parameters, surprising results can be revealed. It is these results that we wish to exploit in the context of photonics and so the information given here will act to guide the work presented in chapters three and four.

2.1.1: Schrödinger's Equation

In 1925 Erwin Schrödinger brought about a scientific paradigm shift when he postulated that the dynamics of microscopic objects are governed by the following partial differential equation[*10*].

$$i\hbar\frac{\partial}{\partial t}\Psi(\boldsymbol{r},t)=\left[-\frac{\hbar^2}{2m}\boldsymbol{\nabla}^2+V(\boldsymbol{r},t)\right]\Psi(\boldsymbol{r},t) \qquad [2.1]$$

Schrödinger's equation describes the energetic exchange between a potential energy landscape $V(\boldsymbol{r},t)$ and a space-time dependant field $\Psi(\boldsymbol{r},t)$ and, crucially, supports bound and travelling wave solutions. Counterintuitively, $\Psi(\boldsymbol{r},t)$ represents just a single particle; a fact confirmed by experimental observations which reveal that one can only ever infer its existence from repeated measurements rather than probing it directly from a single measurement. This seemingly paradoxical result, commonly referred to as wave-particle duality, is often resolved by interpreting $|\Psi(\boldsymbol{r},t)|^2$ as the probability density for observing the particle at some point in space and time in any given measurement[*10*]. This new approach has revolutionised the physical sciences and successfully explained a number of key phenomena, including the discretisation of atomic emission spectra, variation in conduction for metals and semiconductors and even the lifetime of stars.

Without explicit time dependence, $V(\boldsymbol{r},t) \rightarrow V(\boldsymbol{r})$, solutions take the form $\Psi_n(\boldsymbol{r},t) = e^{-\frac{iE_nt}{\hbar}}\psi_n(\boldsymbol{r})$, where E_n is the mode energy which can be found by solving the eigenvalue problem $E_n\psi_n(\boldsymbol{r}) = \left[-\frac{\hbar^2}{2m}\boldsymbol{\nabla}^2 + V(\boldsymbol{r})\right]\psi_n(\boldsymbol{r}) \equiv \widehat{\mathcal{H}}\psi_n(\boldsymbol{r})$. These are known as stationary states as their probability distributions remain fixed in time. While only strictly applicable to static systems, time independent solutions can also be used more generally, in conjunction with perturbative methods, for approximating the interaction between different sub-systems or the dynamics of a particle lying in an evolving potential[*10*]. As well as the Hamiltonian $\widehat{\mathcal{H}}$, which represents the energy of a quantum object, other operators, such as the linear or angular momentum operators, can extract further information. However, the probabilistic nature of the theory usually restricts physically meaningful operations to those that are Hermitian, or self-adjoint, guaranteeing a complete set of eigenvectors with real eigenvalues. Importantly, the fact that the wavefunction cannot be observed directly also provides a freedom to choose its phase arbitrarily. This so called gauge invariance places further limits

on the information that can be gleaned from quantum measurements, as any property that varies under the transformation $\psi_n(\boldsymbol{r}) \rightarrow e^{i\varphi}\psi_n(\boldsymbol{r})$ is not physically accessible.

2.1.2: Parametric Evolution and Geometric Phase

In 1984, Michael Berry decided to investigate the behaviour of a quantum system undergoing slow temporal variation[*11*]. Rather than solving Eq.2.1 directly, Berry described the problem in terms of a Hamiltonian $\widehat{\mathcal{H}}(\boldsymbol{R})$, dependant on a set of parameters $\boldsymbol{R} = (R_1(t), R_2(t), R_3(t) \dots)$ that change with time. For sufficiently slow changes[*], the adiabatic theorem guarantees that an initial stationary state $|n(\boldsymbol{R}(t=0))\rangle$ of $\widehat{\mathcal{H}}(\boldsymbol{R}(t=0))$ will remain an eigenstate of the instantaneous $\widehat{\mathcal{H}}$ for all future *t*. The general solution can then be written as

$$|\Psi(t)\rangle = e^{i\gamma_n(t)} e^{-\frac{i}{\hbar}\int_0^t E_n(\boldsymbol{R}(t'))dt'} |n(\boldsymbol{R}(t))\rangle, \qquad [2.2]$$

where the phase consists of both the usual dynamic contribution plus an extra term originating from the changing environment. By inserting this wavefunction into Schrödinger's equation, it can be shown that

$$\gamma_n = i \int \langle n(\boldsymbol{R}) | \boldsymbol{\nabla}_{\boldsymbol{R}} n(\boldsymbol{R}) \rangle \cdot d\boldsymbol{R}. \qquad [2.3]$$

Berry's insight was to notice that, while not generally true, γ_n is gauge invariant (modulo 2π), and therefore physically observable, for a system which returns to its initial state after

[*] The limit on how slow changes to the Hamiltonian need to be in order for the adiabatic theorem to apply can be determined by inspecting the first order corrections to the time dependent wavefunction, which are proportional to $\langle n' | \partial/\partial t | n \rangle / (E_n - E_{n'})$, where $n' \neq n$[*12*]. Here we can see that the rate of change of the initial eigenstate, and therefore the Hamiltonian, needs to be small compared to the separation from neighbouring energy levels. It is also then obvious that the adiabatic theorem necessarily breaks down if states become degenerate.

some time $\boldsymbol{R}(T) = \boldsymbol{R}(0)$[*11*]. Interestingly, the additional phase factor, often called the Berry phase, is entirely geometrical, depending on the path taken through the underlying parameter space rather than the local coordinates *t* or $\boldsymbol{R}$. Physically, a closed loop in Eq.2.3 can be thought of as the interference between two different states, reminiscent of the Aharonov-Bohm effect for particles taking different routes around a solenoid. Here $\boldsymbol{A}_n = i\langle n(\boldsymbol{R})|\boldsymbol{\nabla}_{\boldsymbol{R}} n(\boldsymbol{R})\rangle$, often called the Berry connection, plays the same role as the magnetic vector potential in classical electromagnetism. For $2 \leq \dim(\boldsymbol{R}) \leq 3$ we can take this analogy further by defining $\boldsymbol{\Omega}_n = \boldsymbol{\nabla}_{\boldsymbol{R}} \times \boldsymbol{A}_n$, often called the Berry curvature, which plays the role of an effective magnetic field. Unlike the Berry connection, the Berry curvature is actually local and gauge invariant. Using Stokes's theorem, Eq.2.3 can also then be recast into the gauge invariant form

$$\gamma_n = \int \boldsymbol{\Omega}_n \cdot d\boldsymbol{S}, \qquad [2.4]$$

which represents an effective Gauss's law, relating the Berry phase accumulated around a circuit to the Berry flux threading the enclosed surface.

One particularly important model to which Berry's analysis can be applied is that of two interacting modes, which can be described by the generalised Hermitian Hamiltonian

$$\widehat{\mathcal{H}}(\boldsymbol{R} = (X, Y, Z)) = \frac{1}{2}\begin{bmatrix} Z & X + iY \\ X - iY & -Z \end{bmatrix}. \qquad [2.5]$$

Notable examples of physical systems that can be described by Eq.2.5 include the behaviour of a spin$-\frac{1}{2}$ particle under the influence of a slowly rotating magnetic field and Bloch electrons at the corner of a hexagonal Brillouin zone. After solving for the eigenstates, it can be shown that, in this case, the Berry curvature takes the simple form[*11*]

$$\boldsymbol{\Omega}_n = \pm\frac{\boldsymbol{R}}{2R^3}. \qquad [2.6]$$

Remarkably, this equation describes the field of an effective magnetic monopole sitting at the origin of the parameter space $\boldsymbol{R} = 0$. By looking at the energy eigenvalues of Eq.2.5, $\varepsilon_n = \pm\sqrt{R^2}$, we can see that a diabolic or Dirac type mode degeneracy also exists for $\boldsymbol{R} = 0$. This correspondence between degeneracies and monopole sources of Berry curvature is actually quite general and can be proven by using perturbation theory to derive an alternative form for $\boldsymbol{\Omega}_n$ containing terms which are inversely proportional to the separation between neighbouring energy levels[*12*]. Just as the electric flux through a closed surface in real space depends solely on the number of electrons or protons contained within it, the Berry flux through a closed surface $\boldsymbol{S}_C$ in $\boldsymbol{R}$ is equal to the number of monopole degeneracies bounded by $\boldsymbol{S}_C$, multiplied by 2π. This leads to the definition of the Chern number,

$$C_n = \frac{1}{2\pi}\iint_{S_C} \boldsymbol{\Omega}_n \cdot d\boldsymbol{S}. \qquad [2.7]$$

Known as a topological invariant, C_n can only take on integer values and therefore remains

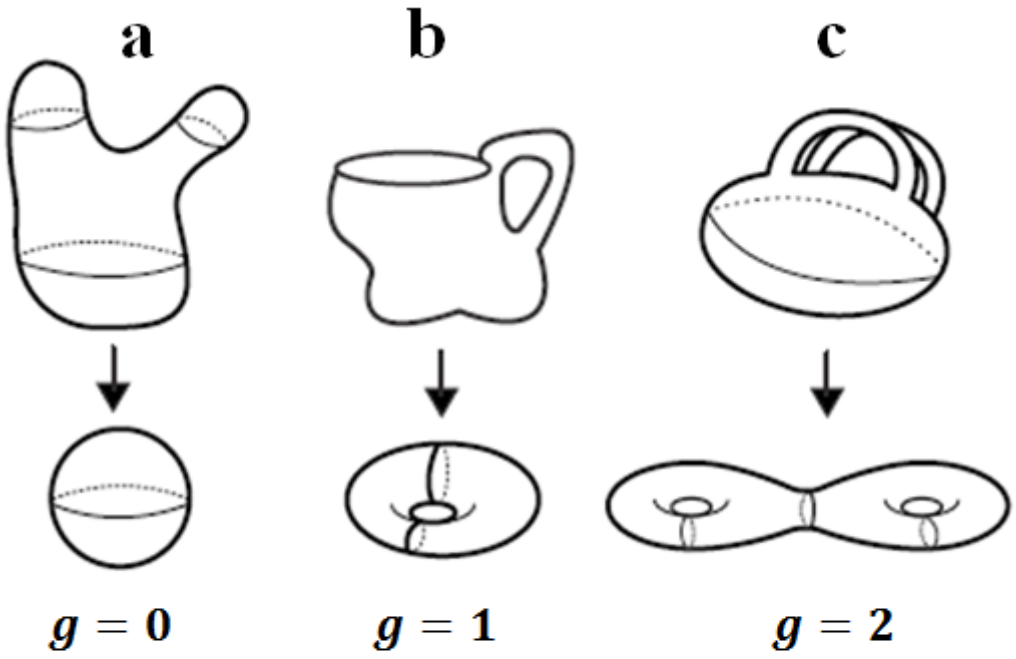

Figure 2.1: Topological characterisation of closed 2D surfaces embedded in 3D space. The genus which counts the number of holes present is a topological invariant. The objects within each sub figure (a, b and c) are topologically equivalent as one can be smoothly deformed into the other, while objects are topologically inequivalent to those in other sub figures as punching a hole is not a smooth transformation[*111*].

invariant under smooth deformations of $\boldsymbol{S}_C$. Cementing the connection between geometry and the concepts outlined throughout this section, Eq.2.7 also closely resembles the Gauss-Bonnet theorem. Through this analogy, C_n plays the same role as the genus which counts the number of holes in a 2D surface embedded in a 3D space. Topological invariance of the genus can be understood very intuitively, as the act of punching a hole through a surface is clearly not smooth.

2.1.3: Non-trivial Topology in Crystals

Having explained the universal properties of parameter dependant Hamiltonians, we now proceed to discuss a specific parametrisation used in condensed matter physics, namely Bloch state crystal momentum, for which topology can have some surprising consequences. The wavefunction of a quantum particle sitting in a time-independent periodic potential $V(\boldsymbol{r}) = V(\boldsymbol{r} + \boldsymbol{a})$ can be written as

$$|\Psi(\boldsymbol{r})\rangle = e^{i\boldsymbol{k}.\boldsymbol{r}}|n(\boldsymbol{r})\rangle, \qquad [2.8]$$

where $|n(\boldsymbol{r})\rangle = |n(\boldsymbol{r} + \boldsymbol{a})\rangle$. The periodic part $|n\rangle$ of the wavefunction obeys the $\boldsymbol{k}$ dependant eigenvalue problem

$$\hat{\mathcal{H}}(\boldsymbol{k})|n(\boldsymbol{k})\rangle = \varepsilon_{n\boldsymbol{k}}|n(\boldsymbol{k})\rangle, \qquad [2.9]$$

with the eigenstates of this equation forming a discrete set of continuous energy bands separated by band gaps[*13*], as illustrated schematically in Figure 2.2b. A particle cannot be transported through the lattice with energies in the band gap. Such problems can therefore be seen to fit nicely within the framework outlined in (2.1.2) with $\boldsymbol{R} \equiv \boldsymbol{k}$. Under the action of a constant, uniform electric field $\boldsymbol{E}$, the particle will be accelerated, corresponding to a variation of $\boldsymbol{k}$ in time, $\frac{\partial \boldsymbol{k}}{\partial t} = -\frac{e}{\hbar}\boldsymbol{E}$. As first pointed out by Zak in 1989, closed parametric loops can be found even in 1D crystals because the periodic boundary condition only allows

for $n(k)$ and $n\left(k+\frac{2\pi}{a}\right)$ to differ by a phase factor $e^{i\gamma_n}$[*14*]. Consequently, one commonly works only in the first Brillouin zone $\left(-\frac{\pi}{a}<k<\frac{\pi}{a}\right)$. This phase γ_n, given by Eq.2.3, is a geometric property of each band and actually attains a topological character when inversion symmetry is present as it is quantized in units of π[*14*].

In two dimensions the situation becomes more interesting as the Berry curvature is well defined. With the Brillouin zone now being represented by a closed toroidal surface each non-degenerate band can be assigned a Chern number C_n which can be calculated using Eq.2.7[*12*]. Importantly, although changes to the potential energy will modify $\varepsilon_{n\boldsymbol{k}}$, the topological invariance of C_n means that it can only change if a band gap is closed. As well as providing a global signature of each ε_n, this has dramatic consequences for the transport

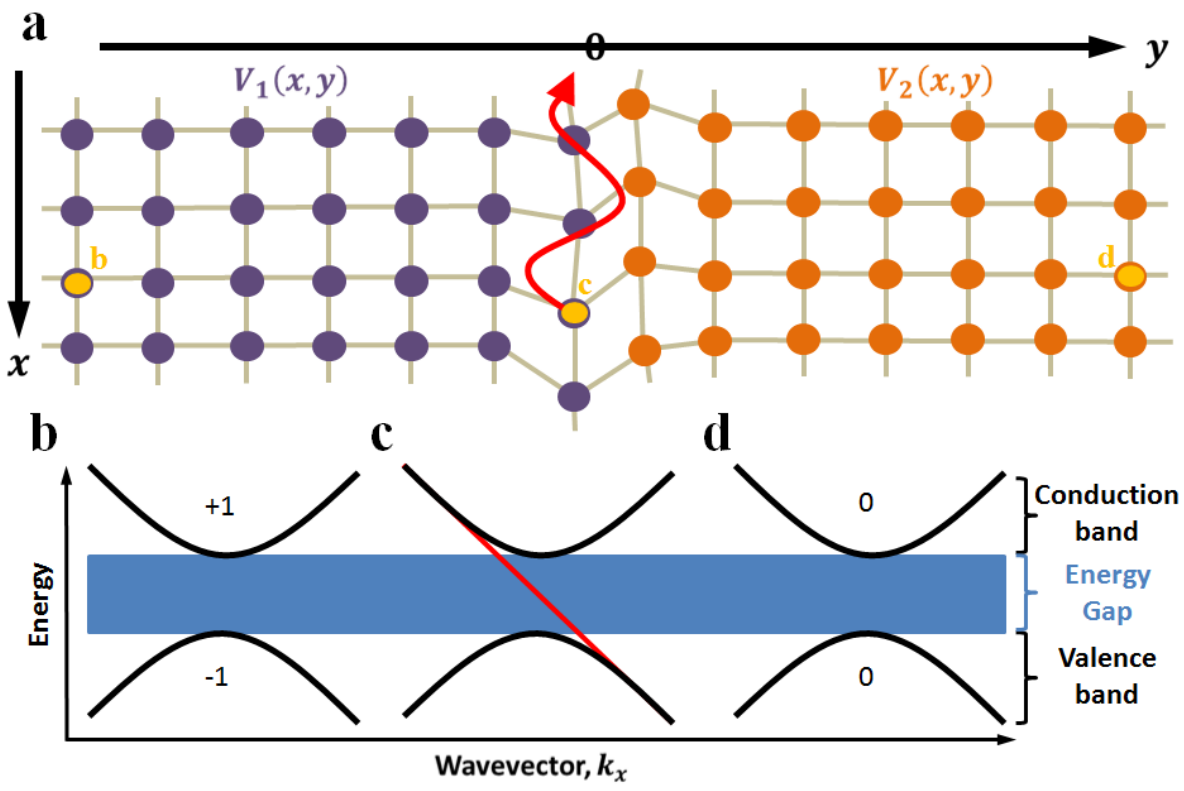

Figure 2.2: Bulk edge correspondence for boundary between topologically distinct 2D crystals. a) Disordered interface between two half-spaces filled with lattice potentials V_1 and V_2. b-d) Band structures for a particle positioned at corresponding coordinates labelled by yellow dotes in subplot(a). As the sum of the Chern numbers below the band gap $\boldsymbol{\Sigma}$ in subplots (b) and (d) differ by one, the gap must close at the interface in the form of a one-way edge state, represented by red curves in (a) and (b).

properties of finite systems. We can see this by considering an interface between two half-spaces described by different Hamiltonians $\widehat{\mathcal{H}}_1$ for $(y < 0)$ and $\widehat{\mathcal{H}}_2$ for $(y > 0)$, as shown in Figure 2.2a. If the corresponding bulk band structures, i.e. the solutions to the infinitely periodic problems $\widehat{\mathcal{H}}_1(\boldsymbol{k})$ and $\widehat{\mathcal{H}}_2(\boldsymbol{k})$, share a complete energy gap one would naturally expect the combination to be fundamentally indistinct from a simple defect within a single periodic space. However, it turns out that propagating modes must exist at such a boundary, unlike a simple defect, when the sum of the Chern numbers associated with energy bands below the gap $\Sigma = \sum_{n<a} C_n$, for a gap between the ath and (a+1)th energy bands, are different for $\widehat{\mathcal{H}}_1(\boldsymbol{k})$ and $\widehat{\mathcal{H}}_2(\boldsymbol{k})$. This can be understood by imagining a particle located in different positions along *y*. Far from the interface $(y \ll -a)$ and $(y \gg a)$, its behaviour will be governed approximately by $\widehat{\mathcal{H}}_1(\boldsymbol{k})$ and $\widehat{\mathcal{H}}_2(\boldsymbol{k})$, respectively. The act of moving the particle from one region of space to the other can then be mapped to a parametric interpolation between the two Hamiltonians, which must be accompanied by a band gap closure if a topological transition occurs[*15*], as illustrated schematically in Figure 2.2. In fact, the exact number of edge states crossing from the lower, or valence, to the upper, or conduction, bulk bands is given by $|\Sigma_2 - \Sigma_1|$. Crucially, as the justification for this so called bulk-boundary correspondence is rooted in *k*-space it is entirely independent of the detailed formation of the interface. Lastly, the requirement for these edge states to connect between different energy levels means that they must disperse asymmetrically within a given band gap, leading to a definite sign for the group velocity $v_g = \nabla_k \omega$. Consequently, the electrons can only travel in one direction and as their existence is guaranteed such boundaries exhibit dissipationless conduction. They are therefore said to be topologically protected against disorder[*15*].

Having discussed the relationship between edge states found between two different media and their bulk Bloch band topology we will now look at some physical systems which

exhibit $\Sigma \neq 0$. The arguments presented above were actually first applied retrospectively to

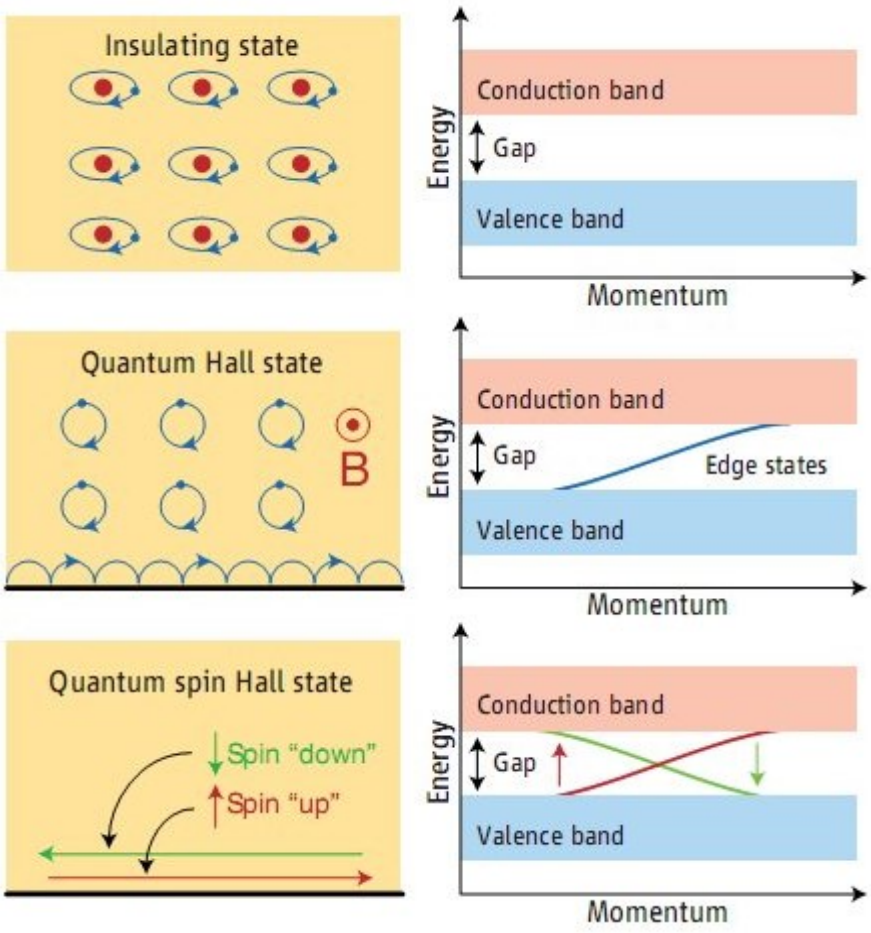

Figure 2.3: Topological electronics. Real space charge dynamics (left) and surface state dispersion (right) for topologically different insulators truncated with a vacuum[*112*].

observations made by von Klitzing et al. in 1980 finding that the conductivity of a 2D semiconductor becomes precisely quantised in units of e^2/h in a strong perpendicular magnetic field[*16*]. By regularising the induced cyclotron orbits on a magnetic Brillouin zone, the dispersionless Landau levels which propagate in the bulk are found to have non-zero Chern numbers. As the existence of one-way edge states is guaranteed by bulk boundary correspondence and the number of electronic states available to conduct on the edge depends only on the Chern numbers of bulk bands below the chemical potential, or Fermi energy, the conductivity can only change, and must change discontinuously, when the Fermi energy crosses a Landau level. The relationship between quantised conductance and topological bulk

indices, later shown to be Chern invariants, was first highlighted by Thouless *et al*[*17*]. This phase is called the integer quantum hall effect (IQHE).

More recently, physicists have asked how systems with topological protection can be created without a magnetic field. The answer turns out to rely on spin. Close to the Brillouin zone corners of graphene, which is a 2D inversion symmetric, honeycomb arrangement of carbon atoms, the electronic dispersion can be approximated by Eq.2.5, with $(X, Y, Z) \equiv (\delta k_x, \delta k_y, 0)$. $Z = 0$ leads to a linear degeneracy at $\delta k_x = \delta k_x = 0$ and is guaranteed by inversion and time reversal symmetries. If $Z \neq 0$ the discussion in (2.1.2) predicts that a gap will open between topologically nontrivial bands. However, breaking inversion symmetry leads to $Z > 0$ and $Z < 0$ for different corners of the Brillouin zone causing the net Berry curvature to vanish. In 2005, Kane and Mele showed that including a spin-orbit interaction can lift each degeneracy with the same *Z*[*18*]. Preservation of time reversal symmetry in this case is manifest in the fact that $Z_{up} = -Z_{down}$. The bulk bands of the two spin sectors can then be thought of as IQHE states with opposite signs for the magnetic field. Consequently, protected, spin polarised edge states are found after truncating the material as long as time reversal symmetry is present, preventing edge spin mixing[*19*]. This phase is therefore known as a quantum spin hall insulator (QSHI). Unfortunately, the gap opened by the spin-orbit interaction within graphene is immeasurably small. However, it was later proposed, and subsequently demonstrated, that by creating a quantum well structure in which a critical thickness is chosen for a HgTe layer sandwiched between two CdTe layers, the normal order of symmetric and antisymmetric, valence and conduction bands describing the propagation of electrons in the remaining two dimensional plane becomes inverted. This leads to the same low energy Hamiltonian as found for graphene except that the much stronger spin orbit coupling in these heavy-atom semiconductors produces a large gap[*20*].

Finally, three dimensional crystals can also exhibit non-trivial topology. By generalising the band inversion argument used for designing the 2D QSHE, a fully gapped 3D bandstructure can be predicted for spin-orbit coupled semiconductors with inversion symmetry[*15*]. The surface states of these so called topological insulators form a single Dirac cone resulting in a spin polarised version of the electronic conduction found in graphene. Unlike graphene, however, the linear degeneracy found in the topological surface dispersion is protected by time-reversal rather than spatial symmetries. Experimental confirmation was provided in 2008 when the surface bands of $Bi_{1-x}Sb_x$ where mapped out using angle resolved

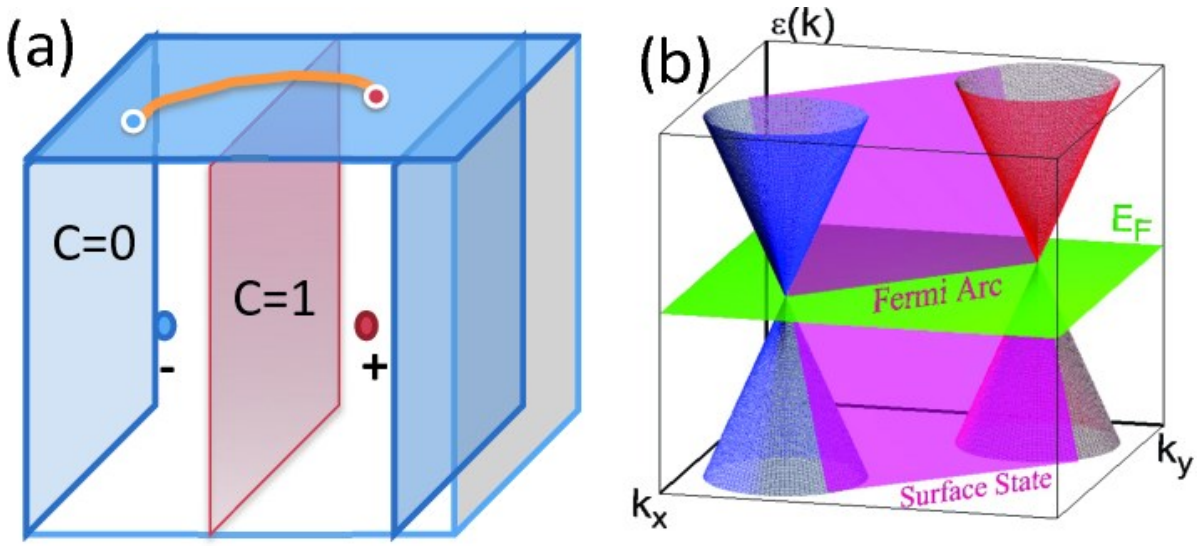

Figure 2.4: Topological semi-metals. a) Chern numbers associated with 2D surfaces in 3D Brullion zone. C=1 if the surface sits between Weyl points of opposite charge, otherwise C=0. Orange curve represents Fermi ark which exists for a truncated system. b) Dispersion corresponding to 'a' with separated points of linear dispersion[*22*].

photoemission spectroscopy[*21*]. Finally, in 3D a truly insulating material isn't strictly necessary. In metallic crystals with strong spin-orbit coupling and broken time reversal or inversion symmetry, degeneracies which disperse linearly in all three directions k_x, k_y and k_z, known as Weyl points, can be found. Unlike Dirac points, these degeneracies cannot be lifted by any perturbation and can only be created in pairs. This robustness originates from the fact that each Weyl point acts as a momentum space monopole, shown in (2.1.2) to possess a quantised topological charge. As a result, Fermi-surfaces which wrap around an

odd number of such *k*-space coordinates can be assigned a nonzero Chern number. In Figure 2.4 bulk boundary correspondence is seen to produce nodes connecting Weyl points with opposite charge, known as Fermi arcs. For particular surface orientations protected surface excitations can be supported[*22–24*].

2.1.4: Non-Hermitian Hamiltonians and Spontaneous *PT* Symmetry Breaking

Despite the great success with which Quantum theory can make predictions, as outlined in section 2.1.1, explanations of certain counterintuitive observations, such as Young's double slit experiment, still rely on a set of mysterious postulates. In this section, we review recent developments which challenge one particular postulate, stating that only eigenvalues of Hermitian operators can be physically measured. Through these endeavours, it has been shown that the full wealth of Quantum analysis can be extended to open or dissipative systems in which energy is able to enter and leave via interactions with the external environment, potentially opening up new directions for experimental study. Of course a complete description of any problem would involve the entire universe which must be closed due to the principle of energy conservation; however, keeping track of every excitation possible is most often impractical.

The strange and often controversial features of Quantum physics stem from the probabilistic interpretation of Schrödinger's equation. Any attempt at describing point particle observations using wave mechanics necessarily involves the use of additional constraints to avoid unphysical predictions. Traditionally, the stipulation that only the action of self-adjoint, or Hermitian, operators $\widehat{\mathcal{H}} = \widehat{\mathcal{H}}^{\dagger}$ can be probed experimentally is applied axiomatically[*10*]. Hermiticity guarantees the existence of both real numbered eigenvalues,

which is a requirement as imaginary energy, momentum or position for example would be nonsensical, and a unitary time evolution operator

$$|\Psi(t)\rangle = \widehat{U}|\Psi(0)\rangle \qquad [2.10]$$

which ensures that probabilities are conserved. Of course for a problem to be Hermitian the potential energy must be a real-valued function of position.

However, in 1998 Bender *et al.* decided to explore one dimensional Hamiltonians $\widehat{\mathcal{H}}(x)$ which extend into the complex plane[*25*]. Remarkably, they found a whole new class of non-Hermitian problems which still have real eigen spectra. Instead the reality of the eigenvalues was put down to *PT* symmetry, i.e. $\left[\widehat{\mathcal{H}}, PT\right] = 0$, where *P* is the parity or mirror operator which changes $p \to -p$ and $x \to -x$, while *T* is the time reversal operator which converts $p \to -p$ and $i \to -i$. The correspondence between complex conjugation and time reversal comes from the fact that time dependence only enters the wave function

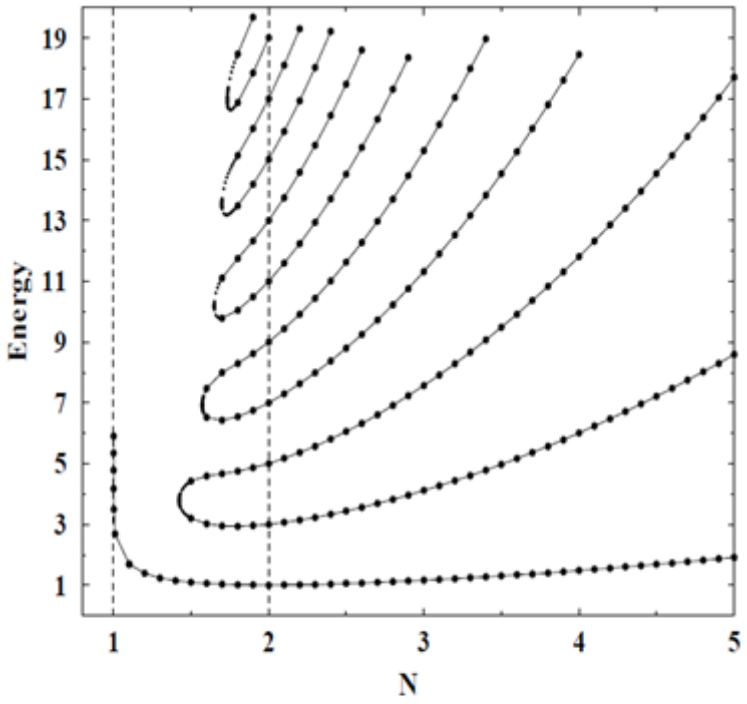

Figure 2.5: Energy levels of the Hamiltonian $\widehat{\mathcal{H}} = \boldsymbol{p^2 - (ix)^N}$ as a function of the parameter *N*. There are three regions: When $\boldsymbol{N \geq 2}$ the spectrum is real and positive. The lower bound of this region, $\boldsymbol{N = 2}$, corresponds to the harmonic oscillator, whose energy levels are $\boldsymbol{E_n = 2n + 1}$. When $\boldsymbol{1 < N < 2}$ there are a finite number of real positive eigenvalues and an infinite number of complex conjugate pairs of eigenvalues. As *N* decreases from 2 to 1, the number of real eigenvalues decreases; when $\boldsymbol{N \leq 1.42207}$, the only real eigenvalue is the ground-state energy. As *N* approaches 1, the ground-state energy diverges. For $\boldsymbol{N \leq 1}$ there are no real eigenvalues[*25*].

harmonically $\Psi_n(\boldsymbol{r},t) = e^{-\frac{iE_nt}{\hbar}}\psi_n(\boldsymbol{r})$ as t is assumed to be absent in $\widehat{\mathcal{H}}$. This also provides physical meaning to the imaginary part of the potential which can be seen to lead to exponential growth/decay of the wave function. *PT* symmetry therefore provides a natural route to exploring open quantum systems.

Interestingly, *PT* symmetry unlike Hermiticity doesn't guarantee real eigenvalues. In [*25*] a detailed numerical investigation of the Hamiltonian $\widehat{\mathcal{H}} = p^2 - (ix)^N$ was carried out as a function of the real-valued parameter *N*. The results of their analysis are summarised in Figure 2.5. Although this equation is *PT* invariant for all *N*, when $N \leq 2$ complex conjugate eigenvalue pairs emerge. In this region *PT* symmetry is said to be spontaneously broken as not all of the energy eigenstates commute with the *PT* operator. Exactly at the transition point $N = 2$, and any other *N* for which two real energy levels merge together, the associated eigenstates also become degenerate. Such coordinates are known as exceptional points (EPs), representing the extreme non-Hermitian limit[*25*].

In a later study the same authors pointed out that when *PT* symmetry is unbroken a norm preserving inner product can be defined in terms of a linear operator $C(x,y) = \sum_n \psi_n(x)\psi_n(y)$, where ψ_n are the energy eigenstates, which commutes with both *PT* and $\widehat{\mathcal{H}}$. The reason for labelling this operator *C* is that it has a very similar form to the charge conjugation operator which transforms, for example, a particle into an antiparticle. As a result, Bender et. al. proposed *CPT* symmetry as a complex generalisation of traditional quantum mechanics[*26*]. However, the physical significance of this finding is still hotly debated and, as we are only interested in the insights provided for complex wave dynamics, we will not discuss the issue further.

2.2: Classical Electromagnetism and Natural Media

In the second part of chapter two, we will introduce the physical principles, and corresponding mathematical descriptions, necessary for understanding the propagation of electromagnetic radiation through naturally occurring materials. As well as providing an initial discussion of the light-matter interaction, this section will also act as a guiding light for designing artificial systems with new and exciting properties.

2.2.1: Electromagnetic Wave Propagation

The laws of electromagnetism can be neatly summarised by Maxwell's equations

$$\boldsymbol{\nabla} \cdot \boldsymbol{E}(\boldsymbol{r}, t) = \frac{\rho(\boldsymbol{r}, t)}{\varepsilon_0} \quad [2.11]$$

$$\boldsymbol{\nabla} \cdot \boldsymbol{B}(\boldsymbol{r}, t) = 0 \quad [2.12]$$

$$\boldsymbol{\nabla} \times \boldsymbol{E}(\boldsymbol{r}, t) = -\frac{\partial \boldsymbol{B}(\boldsymbol{r}, t)}{\partial t} \quad [2.13]$$

$$\boldsymbol{\nabla} \times \boldsymbol{B}(\boldsymbol{r}, t) = \mu_0 \left(\boldsymbol{J}(\boldsymbol{r}, t) + \varepsilon_0 \frac{\partial \boldsymbol{E}(\boldsymbol{r}, t)}{\partial t} \right), \quad [2.14]$$

which describe the generation of electric $\boldsymbol{E}$ and magnetic $\boldsymbol{B}$ fields by the presence of source electric charge ρ and current $\boldsymbol{J}$ densities, as well as other time varying fields[*27*]. The fundamental constants ε_0 and μ_0 are known as the permittivity and permeability of free-space, respectively. Importantly, without sources $\rho = \boldsymbol{J} = 0$ Eq.2.11-14 can be written simply as

$$\nabla^2 \boldsymbol{E}/\boldsymbol{B}(\boldsymbol{r}, t) + \varepsilon_0 \mu_0 \frac{\partial^2 \boldsymbol{E}/\boldsymbol{B}(\boldsymbol{r}, t)}{\partial t^2} = 0, \quad [2.15]$$

permitting solutions of the form $\boldsymbol{E} = \boldsymbol{E_0} e^{i(\boldsymbol{k}.\boldsymbol{r}-\omega t)}$, $\boldsymbol{B} = -\frac{i}{\omega}\boldsymbol{k} \times \boldsymbol{E}$ where $\omega = |\boldsymbol{k}|/\sqrt{\varepsilon_0 \mu_0}$. $\boldsymbol{k}$ is known as the wave-vector and is related to the spatial periodicity or wavelength via $\lambda = 2\pi/|\boldsymbol{k}|$, and ω, known as the angular frequency, is related to the temporal periodicity via $T = 2\pi/\omega$. We can also label the quantity $c = \lambda/T = 1/\sqrt{\varepsilon_0 \mu_0}$ which represents the speed of speed of light in a vacuum. Throughout the rest of this thesis we will deal almost exclusively with the propagation of these electromagnetic wave fields, leaving their excitation and detection as an experimental detail. Consequently, non-zero ρ and $\boldsymbol{J}$ can only arise as a result of Lorentz forces acting on charges bound within previously neutral and static objects. The detailed spatial distribution of the induced $\rho(\boldsymbol{r}, t)$ and $\boldsymbol{J}(\boldsymbol{r}, t)$ can be incredibly complicated. However, the scale of variations caused by atomic and molecular effects is so small that the averaged response is often approximated by the polarisation $\boldsymbol{P}$ and magnetisation $\boldsymbol{M}$ vector fields, defined via the continuity equation $\boldsymbol{\nabla} \cdot \boldsymbol{J} - \rho = 0$ as[*27*]

$$\rho(\boldsymbol{r}, t) = -\boldsymbol{\nabla} \cdot \boldsymbol{P}(\boldsymbol{r}, t) \qquad [2.16]$$

$$\boldsymbol{J}(\boldsymbol{r}, t) = \boldsymbol{\nabla} \times \boldsymbol{M}(\boldsymbol{r}, t) + \frac{\partial \boldsymbol{P}(\boldsymbol{r}, t)}{\partial t}. \qquad [2.17]$$

In the limit $\boldsymbol{k} \to 0$, $\boldsymbol{M}$ and $\boldsymbol{P}$ physically represent the density of magnetic and electric dipole moments, respectively. Crucially, the absence of magnetic charges means that magnetic dipoles can only be generated by circulating currents, as expressed by the curl operation in Eq.2.17 and illustrated in Figure 2.6b. Having put the material response on the same footing as the electric and magnetic fields, Maxwell's equations can be written in their macroscopic form

$$\boldsymbol{\nabla} \cdot \boldsymbol{D}(\boldsymbol{r}, t) = 0 \qquad [2.18]$$

$$\boldsymbol{\nabla} \cdot \boldsymbol{B}(\boldsymbol{r}, t) = 0 \qquad [2.19]$$

$$\nabla \times \boldsymbol{E}(\boldsymbol{r},t) = -\frac{\partial \boldsymbol{B}(\boldsymbol{r},t)}{\partial t} \quad [2.20]$$

$$\nabla \times \boldsymbol{H}(\boldsymbol{r},t) = \frac{\partial \boldsymbol{D}(\boldsymbol{r},t)}{\partial t}, \quad [2.21]$$

where $\boldsymbol{D} = \varepsilon_0 \boldsymbol{E} + \boldsymbol{P}$ and $\boldsymbol{H} = \boldsymbol{B}/\mu_0 - \boldsymbol{M}$. As previously mentioned, we consider here only induced ρ and $\boldsymbol{J}$ and, therefore, $\boldsymbol{P}$ and $\boldsymbol{M}$ must be expressible in terms of the incident fields, $\boldsymbol{P} = \varepsilon_0 \boldsymbol{\chi_e} \boldsymbol{E} + \boldsymbol{\chi_{em}} \boldsymbol{H}$ and $\boldsymbol{M} = \boldsymbol{\chi_m} \boldsymbol{H} + \boldsymbol{\chi_{me}} \boldsymbol{E}$, where $\chi_{e,m,em,me}$ are known as the electric, magnetic and magneto-electric susceptibilities. A further parameterisation that can be made,

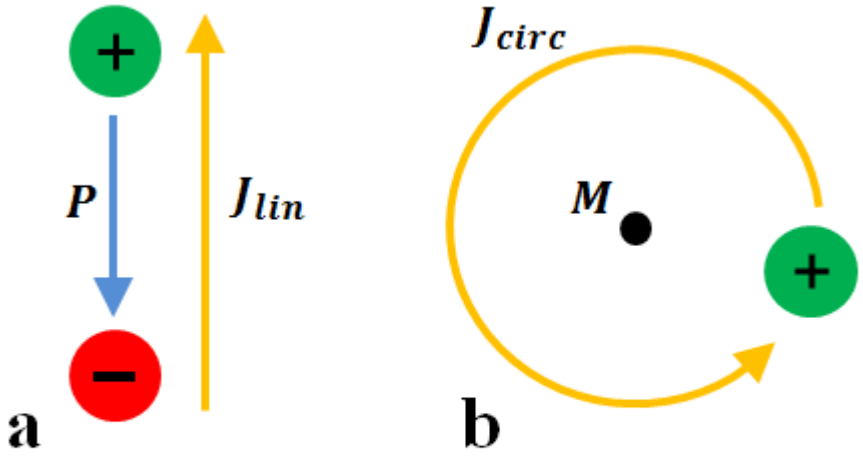

Figure 2.6: Schematic illustration of the interaction between electric and magnetic fields, and charge bound within a medium. (a) Linearly displaced charge creates dipole moment $\boldsymbol{P}$ and linear polarisation current. (b) Circulating current creates magnetic dipole moment $\boldsymbol{M}$.

which simplifies the constitutive equations, is to define the relative permittivity $\boldsymbol{\varepsilon_r} = \boldsymbol{I} + \boldsymbol{\chi_e}$ and relative permeability $\boldsymbol{\mu_r} = \boldsymbol{I} + \boldsymbol{\chi_e}$. In general, $\chi_{e,m,em,me}$ are 3x3 tensors. However, anisotropy and magneto-electric coupling are rare and usually very weak in natural materials. Ignoring these effects, classical electromagnetic problems can be reduced to solving the equation

$$\nabla^2 \boldsymbol{E}(\boldsymbol{r},t) + \varepsilon_0 \mu_0 \varepsilon_r(r) \mu_r(r) \frac{\partial^2 \boldsymbol{E}(\boldsymbol{r},t)}{\partial t^2} = 0 \quad [2.22]$$

where ε_r and μ_r are scalar quantities. As for a vacuum, represented by Eq.2.15, a homogeneous space filled with some polarisable medium accepts plane wave solutions, with the modified dispersion relation $\omega = c|\boldsymbol{k}|/\sqrt{\varepsilon_r \mu_r}$. However, unlike ε_0 and μ_0, ε_r and μ_r have in general a complex frequency dependence, originating from the internal charge dynamics. Detailed discussion of this issue will be left until later on in this chapter when physical models are introduced for specific dynamical processes. We can see that the wave speed $v = c/n$ is altered by a factor of $n = \sqrt{\varepsilon_r \mu_r}$, known as the refractive index. At this point we should note that, while devised initially to describe the response of atoms and molecules within chemical elements and compounds, metamaterials research actually grew from the simple realisation that exactly the same rules apply for artificial "atoms" if constructed on a sufficiently small scale. Such an upper limit on the structure size stems from the definition of the polarisabilities. Although $\boldsymbol{P}$ and $\boldsymbol{M}$ are always well defined, if material variations reach a significant fraction of the wavelength of the considered radiation, $\boldsymbol{P}$ and $\boldsymbol{M}$ can no longer simply be expressed in terms of $\boldsymbol{E}$ and $\boldsymbol{H}$. Instead, gradients of the fields become important and ε_r and μ_r must depend on $\boldsymbol{k}$ as well as ω, meaning that the domain cannot be considered a true effective medium. The systems investigated in chapters three and four of this thesis happen not to be particularly sensitive to such non-local effects; therefore, care has not been taken to produce deeply subwavelength designs. Nevertheless, spatial dispersion should and has been accounted for in order to provide an accurate description of the physics involved.

Having explained that it is possible to encapsulate the averaged response of an ensemble of induced charges and currents by assigning effective parameters, one final question remains. What happens to electric and magnetic fields at discontinuities which must appear at the boundary between two different materials? The answer can be found by considering the integral forms of Eqs.2.18-2.21 directly at the interface. It is straightforward to show that, due to the lack of free surface charge, the normal components of $\boldsymbol{D}$ and $\boldsymbol{B}$ must

be continuous. Similarly, the absence of free surface currents means that the tangential components of $\boldsymbol{E}$ and $\boldsymbol{H}$ must also be continuous.

In section 2.3 of this chapter we will focus on how artificial structures can be exploited for manipulating electromagnetic radiation, within the mathematical framework developed in the current section. Particular attention will be paid to wave propagation through media with highly anisotropic ε_r and μ_r, as well as strong magneto-electric coupling.

2.2.2: Light and Metals

In the previous section, we discussed the existence of wave solutions to Eq.2.22, with wavenumbers $|\boldsymbol{k}| = \omega\sqrt{\varepsilon_r\mu_r}/c$. However, only real-valued wavenumbers represent propagating solutions. For $\varepsilon_r\mu_r < 0$, $|\boldsymbol{k}|$ becomes imaginary, corresponding to evanescent fields which decay in space. The most common materials to exhibit this kind of behaviour are metals, which have a negligible magnetic response $\mu_r = 1$ but a strong electric response $\varepsilon_r < 0$. Typically, the interaction between metals and oscillating electric fields $\boldsymbol{E} = \boldsymbol{E_0}e^{-i\omega t}$ is described via the Drude model, which treats the conduction electrons as free particles, allowing the AC conductivity to be expressed by[*28*]

$$\sigma(\omega) = \frac{\sigma_0}{1 - i\frac{\omega}{\gamma}}, \qquad [2.23]$$

where σ_0 is the DC conductivity and γ describes the rate at which electrons dissipate energy through collisions with each other and lattice defects. As the induced current is simply $\boldsymbol{j} = \sigma\boldsymbol{E}$, the permittivity can then be written as

$$\varepsilon_m = \varepsilon_\infty + \frac{i\sigma_0}{\varepsilon_0\omega\left(1 - i\frac{\omega}{\gamma}\right)}, \qquad [2.24]$$

where ε_∞ represents the dielectric response of bound electrons. From Eq.2.24 it can be shown that, for $\omega < \omega_p = \sqrt{\frac{\gamma\sigma_0}{\varepsilon_0}}$, where ω_p is known as the plasma frequency, the real part of ε_m takes on negative values and propagating waves are suppressed. In fact, the Drude model predicts a complex permittivity with both real and imaginary parts contributing to the decay coefficient of the electric field. Importantly, however, only the imaginary part of ε_r shows up in the expression for the change in the time averaged power and thus represents attenuation of the incident radiation. Perhaps the most interesting behaviour revealed by Eq.2.24 occurs for $\gamma < \omega < \omega_p$. Here, $\left|\frac{Re(\varepsilon_m)}{Im(\varepsilon_m)}\right| \gg 0$ allowing the field to penetrate into the metal with minimal loss of energy[*28*]. What's more, an interface between such a metal and a dielectric medium $\varepsilon_d > 0$ can be shown to support propagating solutions known as surface plasmon polaritons (SPP), which can be used for a range of exciting applications. With plasma frequencies tending to lie in the ultraviolet, surface plasmons traditionally exist only at optical frequencies.

Throughout this thesis we will mainly be concerned with electromagnetic waves oscillating at frequencies of one Terahertz and below. Estimates often put the collision frequencies of commonly used metals, including gold, silver, lead and aluminium, in the far-infrared spectral region $\gamma \sim 10THz$. It has also been shown that in thin films an increased contribution from surface defects pushes γ to higher frequencies and, consequently, for the regime and structures under consideration $\frac{\omega}{\gamma} \ll 1$, meaning that the permittivity can be written approximately as[*29*, *30*]

$$\varepsilon_m \approx \varepsilon_\infty - \frac{\sigma_0}{\varepsilon_0\gamma} + \frac{i\sigma_0}{\varepsilon_0\omega}. \qquad [2.25]$$

The final, imaginary term in this expression also dominates the other two and so, metals can often be described purely in terms of the DC conductivity[*29*]. At even lower frequencies, i.e.

microwaves, the ratio between the penetration depth and the wavelength becomes so small that metallic regions can be replaced, to a very good approximation, by a hard wall boundary condition $\boldsymbol{E} = 0$ on the perimeter. Not only does this significantly improve the computational efficiency of simulations, but it also means that metallic absorption of microwaves is negligible, making them ideal candidates for guiding such radiation over long distances.

2.2.3: Birefringence in Anisotropic Media

While most materials can be described by simple scalar parameters, in certain crystals, such as calcite and rutile, the strength of the induced dipole moments depends on the orientation of the applied electric field with respect to the crystal axes. In this case, the permittivity must be represented by a 3×3 tensor, which is diagonal in the principal coordinates. Anisotropy has two key consequences. Firstly, an electromagnetic wave travelling in a given direction within such a medium can experience two possible refractive indices depending on the direction in which the field is polarised. This is commonly referred to as birefringence. Secondly, the inherent relationship that exists between the polarisation and the wavevector, coming from Eqs.2.18-2.19, means that the refractive index can also vary for different propagation directions. We can see this by considering the more general form of Eq.2.22

$$-\nabla \times \nabla \times \boldsymbol{E}(\boldsymbol{r},t) = \varepsilon_0 \mu_0 \boldsymbol{\varepsilon_r} \frac{\partial^2 \boldsymbol{E}(\boldsymbol{r},t)}{\partial t^2}, \qquad [2.26]$$

for a homogeneous space with $\boldsymbol{\varepsilon_r} = diag(\varepsilon_x, \varepsilon_y, \varepsilon_z)$ and $\mu_r = 1$, where $\varepsilon_x \neq \varepsilon_y \neq \varepsilon_z$. Substituting $\boldsymbol{E} = \boldsymbol{E_0} e^{i(\boldsymbol{k}.\boldsymbol{r}-\omega t)}$, the dispersion relations for plane waves can then be found by solving

$$\begin{vmatrix} -k_y^2 - k_z^2 + \varepsilon_x\left(\frac{\omega}{c}\right)^2 & k_x k_y & k_x k_z \\ k_x k_y & -k_y^2 - k_z^2 + \varepsilon_y\left(\frac{\omega}{c}\right)^2 & k_y k_z \\ k_x k_z & k_y k_z & -k_y^2 - k_z^2 + \varepsilon_z\left(\frac{\omega}{c}\right)^2 \end{vmatrix} = 0. \quad [2.27]$$

In the simplified, and more common, scenario of a uniaxial permittivity $\varepsilon_x = \varepsilon_y$, Eq.2.27 can be factorised into the expressions

$$k_x^2 + k_y^2 + k_z^2 = \varepsilon_x\left(\frac{\omega}{c}\right)^2, \quad [2.28]$$

corresponding to a so called Transverse Electric (TE) wave, as its electric field is polarised in the xy plane and,

$$\frac{k_x^2 + k_y^2}{\varepsilon_z} + \frac{k_z^2}{\varepsilon_x} = \left(\frac{\omega}{c}\right)^2, \quad [2.29]$$

corresponding to a Transverse Magnetic (TM) wave, as its Magnetic field is polarised in the xy plane. Although Eq.2.28 describes an isotropic response, which is reasonable since the $\boldsymbol{E}$ field only interacts with ε_x and not ε_z, Eq.2.29 reveals that the TM mode has an ellipsoidal dependence on the wavevector. Consequently, these materials are sometimes referred to as elliptic media. From Figure 2.7 the difference in the effective indices for the two solutions can be seen to vanish for waves propagating along the optical axis $\hat{\boldsymbol{z}}$ and reach a maximum $|\Delta n| = \left|\sqrt{\varepsilon_x} - \sqrt{\varepsilon_z}\right|$ for waves propagating perpendicular to $\hat{\boldsymbol{z}}$. Between these two directions the TM wave also has the strange property that its group velocity $\boldsymbol{v}_g = \boldsymbol{\nabla}_k \omega(\boldsymbol{k})$, which can also be represented geometrically as the normal to the equi-frequency surface (EFS), and phase velocity $\boldsymbol{v}_p = \frac{\omega}{|\boldsymbol{k}|}\widehat{\boldsymbol{k}}$ are misaligned. Electromagnetic energy within such a material, therefore, flows in a different direction to that of the wave fronts.

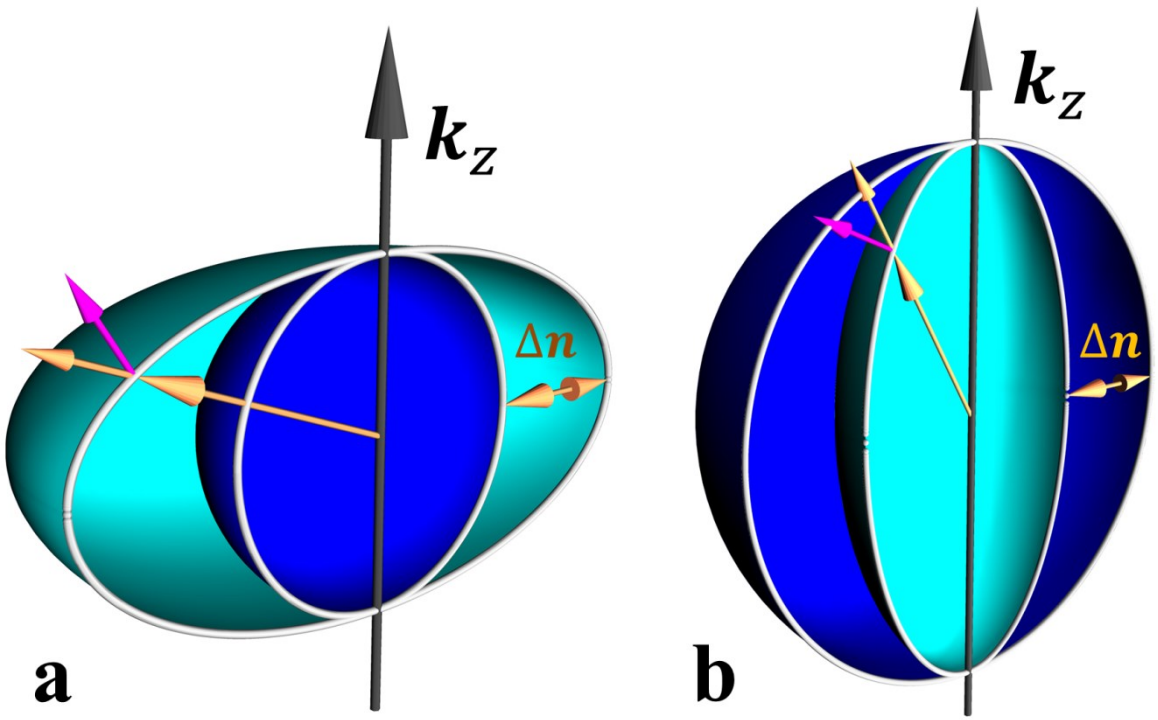

Figure 2.7: Equi-frequency surfaces for uniaxially birefringent media with z orientated optical axes. (a) Positive birefringence $\boldsymbol{n_z = 3}$ and $\boldsymbol{n_{x/y} = 1.5}$. (b) Negative birefringence $\boldsymbol{n_z = 1.5}$ and $\boldsymbol{n_{x/y} = 3}$. In both figures orange arrows represent wave-vectors and purple arrows represent group velocity directions. The blue and turquoise EFSs correspond to TE and TM polarisations, respectively.

Not only is birefringence an interesting phenomenon, but it can also be useful for manipulating polarisation states of light. Changes in photonic polarisation are best described by using Jones calculus in which the transverse electric or magnetic field of a wave is represented by a complex two component vector. Alterations caused by the wave's passage through a polarising medium can then be accounted for by the action of a transfer matrix, commonly referred to as a Jones matrix[*31*]

$$\begin{pmatrix} \tilde{E}_x \\ \tilde{E}_y \end{pmatrix}_{transmitted} = \begin{pmatrix} \tilde{t}_{xx} & \tilde{t}_{xy} \\ \tilde{t}_{xy} & \tilde{t}_{yy} \end{pmatrix} \begin{pmatrix} \tilde{E}_x \\ \tilde{E}_y \end{pmatrix}_{incident}. \qquad [2.30]$$

This also allows us to determine the polarisation state transmitted through a stack of materials with different properties simply by cascading Jones matrices $\widetilde{\boldsymbol{E}}_t = \hat{J}_3\hat{J}_2\hat{J}_1 \ldots \widetilde{\boldsymbol{E}}_i$. The response of a birefringent slab whose optical axis lies in $\hat{\boldsymbol{x}}$ for example can be written as

$$\hat{J}_{bi} = \begin{pmatrix} e^{i\Delta n\pi\frac{d}{\lambda}} & 0 \\ 0 & e^{-i\Delta n\pi\frac{d}{\lambda}} \end{pmatrix}, \qquad [2.31]$$

where d is the thickness of the slab and λ is the optical wavelength. From Eq.2.31 it can be seen that circular polarisation can be produced by passing $\hat{\boldsymbol{x}}$ or $\hat{\boldsymbol{y}}$ polarised light through a slab of thickness $d = \frac{\lambda}{4|\Delta n|}$. Such a device is known as a quarter-waveplate and is one of the most widely used components in modern optics. The difference in TE and TM refraction angles can also be used for making polarising beam splitters.

2.2.4: Surface Waves

We have already seen that under certain circumstances the dispersion relation $\omega(\boldsymbol{k})$ can only be satisfied by wavevectors with at least one imaginary component, corresponding to fields which exponentially decay along some spatial coordinate. Such solutions to Maxwell's equations play an important role in describing the behaviour of waves at boundaries between media with different electromagnetic properties. For example, evanescent fields are responsible for the strong reflections that occur at a metal-dielectric interface and the total reflection that occurs, beyond a critical incident angle, for light passing from one dielectric material to another. In this section, we will discuss another possibility in which travelling waves are prohibited on both sides of an interface. In this case, solutions that propagate along the interface, but decay away from it, can still exist. In recent years it has been shown that these so called surface waves can be incredibly useful for guiding and controlling electromagnetic energy.

For any one dimensional boundary between two distinct, homogeneous, materials, i.e. properties varying as a step function of a single coordinate, chosen here to be z, the existence of surface waves can be investigated by following a universal prescription. First of all, the

general spatially dependant solution $E/H_j(x,y,z) = A_j e^{-\beta_j|z|} e^{i(k_x x + k_y y)}$, where β_j, k_x and k_y are real and positive in a lossless system, is fixed by the presence of translational symmetry in x and y and the requirement that the excitation be bound to the interface. Relationships between the fields can then be found by using Eqs.2.20-2.21 to solve for the polarisation eigenstates in each medium. Finally, after applying the boundary conditions given at the end of (2.2.1), the existence and dispersion of surface waves can be determined. We can apply this procedure to the simple case of isotropic, non-magnetic $\mu_r = 1$ media $\varepsilon_1 \neq \varepsilon_2$, choosing x as the propagation direction $k_y = 0$ without loss of generality. As for plane waves within such materials, surface modes can be separated out into independent TE $\left(E_x = E_z = H_y = 0\right)$ and TM $\left(H_x = H_z = E_y = 0\right)$ polarised components. The decay coefficients on each side of the interface can then be shown to follow

$$\beta_2 = -\beta_1, \qquad [2.32]$$

for TE and

$$\frac{\beta_2}{\beta_1} = -\frac{\varepsilon_2}{\varepsilon_1}, \qquad [2.33]$$

for TM. Clearly Eq.2.32 cannot be satisfied with $\beta_{1,2} > 0$ and, therefore, TE polarised surface waves cannot be localised. Eq.2.33 on the other hand, can be satisfied with $\beta_{1,2} > 0$ as long as $Re(\varepsilon_2)/Re(\varepsilon_1) < 0$. This means that one of the two materials must be metallic, while the other is a dielectric. By ensuring that the parameters β_1, β_2 and k_x are consistent with Eqs.2.22 and 2.33, the dispersion relation for the TM wave, known as a surface plasmon polariton (SPP), can be then found[*28*]

$$k_x = \frac{\omega}{c}\sqrt{\left(\frac{\varepsilon_1\varepsilon_2}{\varepsilon_1 + \varepsilon_2}\right)}. \qquad [2.34]$$

Figure 2.8 shows the dispersion relation for SPPs at the interface between a vacuum $\varepsilon_1 = 1$ and an ideal Drude metal $\varepsilon_2 = 1 - \omega_p^2/\omega^2$. As well as being localised in the

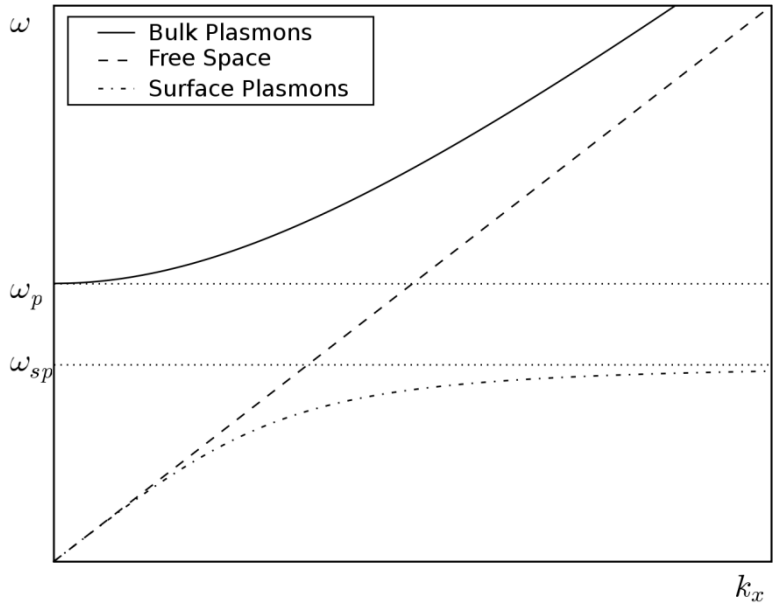

Figure 2.8: Dispersion relation of a surface plasmon polariton at the interface between a vacuum and a lossless metal[*32*]**.**

direction normal to the boundary, it can be seen that when $\varepsilon_1 + \varepsilon_2$ becomes small the plasmonic wavenumber grows much bigger than the free-space equivalent. Such large wavenumbers, therefore, allow electromagnetic fields to be confined within regions much smaller than the free-space wavelength, which is usually forbidden by the well-known diffraction limit. Although in Eq.2.34 k_x asymptotically approaches ∞ as ε_2 tends to ε_1, in reality absorption in the metal, represented by an imaginary part in ε_2, will provide an upper bound for k_x. High losses also prevent long propagation distances. Nevertheless, aided by the development of nanofabrication techniques such as electron beam lithography, these excitations have been used to demonstrate unprecedented levels of control in optical experiments. Consequently, surface plasmons are currently at the heart of modern research into nano-photonics and are becoming more and more popular for creating nanoscale devices.

Much more recently, a new type of surface wave has been discovered which does not rely on a metallic response. Predicted in 1988, these so called Dyakonov waves exist at boundaries between materials which depend differently on the electric and/or magnetic field directions[*33*]. The initial study in [*33*] considered the particular case of an isotropic dielectric medium ε_1 and a uniaxial dielectric medium with its optical axis, chosen here to be z, aligned parallel to the interface $\varepsilon_z = \varepsilon_\parallel, \varepsilon_x = \varepsilon_y = \varepsilon_\perp$. In (2.2.3) we have already explored the polarisation eigenstates of just such an anisotropic material, showing that there exists a TE solution with $E_z = 0$ and a TM solution with $H_z = 0$, described by Eq.2.28 and Eq.2.29, respectively. As there is now three different dispersion relations, in general we must have three different decay coefficients β_{TE}, β_{TM} and β_{iso} normal to the interface, chosen here to lie at $x = 0$ with $\varepsilon = \varepsilon_1$ for $x > 0$ and $\varepsilon = diag(\varepsilon_\perp \quad \varepsilon_\perp \quad \varepsilon_\parallel)$ for $x < 0$. After applying Eqs.2.18-2.21 in the two regions, the electric and magnetic field components of each mode can be written as

$$\begin{bmatrix} E_x \\ E_y \\ E_z \end{bmatrix} = \begin{bmatrix} 0 \\ 1 \\ 0 \end{bmatrix}_{TE_+}, \begin{bmatrix} q \\ 0 \\ -i\beta_{iso} \end{bmatrix}_{TM_+}, \begin{bmatrix} q\sin\varphi \\ i\beta_{TE}\cos\varphi \\ i\beta_{TE}\sin\varphi \end{bmatrix}_{TE_-}, \begin{bmatrix} i\beta_{TM} q\cos\varphi \\ -\varepsilon_\perp \sin\varphi \\ (\varepsilon_\perp - q^2)\cos\varphi \end{bmatrix}_{TM_-},$$

$$\begin{bmatrix} H_x \\ H_y \\ H_z \end{bmatrix} = \begin{bmatrix} -q \\ 0 \\ i\beta_{iso} \end{bmatrix}_{TE_+}, \begin{bmatrix} 0 \\ \varepsilon_1 \\ 0 \end{bmatrix}_{TM_+}, \begin{bmatrix} -i\beta_{TE} q\cos\varphi \\ \varepsilon_\perp \sin\varphi \\ \beta_{TE}^2 \cos\varphi \end{bmatrix}_{TE_-}, \begin{bmatrix} q\varepsilon_\perp \sin\varphi \\ i\beta_{TM}\varepsilon_\perp \cos\varphi \\ i\beta_{TM}\varepsilon_\perp \sin\varphi \end{bmatrix}_{TM_-}, \quad [2.35]$$

where $q^2 = k_y^2 + k_z^2$ and $\tan\varphi = k_z/k_y$. Unlike the above case for SPPs, TE_- and TM_- are not necessarily orthogonal and, therefore, surface waves are in general made up of all four eigenstates. By equating the tangential fields, E_y, E_z, H_y and H_z, across the boundary it can be shown that for a surface wave to exist, the bulk dispersion relations as well as the condition

$$(\beta_{iso} + \beta_{TM})(\beta_{iso} + \beta_{TE})(\varepsilon\beta_{TE} + \varepsilon_\perp\beta_{TM}) = (\varepsilon_\parallel - \varepsilon)(\varepsilon - \varepsilon_\perp)\beta_{TE} \quad [2.36]$$

must be satisfied. Once again, we need $\beta_{iso}, \beta_{TE,} \beta_{TM} > 0$ for the excitation to be localised at the interface. It follows that this requirement is only met by the configuration $\varepsilon_\parallel > \varepsilon > \varepsilon_\perp$.

Even with appropriate material parameters the wave can only propagate within a certain range of angles φ, the limits of which depend on the permittivities as

$$\sin^2 \varphi_{min} = \frac{\xi}{2}[1 - \eta\xi + \sqrt{((1+\eta\xi)^2 + 4\eta)}],$$
$$\sin^2 \varphi_{max} = \frac{(1+\eta)^3\xi}{(1+\eta)^2(1+\eta\xi) - \eta^2(1-\xi)^2}, \quad [2.37]$$

where $\eta = \frac{\varepsilon_\parallel}{\varepsilon_\perp} - 1$ and $\xi = \frac{(\varepsilon - \varepsilon_\perp)}{(\varepsilon_\parallel - \varepsilon_\perp)}$.

Dyakonov waves were only observed experimentally in 2009[*34*], 20 years after they were first predicted to occur. This delay can be attributed to the lack of materials available with a suitably anisotropic response. While many birefringent crystals exist, they typically have very weak directionality $\eta \ll 1$. Not only does this necessitate a cover material to be chosen with a very specific ε, but it also leads to a very small angular distribution of possible surface wavevectors, requiring incredibly precise measurements. As we will discuss in section (2.3), metamaterials research provides an ideal platform for not only achieving extremely strong anisotropy but also combining Dyakonov's original idea with more exotic interactions, such as magneto-electric coupling.

2.3: Artificial Electromagnetic Media

In the final part of chapter 2 we will outline some key concepts which underpin recent developments in the field of artificial electromagnetism. In particular, we will focus on metamaterials, man-made structures composed of elements arranged on a subwavelength scale whose properties can be derived from geometry rather than the constitutive materials they are made form. As well as enabling the realisation of completely new phenomena such as negative refractive index and super-lenses, metamaterials also provide the ability to enhance and control properties found in natural media. Throughout this section, we will build

on the foundations laid down in (2.2), showing how an understanding of the microscopic formation of electric and magnetic dipoles can provide a recipe for geometrically tailoring the light matter interaction. We will also place a particular emphasis on polarisation dependant propagation in anisotropic and bi-anisotropic media. This information will provide the necessary tools needed for investigating photonic *PT* symmetry and topology in the following chapters.

2.3.1: Wire-Metamaterials as Designer Metals

As discussed in (2.2.2/4), electrically conducting materials are very useful for confining and controlling optical frequency electromagnetic fields on the subwavelength scale. This functionality relies crucially on the dominance of the negative real part of the permittivity, which only occurs in the range $\gamma < \omega < \omega_p$. At lower frequencies, absorption takes over and metals start behaving like lossy mirrors. The plasma frequency associated with a given metal depends on the number density n_e and effective mass m_e of free electrons

$$\omega_p^2 = \frac{n_e e^2}{\varepsilon_0 m_e}, \qquad [2.38]$$

where e is the electric charge. While it lies traditionally in the visible or ultraviolet part of the electromagnetic spectrum, in 1996 Pendry *et. al.* realised that chemistry wasn't the only tool available for manipulating ω_p[*2*]. Starting with a conventional metallic solid and stripping away most of the material until currents can be driven only in a mesh of very thin wires; the remaining structure can be assigned an effective plasma frequency ω_p^* given by Eq.2.38 in terms of an effective free electron density n_e^* which is smaller than n_e in proportion to the

reduction of space occupied by the metal. By localising the flow of current, inductance is also

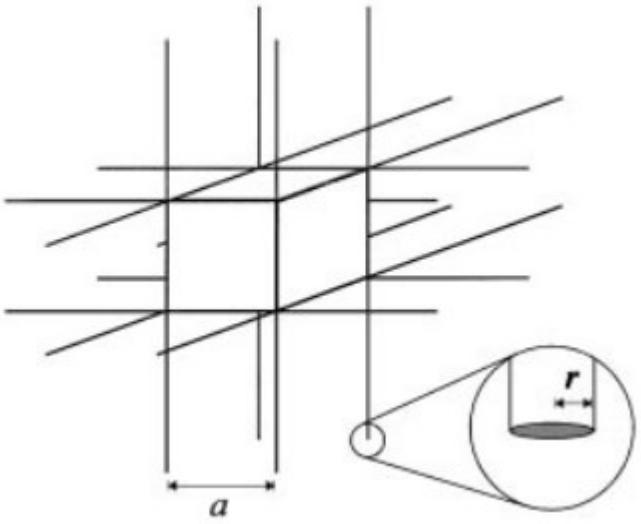

Figure 2.9: Schematic of a wire-metamaterial with a geometrically suppressed plasma frequency[*2*].

generated which acts to increase the effective mass of the electrons

$$m_e = \frac{\mu_0 n_e r^2}{2} \ln\left(\frac{d}{r}\right), \qquad [2.39]$$

where d is the lattice constant of the mesh and r is the wire radius. Taking both of these effects into account we obtain

$$\omega_p^{*2} = \frac{2\pi c^2}{d^2 \ln\left(\frac{d}{r}\right)}. \qquad [2.40]$$

From this expression we can clearly see that the plasma frequency of a domain can easily be controlled by scaling up the size of the unit cell. Importantly, however, as mentioned in (2.2) the appropriate use of such a parameter within an effective medium description of an inhomogeneous space, Eq.2.24, relies on the variation of induced sources being much smaller than the electromagnetic wavelength. Due to the logarithmic dependence of λ_p on (d/r), $\lambda_p = d\sqrt{2\pi \ln(d/r)}$, the use of wires that aren't a lot thinner than the lattice spacing will therefore cause the true response to deviate from the simple frequency dependent model discussed above. In fact, by considering waves propagating in arbitrary directions, such that

the electric field neither aligns parallel nor perpendicular to the wires, it can be shown that at low frequencies the local description breaks down even in the limit $\boldsymbol{k} \to 0$, due to the presence of longitudinal modes[*35*]. We will discuss modifications that can be made to overcome this strong spatial dispersion in the following section. Despite these limitations, a number of groups have successfully demonstrated a plasmonic response to microwaves using Pendry's approach, including the first realisation of a material with a negative refractive index[*4*, *36*].

2.3.2: Hyperbolic Metamaterials

The electromagnetic response of many metamaterial elements depends critically on the direction in which the fields are applied. Far from a coincidence, this anisotropy facilitates a strong interaction between radiation and subwavelength current distributions. Early on, researchers considered this to be detrimental to the performance of their designs, not least because of a desire to realise an isotropic 3D material with a negative refractive index. However, not only are metamaterials with an anisotropic response easier to design and fabricate, but they can also reveal properties that are as, if not more, interesting and useful than their isotropic counterparts. As discussed in (2.2.3), natural crystals with a directionally dependent response do exist but they usually only possess a very slight variation in the index for different orientations $\Delta n \ll \bar{n}$. Not only can artificial structures be used to dramatically enhance the range of possible Δn that can be achieved, but they also enable a scenario that very rarely occurs naturally, in which metallic and dielectric behaviour coexists. Some exceptions to this are found in the THz and far-infrared regimes where anisotropic phonon resonances and plasma oscillations lead to narrow bands with extreme properties[*37*]. Mathematically, these materials can be described by a 3×3 permittivity and/or permeability tensor with positive and negative components. For simplicity, in this section we restrict our

attention to non-magnetic $\mu_r = 1$ and uniaxial systems $\boldsymbol{\varepsilon_r} = diag(\varepsilon_x, \varepsilon_x, \varepsilon_z)$ as all of the salient features are captured by this simplification. We will extend our treatment to the most general case, including magneto-electric coupling, when designing a topological metamaterial in chapter 4. Two possibilities remain, type I ($\varepsilon_x < 0, \varepsilon_z > 0$) and type II ($\varepsilon_x > 0, \varepsilon_z < 0$). The corresponding wave solutions to Maxwell's equations are given by Eqs.2.28-2.29. From Eq.2.28 we can see that only a type II permittivity supports

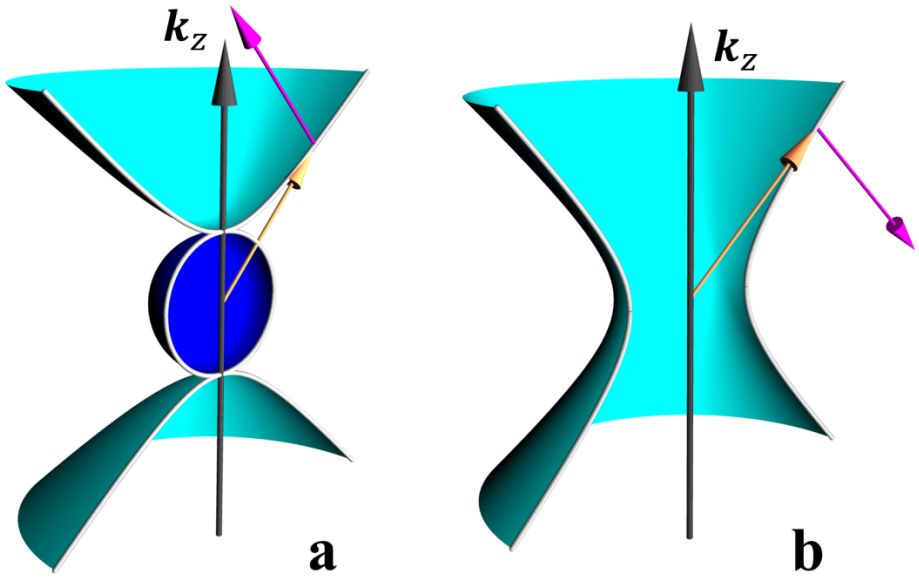

Figure 2.10: Equi-frequency surfaces for uniaxial hyperbolic media with *z* orientated optical axes.(a) type II ($\boldsymbol{\varepsilon_x > 0, \varepsilon_z < 0}$). (b) type I ($\boldsymbol{\varepsilon_x < 0, \varepsilon_z > 0}$). In both figures orange arrows represent wave-vectors and purple arrows represent group velocity directions. The blue and turquoise EFSs correspond to TE and TM polarisations, respectively.

an isotropic TE mode as $\varepsilon_x < 0$ leads to an imaginary wavevector. More interestingly, Eq.2.29 now represents the equation for a k space hyperbola. In stark contrast to elliptical media, the EFSs for TM modes in these so called hyperbolic media, shown in Figure 2.10, are unbound. Remarkably, this means that light with an arbitrarily small wavelength can propagate through such materials, making them ideal for super resolution imaging[*38*, *39*]. As well as permitting solutions with large wavenumbers, the infinite area of the hyperbolic EFSs also provides a divergence in the density of states available to local sources of radiation. It has been shown that this divergence can dramatically enhance the Purcell factor

of a quantum emitter placed in close proximity to the anisotropic metamaterial[*40*]. Similarly, the power of Cerenkov radiation emitted within hyperbolic systems can be shown to increase, rather than decrease as per convention, with a decrease in particle velocity[*41*]. This may be useful for the detection of heavy charged particles. From Figure 2.10 we can also see that the orientation of the group velocity of the TM wave can deviate massively from its phase velocity. This has allowed negative refraction to be observed without the need for a magnetic response, as required by materials with a negative refractive index[*42*, *43*].

The accuracy of Eq.2.29 relies on the elements of the permittivity tensor being strictly local parameters. In reality, any structure used to investigate these hyperbolic phenomena must have some finite periodicity or length scale. Near the corresponding Brillouin zone edge, Bragg scattering will modify the wave dynamics providing a natural cut-off. Perhaps more importantly, at least for optical applications, the presence of metallic losses will also lead to strong attenuation of the high k modes over relatively short distances even with a very small lattice constant. Nevertheless, most of the above mentioned phenomena have been successfully demonstrated at a range of different frequencies, showing that these limitations do not completely destroy the validity of the approach and interesting physics can still be observed[*44*].

The vast majority of experimental investigations into hyperbolic metamaterials have employed structures similar to Figure 2.9 but with metallic regions extending continuously only in one or two dimensions. While a 2D array of parallel wires is often used to realise a type II medium, type I media usually take the form of simple 1D metal-dielectric stacks, due to the ease of fabrication. As shown in (2.3.1), electric fields aligned with the wires or sheets will experience a geometrically dependant Drude response. Conversely, as long as the structures are very thin, so as to avoid unwanted resonant effects, perpendicular fields will be unable to induce currents in the metal and will therefore only interact with the dielectric host.

These designs work well at high frequencies, for micro and nano fabricated structures, and can be described reasonably well by a local permittivity tensor. In 2003 however, Belov *et. al.* revealed that in the microwave regime wire structures suffer from spatial dispersion even in the long wavelength limit $\boldsymbol{k} \to 0$[*35*]. Although the response to waves propagating perpendicular to the wires agrees with Pendry's diluted plasma model, for other directions the axial permittivity can be shown to take the modified form

$$\varepsilon_z(\omega, \boldsymbol{k}) = \varepsilon_0 \left(1 - \frac{\omega_p^2}{\omega^2 - (ck_z)^2}\right). \qquad [2.41]$$

Not only does this diminish the original claim that such an array can be considered as an effective medium, but after solving for the corresponding eigenmodes it can be shown that the interesting high-k states, previously predicted to occur for TM polarisations, vanish. Physically, this strong spatial dispersion originates from the large conductivity of the metals involved, allowing charge to build up on the wires. Later, Pendry *et. al.* provided a solution to this problem. By adding structures to increase the capacitive or inductive interaction

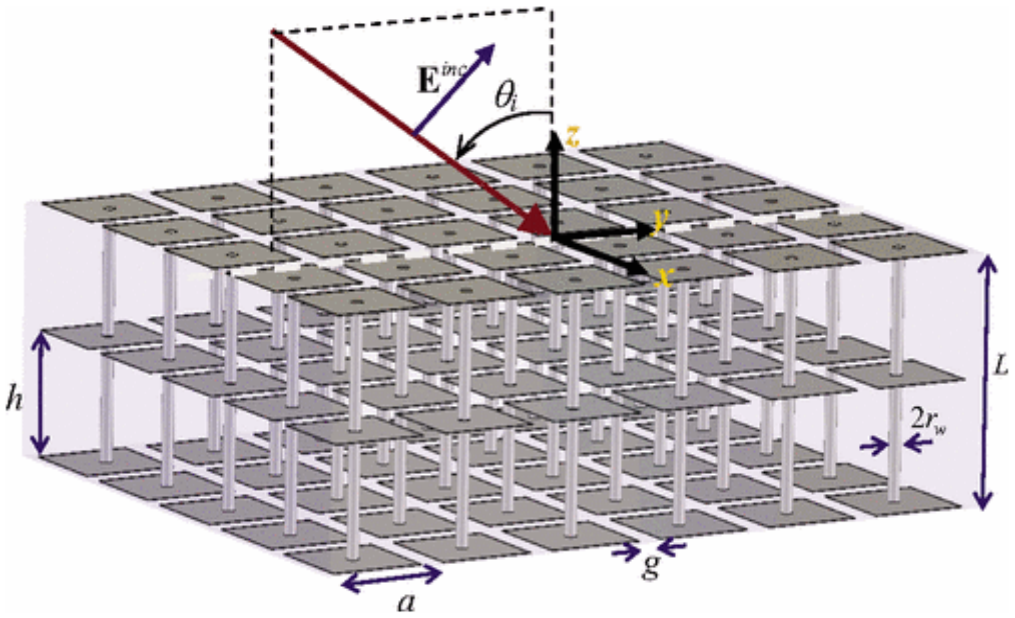

Figure 2.11: Schematic diagram of a capacitively loaded wire metamaterial. The structure is designed to exhibit negative refraction due to the possession of a local hyperbolic permittivity[*46*].

between the wires, charge can be re-distributed throughout the unit cell and a local hyperbolic response can be re-established[*45*]. One such design which employs metallic plates is illustrated in Figure 2.11[*46*].

2.3.3: Designer Atoms and Artificial Magnetism

Up until now, we have focussed on explaining ways in which the ability of a domain to conduct electricity can be tailored by structuring the constitutive metals, allowing one to control the details of a Drude type permittivity. In this section, we will consider the possibility of replicating the qualitatively different response of insulating materials in which charge is tightly bound within atoms or molecules. As for metals, the presence of an electromagnetic field can drive the charge into motion. However, in this case, the strong Coulombic restoring forces involved lead to a Lorentzian form for the polarisability[*27*]

$$\alpha(\omega) \propto \frac{1}{\omega^2 - \omega_0^2 + i\gamma\omega}, \qquad [2.42]$$

where ω_0 is the resonant frequency and γ once again represents the rate at which energy is dissipated. As mentioned in (2.2.1), the absence of magnetic charges means that secondary sources of electric and magnetic fields require distinct physical mechanisms. Electric dipoles can arise, for example, from electron clouds which are linearly displaced with respect to their atomic nuclei, whereas magnetic dipoles rely on atomic or molecular states with a sense of rotation, such as those with a non-zero orbital or spin quantum number. Not only do these processes lead to separate resonant features, but the field strengths they generate also scale differently with the size of the object in question, which in turn explains the relative weakness of magnetic effects, especially at high frequencies[*47*]. It is this fundamental asymmetry that makes the prospect of realising artificial atoms so attractive.

We have already seen that subwavelength arrays of straight conducting wires can be used to geometrically depress the effective plasma frequency. In 1999, Pendry *et.al.* theoretically explored the possibility of using metallic loops to produce an artificial magnetic response to axial fields[*3*]. Importantly, structures were chosen that contained gaps, impeding the flow of current and causing a build-up of charge. These so called split ring resonators (SRR) can be modelled as LRC circuits, were the inductance L and capacitance C depend on the size and shape of the loops and the gaps in the design, respectively, while the resistance R represents the net dissipation of energy trapped close to the ring. It is well known that such a circuit obeys the same harmonic oscillator equation as the atomic transitions discussed above, with $\omega_0 = \frac{1}{\sqrt{LC}}$. If we then arrange a large number of these structures in a periodic fashion, for radiation with a wavelength much larger than the lattice constant, each ring can be treated as a single magnetic dipole $\boldsymbol{m} = \alpha(\omega)\boldsymbol{H}$, resulting in the magnetisation $\boldsymbol{M} = F\boldsymbol{m}$, where F is

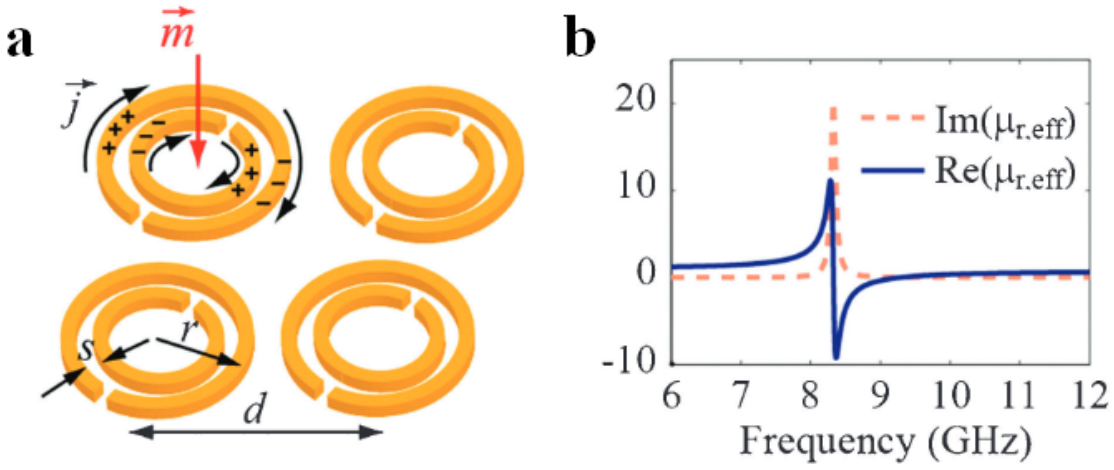

Figure 2.12: Artificial magnetism in SRR metamaterials.a) Schematic diagram of a double SRR array b) Effective permeability of SRR array shown in "a" with $\boldsymbol{d} = \boldsymbol{4mm}$, $\boldsymbol{r} = \boldsymbol{1mm}$ and $\boldsymbol{s} = \boldsymbol{0.1mm}$[*48*].

the SRR filling fraction. Following the prescription used for describing the response of wire-metamaterials, such an array can be considered as a homogeneous medium, with an effective permeability

$$\mu_r(\omega) = 1 - \frac{\omega^2 F}{\omega^2 - \omega_0^2 + i\gamma\omega}. \quad [2.43]$$

From the example shown in Figure 2.12, we can see that as well as being enhanced close to resonance, μ_r behaves very differently above and below ω_0. This difference stems from the frequency dependent phase of the induced dipoles. For $\omega > \omega_0$, The Magnetisation lags behind the incident magnetic field causing them to interfere destructively. If the magnitude of the response is strong enough the permeability can even become negative, as evidenced by Figure 2.12b, which is incredibly rare in natural materials. The dominant role played by geometry in deciding the value of parameters found in Eq.2.43 provides a clear route for designing artificial magnetic materials. However, as already mentioned, variations that aren't significantly smaller than the wavelength prohibit the accurate use of a purely frequency dependent μ_r. Because μ_r tends to one away from resonance, it is therefore critical that we find structures, with characteristic length scale d, for which $\omega_0 d/c \ll 1$. Although L depends on the area enclosed by the SRR, causing the resonant wavelength to vary linearly with the ring radius, C can in principle be increased arbitrarily by using very fine gaps relative to the ring width without increasing its radius. What's more, sophisticated designs which employ multiple rings, like the example shown in Figure 2.12, can be used to further enhance the capacitance. Guided by simple circuit theory, researchers have been able to significantly reduce $\omega_0 d/c$. Since these ideas were first presented, many groups have followed the path laid out in [*3*] to geometrically enhance magnetism at a range of different frequencies, including regimes in which the response of natural materials is very weak[*49*, *50*]. As shown in Figure 2.13, structures employed to achieve an optical response are somewhat different from their microwave counterparts. This is because plasmonic effects takeover from the simple circuit description. Such effects also give rise to enhanced material or Ohmic losses in

the metal producing a large imaginary part in the effective parameters close to a resonance.

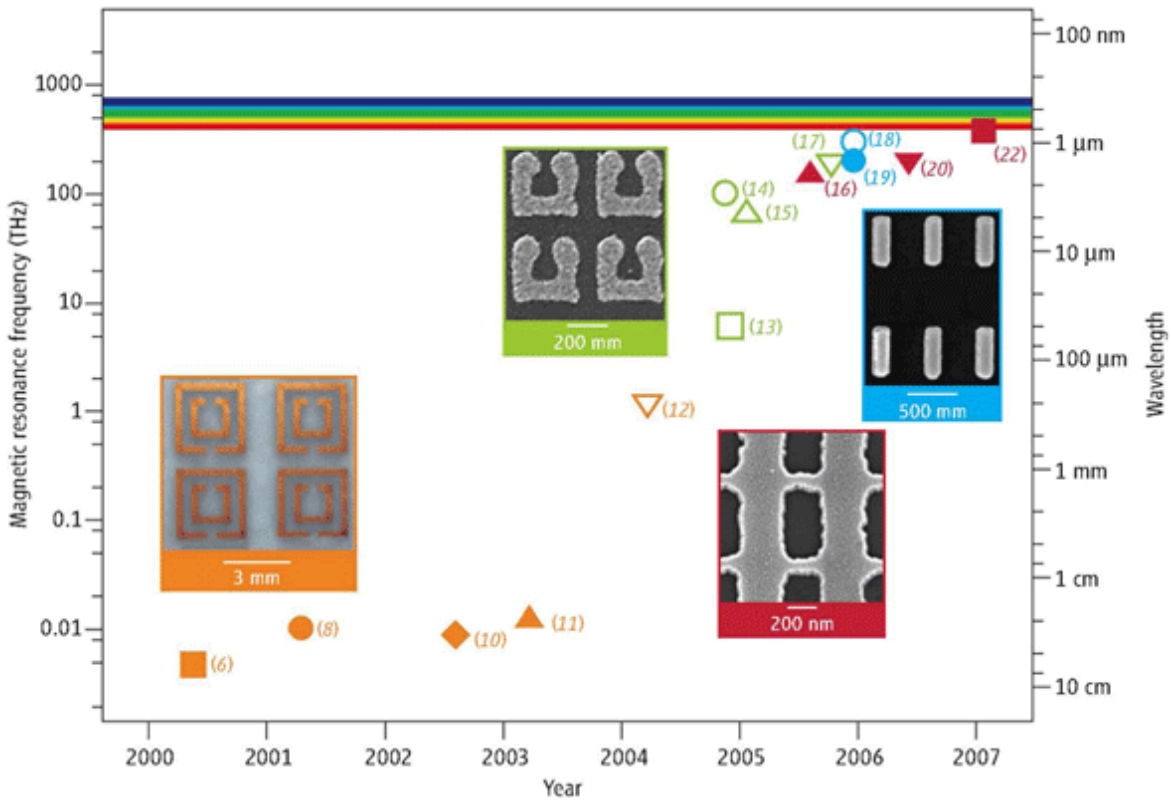

Figure 2.13: Plot charting the observation of artificially induced magnetic response at ever increasing frequencies. Reproduced from [*51*] with labels corresponding to references therein.

When trying to manipulate the propagation of light with these devices, the desire to achieve a strong response must be balanced with the need to avoid excessive absorption. This is especially true for 3D optical metamaterials.

Having explained the importance of charging effects in producing a subwavelength magnetic resonance, we should also note that such features act as a second source of radiation coupling. When an electric field is applied parallel to a dielectric gap which separates two metallic regions, an electric dipole moment can be induced[*52*]. This interaction is easily included in the effective medium description of a SRR metamaterial via an effective permittivity with a Lorentzian form similar to that of Eq.2.43. As the electric dipole is simply another mechanism by which radiation can couple to the fundamental *LC* resonance, it cannot have a separate resonant frequency. On the other hand, artificial electric and magnetic

dipoles, just like their atomic counterparts, can, and in general do, radiate with very different efficiencies. Unlike natural systems, however, metamaterial structures can be precisely tailored to achieve unprecedented material properties such as balanced ε_r and μ_r. For waves propagating along certain directions of high symmetry, the excitation of one or more dipoles may be forbidden, simplifying the response. When working at THz frequencies and above, for example, micro and nano-fabrication techniques are required. With these techniques non-planar designs are expensive, time consuming and often inaccurate. However, at normal incidence, the direct excitation of magnetic dipole moments associated with planar current loops is prohibited due to their alignment with the incident wavevector. Nevertheless, LC resonances can still be excited electrically, providing a convenient way to access such modes and the corresponding surface field enhancement[*53*]. For arbitrary directions, not only are both electric and magnetic dipoles expected to be simultaneously accessible, but the low symmetry of the light-matter interaction also leads to strong magneto-electric coupling. This phenomenon, termed bi-anisotropy, will be dealt with more thoroughly in the next section. We note finally that, although we have focussed on the dipolar modes of SRRs, higher order excitations such as electric and magnetic quadrupoles can also exist. While the radiation from these modes vanishes in the long wavelength limit, for structures with a finite size they cannot always be ignored.

2.3.4: Optical Activity and Chiral Meta-Structures

At the beginning of the 19th century, a number of prominent scientists, including Biot, Fresnel and Pasteur, began to explore a strange effect known as optical activity in which the plane of polarisation of light passing through particular substances gets rotated[*54*]. As

linearly polarised waves can be expressed as the superposition of circularly polarised components

$$\begin{pmatrix} E_x \\ E_y \end{pmatrix} = \frac{1}{\sqrt{2}}\left[\begin{pmatrix} 1 \\ i \end{pmatrix} + e^{i2\theta}\begin{pmatrix} 1 \\ -i \end{pmatrix}\right], \qquad [2.44]$$

where θ determines the orientation of the linear field, it is reasonable to conclude that optical activity results from circular birefringence, in which electromagnetic waves rotating clockwise and counter clockwise experience different refractive indices. Importantly, the shape swept out by a circularly polarised electric field, as the light propagates, is a helix.

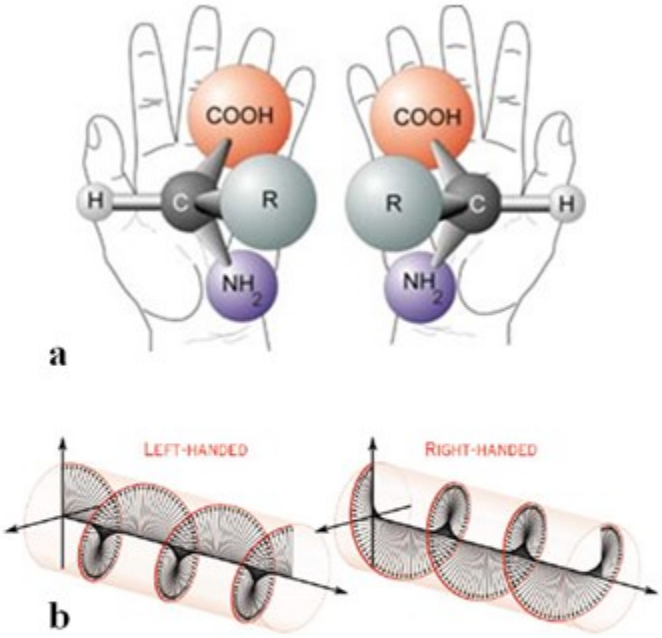

Figure 2.14: Symmetry, light and matter. a) Two enantiomers of a chiral amino acid[*113*]. b) Electric fields of circularly polarised light[*114*].

Such geometries are said to be chiral; a term coined by Lord Kelvin in 1893 to describe objects which are not superimposable on to their mirror image, coming from the Greek word for hand, as human hands have become the archetypal example of chirality. In fact, clockwise and counter clockwise polarisations, also known as left and right handed, are mirror images of each other. To explain the selective interaction with chiral light fields it was hypothesised

that optical activity originates from similarly chiral molecular structures. Louis Pasteur confirmed this theory in 1848 by measuring an equal but opposite optical rotation after separating out mirror symmetric partners, also known as enantiomers[*54*]. Nowadays, chirality is known to be incredibly important for determining the behaviour of chemical and biological systems and thus, optical activity has become an invaluable tool for analysis within many scientific fields. However, while a significant rotation can be measured for light passing through many wavelengths of a substance, natural molecules respond only very weakly $\Delta n_C = n_L - n_R \ll 1$, rendering them impractical for manipulating photonic polarisation states.

As for magnetism and anisotropy, metamaterials provide an ideal platform for enhancing circular birefringence. While symmetry arguments allow one to reason as to whether or not a given structure will be optically active, predicting the strength of this interaction requires an understanding of the underlying charge dynamics. If we assume that an object is much smaller than the relevant wavelength, we have already learnt that, to leading order, the response will be dominated by co-located electric and magnetic dipole moments, arising from accumulated charge and circulating currents, respectively. To selectively perturb a wave with a particular handedness, these induced dipoles must generate radiation that is orthogonally orientated and $\frac{\pi}{2}$ out of phase with respect to the incident wave. Without breaking Lorentz reciprocity, the necessary phase difference can only be achieved if electric (magnetic) dipoles can be excited by mutually aligned magnetic (electric) fields

$$\begin{pmatrix} \boldsymbol{p} \\ \boldsymbol{m} \end{pmatrix} = \begin{pmatrix} \alpha_e & i\kappa \\ -i\kappa & \alpha_h \end{pmatrix} \begin{pmatrix} \boldsymbol{E} \\ \boldsymbol{H} \end{pmatrix}, \qquad [2.45]$$

where the form of the off-diagonal elements is set by the reciprocal nature of the problem. This requirement provides a more concrete explanation of the need for chiral geometries. It is well known that magnetic and electric fields transform symmetrically and anti-symmetrically,

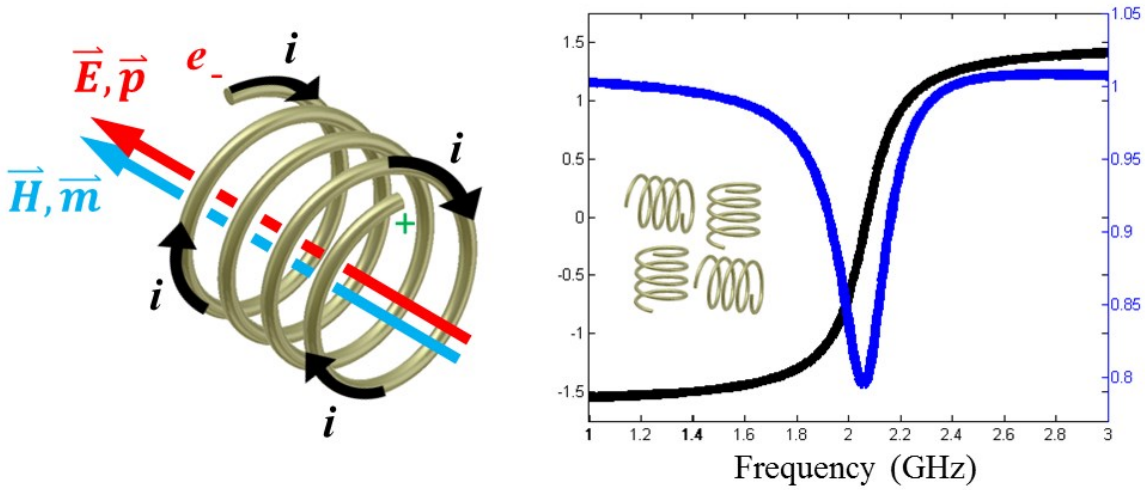

Figure 2.15: Chiral metamaterial. a) Magneto-electric coupling in a single helix. b) Simulated transmission spectra through helix array, blue curve (right *y* axis) showing circularly polarised transmission amplitude $|\boldsymbol{T_{ll}}|=|\boldsymbol{T_{rr}}|$ and black curve (left *y* axis) showing linear polarisation rotation angle in radians. The inset shows a single unit cell, including four coils to maintain four fold rotational symmetry thereby preventing circular polarisation conversion $\boldsymbol{T_{rl}} = \boldsymbol{T_{lr}} = \boldsymbol{0}$.

under spatial inversion, respectively; the overlap integral for these fields must therefore vanish without an asymmetric, or chiral, contribution from the environment. The principles described in this paragraph and at the end of (2.3.3) together point to an obvious route for structurally enhancing circular birefringence. Take for example, the simple case of an oscillating electric field incident upon an array of small metallic helices. As illustrated in Figure 2.15a, the axial components of the electric field can drive currents through the metal wires which in turn generate a set of axial magnetic dipole moments coming from loops in the wire geometry. The magnetic dipoles can then radiate with a $\pm\frac{\pi}{2}$ phase difference with respect to the initial excitation, depending on the handedness of the helices being used. The frequency dependence of this interaction can be described by the same LC circuit model as previously applied to SRRs. The simulated transmission of circularly polarised microwaves through such an array is shown in Figure 2.15b, clearly revealing a marked difference for just a single layer. Although the helical geometry has a definite handedness, we can see that the optical activity changes sign across the resonance. This can be reasoned by considering the Lorentzian frequency dependence. While $\boldsymbol{p}$ and $\boldsymbol{m}$ have a fixed relationship with each other,

for ω above the resonant frequency, the dipoles oscillate out of phase with respect to the incident wave, mimicking the effect of structural inversion. Despite the fact that chirality is an intrinsic geometrical property of an object, it is important to note that waves propagating along the axis of the coils in Figure 2.15 experience no optical activity. This highlights the polarisability as the fundamental property which must always be considered when designing photonic metamaterials. Such magneto-electric coupling can be treated within an effective medium description via the constitutive relations[*55*, *56*]

$$\boldsymbol{D} = \varepsilon_0 \varepsilon_r \boldsymbol{E} - i\frac{\gamma}{c}\boldsymbol{H} \quad [2.46]$$

$$\boldsymbol{B} = \mu_0 \mu_r \boldsymbol{E} + i\frac{\gamma}{c}\boldsymbol{E}. \quad [2.47]$$

After applying Eqs.2.46-2.47 to Eqs.2.18-2.21, for an isotropic chiral medium, circularly polarised wave solutions can be found with refractive indices

$$n_{L/R} = \sqrt{\mu_r \varepsilon_r} \pm \gamma. \quad [2.48]$$

From Eq.2.48 we can see that a strong chiral response $\gamma^2 > \mu_r \varepsilon_r$ can also lead to a negative refractive index without the need for negative permeability or permittivity[*57*]. For many groups this result has been a key motivation for the development of artificial chiral materials, especially at high frequencies[*55–58*].

While 2D chiral designs, such as SRRs, exhibit magneto-electric coupling, restricting the induced currents to lie in the plane forces the corresponding magnetisation to point in the normal direction. A differential response to circularly polarised radiation must therefore be absent at normal incidence as only the in plane electric dipoles can be excited. For oblique incidence, however, it has been demonstrated that optical activity can occur if the electric and magnetic dipoles share a common field component when projected onto the plane $\boldsymbol{k} \cdot \boldsymbol{B} = \boldsymbol{k} \cdot \boldsymbol{E} = 0$. On the other hand, the mirror symmetry that necessarily exists for such 2D

geometries, if we ignore the small effect coming from the difference in permittivity of the super and substrates, must cause the discrimination between left and right handed polarisations to cancel globally, i.e. for any given direction there must exist a partner in which the optical rotation is equal and opposite. As 3D micro and nano structures are very challenging to fabricate, artificially realising a true chiral response at high frequencies requires the employment of more imaginative designs. A particularly popular approach for overcoming these difficulties has been to create bilayer structures[*56*, *59*, *60*], as shown in Figure 2.16, in which closely spaced 2D resonators are capacitively and/or inductively coupled together. While complicated circuit models can be used to describe their electromagnetic

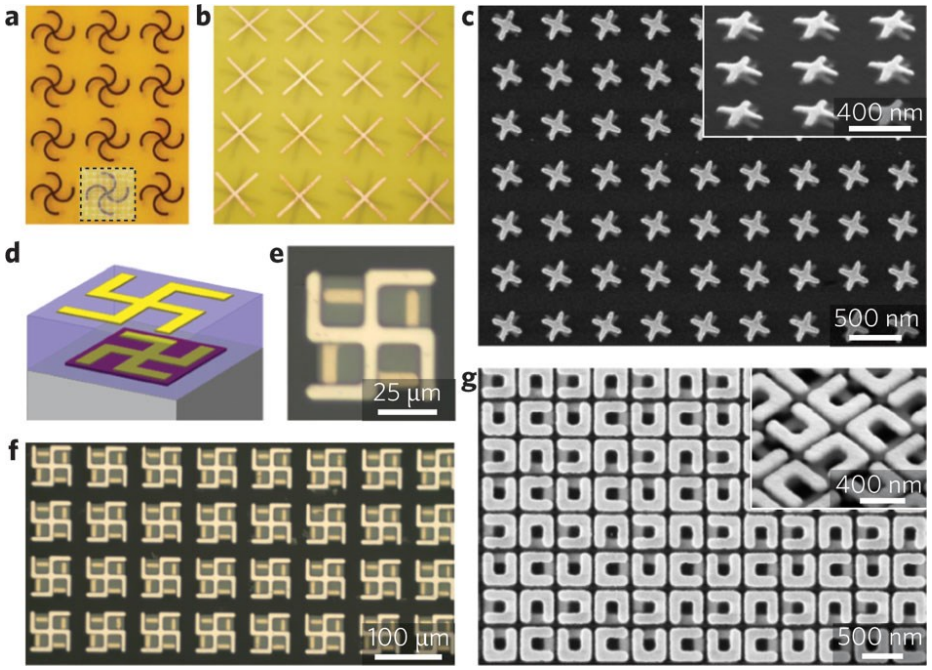

Figure 2.16: Examples of bilayer chiral metamaterials from microwave (a,b) and terahertz (d,e,f) frequencies up to the optical regime (c,g). Reproduced from [*51*] with sub figures found in references therein.

response, a more abstract hybridisation picture is perhaps more useful for understanding the qualitative behaviour of such a system. As will be discussed in greater detail in the following section, coupling between two resonators leads to the occurrence of two new resonant features at different frequencies. It can also be shown that one of these modes consists of a symmetric combination of in plane electric and magnetic dipoles, while the other possesses

an antisymmetric configuration. Interference between the two modes in these bilayer designs therefore produces a less dispersive and more broadband chiral response than the simple coil geometry shown in Figure 2.15. Finally, we note that pure optical rotation only occurs for lossless systems with four-fold rotational symmetry about the propagation direction. When loss is considered Δn_C can possess an imaginary part, describing the differential absorption of left and right circular polarisations. By inspecting Eq.2.44 we can see that this phenomenon, commonly referred to as circular dichroism, will cause a linearly polarised incident wave to become elliptical rather than simply rotated. For chiral structures with low rotational symmetry, the off-diagonal elements of the Jones matrix in the circularly polarised basis become non-zero, meaning that the transmission of circularly polarised light cannot be described by the refractive index alone. In fact, it has been shown that such metamaterials with low symmetry can be used to induce a differential circular response even for a 2D, and therefore non-chiral, setting[*61*]. This is possible because the conversion between LCP and RCP light can be non-reciprocal.

2.3.5: "Meta-Molecules" from Coupled "Meta-Atoms"

In sections (2.3.3/4) we have focussed on the creation of manmade electromagnetic dipole moments. We have seen that an ability to structurally manipulate the flow of charge on a subwavelength scale allows the properties of these dipoles to be chosen almost arbitrarily. Often, simple designs which exhibit spectrally isolated Lorentzian resonances are employed, allowing a strong analogy to be drawn between meta-structures and atomic dipole transitions. However, this is but one of many possible excitations that can be found in nature. The energy levels associated with a complex molecule, for example, can reveal a rich variety of

behaviour. Rather than solving Schrödinger's equation for the entire molecule, physicists commonly view the eigenstates of such a system as mixtures of well-known atomic orbitals.

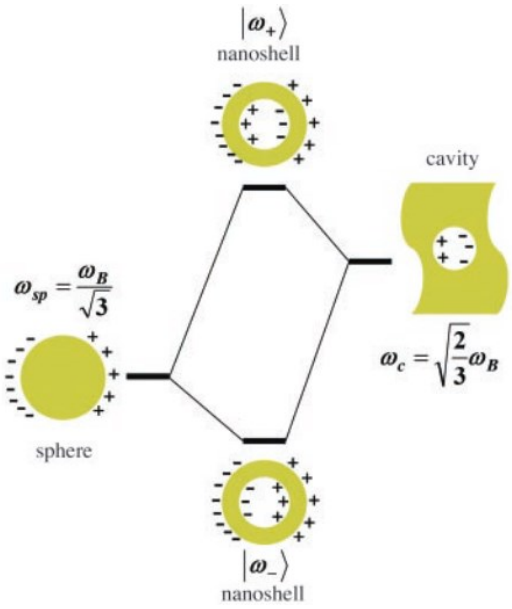

Figure 2.17: Plasmonic hybridisation model, reproduced from Ref[*62*]**.** Resonant frequencies of metallic nanorings can be predicted from analytical solutions of isolated metal spheres and cavities.

In 2003 Prodan *et. al.* applied the same principle to the analysis of plasmonic resonators[*62*]. They showed that the resonant features of a complicated metallic structure could be predicted by representing them as a hybridisation between modes of simpler geometries. This approach provides a powerful conceptual tool for designing novel metamaterials. In essence, it means that understanding the response of just a few basic objects or "meta-atoms" such as spheres, rods and rings, as well as knowing the rules that govern their interactions; a plethora of intricate "meta-molecules" can be modelled with ease.

In the simplest case of two identical oscillators with resonant frequencies ω_0, coupled together via a near-field interaction of strength ξ, two hybrid solutions emerge with the same Lorentzian form as for $\xi = 0$ given in Eq.2.42, but with mode frequencies $\omega_\pm = \omega_0/\sqrt{1 \mp \xi}$[*63*]. These new states correspond to symmetric and antisymmetric, i.e. in and out of phase, combinations of the component resonators meaning that their ability to radiate,

which depends strongly on the chosen configuration, can be very different. For example, the far field response of the antisymmetric mode for a subwavelength pair of parallel nanorods can be completely suppressed while the response of the symmetric mode is actually enhanced. More exotic hybridisation effects occur when the sub systems are not identical but instead have very different properties. For instance, when a narrow resonance is coupled to a relatively broad feature, i.e. a resonance with a much bigger dissipation coefficient, located at a different frequency it develops an asymmetric dispersion which is given approximately by

$$I \propto \frac{(F\gamma + \omega - \omega_0)^2}{(\omega - \omega_0)^2 + \gamma^2}. \qquad [2.49]$$

This is known as Fano resonance, named after Ugo Fano who derived Eq.2.49 in 1961 to explain atomic auto-ionisation observations[*64*]. Specifically, he considered the interference between scattering from a discrete Lorentzian excitation and a background continuum of

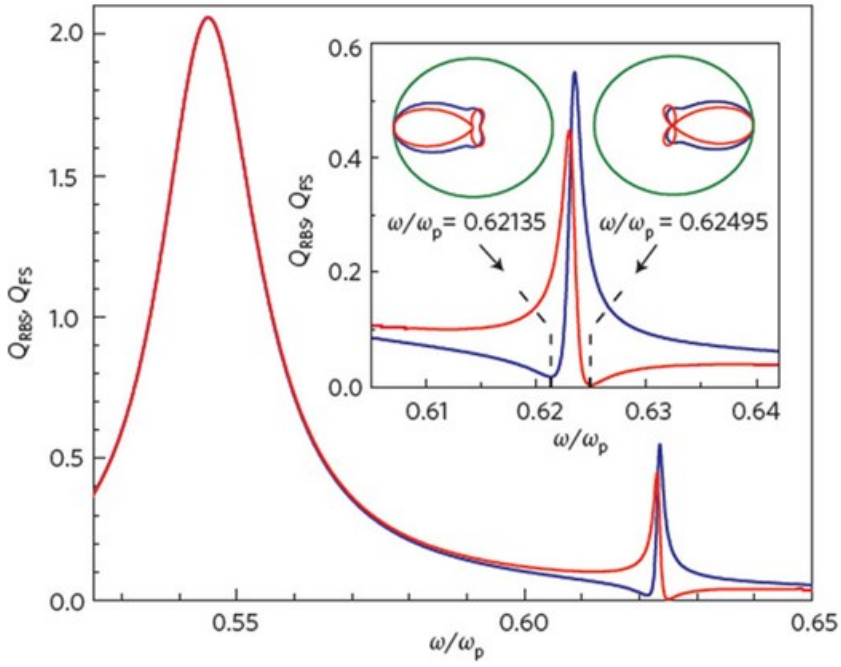

Figure 2.18: Mie scattering from a metallic sphere. Red and blue curves represent back and forward scattering, respectively. The interaction between the low frequency dipole and high frequency quadrupole resonances can be seen to produce a Fano line shape[*64*].

states. However, slow amplitude and phase variation rather than a precisely flat continuum is sufficient to produce this form of asymmetric line shape. As such a condition is satisfied by a broad response away from resonance, Fano spectral features turn out to be ubiquitous in plasmonics[*64*]. An example showing the interaction between the dipole and quadrupole modes of a metallic nanoparticle can be found in Figure 2.18. Due to the steep gradient found in these dispersion curves it has been suggested that they could be used for improving plasmon based sensors and switches[*65*]. Another metamaterial system which makes use of differences in meta-atom dissipation has also received a lot of attention recently. In this case, a bright mode which radiates strongly to the far field is coupled to a dark mode, from which radiation is completely suppressed, with the same resonant frequency. Such a metastructure is

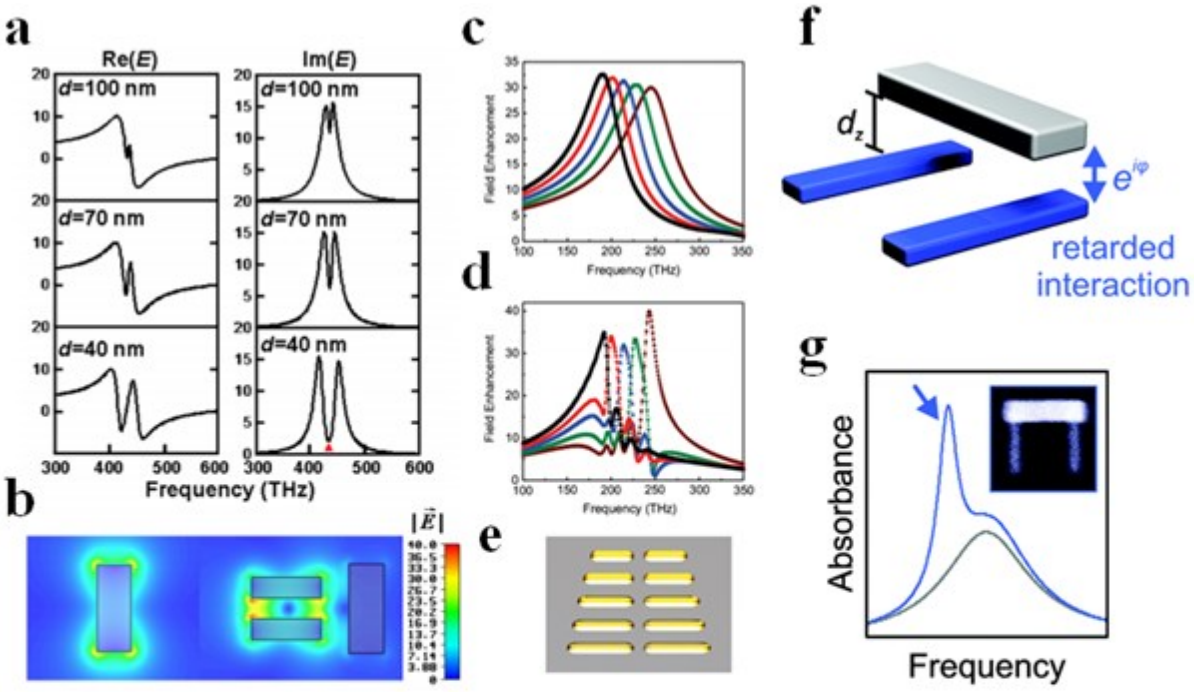

Figure 2.19: Coupled metamolecules. a) *E*-field near bright metaatom for different separations and therefore coupling strengths b) *E*-field patterns at central frequency for isolated nanorod (left) and EIT metamolecule (right) c) isolated resonant field enhancements for nanorods in 'e' d) anti-Hermitian coupling narrowed field enhancements for structure in 'e' f) retarded coupling between dipolar mode of nanorod and quadrupole mode of nanorod pair. g) electromagnetically induced absorption from structure in 'f'[*66–68*].

shown in Figure 2.19b. As revealed in Figure 2.19a, a sharp transparency window opens in the transmission for large coupling strengths caused by destructive interference between the field

incident on the bright nanorod and the feedback from the dark nanorod pair. This can be seen as an analog of electromagnetically induced transparency (EIT) found in three level atomic systems. Most interestingly, the sharp spectral feature combined unity transmission leads to a huge reduction in the group velocity which could be useful for nanoscale slow light applications[*66*].

Above we have focussed on ways in which the dissipation of the meta-atoms themselves can lead to interesting meta-molecule states. However, the imaginary part of the coupling coefficient can also provide an extra degree of freedom. While quasistatic near-fields dominate the interaction for closely spaced antennas, ensuring that $Im(\xi) = 0$, as they are moved further apart retardation of the field leads to $\xi \propto e^{ikd}$, where d is the antenna separation. In Ref[*67*] the structure illustrated in Figure 2.19f, which is the same as the one used in Ref[*66*] except that ξ is complex, was shown to produce electromagnetically induced absorption, Figure 2.19g. Furthermore, in Ref[*68*] it was revealed that the indirect coupling between two nanorods through a shared radiation channel leads to an imaginary, anti-Hermitian ξ. This can narrow the response of spectrally overlapping resonances, shown in Figure 2.19c/d, allowing for selective excitation of closely spaced nanoparticles.

2.4: Chapter Summary

Throughout this chapter we have outlined the conceptual tools and key mathematical details required for discussions in the following chapters. Starting with quantum mechanics in (2.1), single particle Hamiltonians, dependant on a set of parameters, were investigated. After introducing the idea of geometric, or Berry, phases and topological invariants, the guaranteed one-way excitations at boundaries between topologically trivial and nontrivial crystals were analysed. The occurrence of spontaneous symmetry breaking in complex *PT* symmetric problems was also highlighted. Next, in section (2.2) an overview of wave solutions to the

macroscopic Maxwell's equations for natural phenomena including birefringence and surface waves was provided. Finally in (2.3) a summary of the experimental and theoretical aspects of the field of photonic metamaterials was presented. As well as explaining the general principles behind artificial electric and magnetic materials, an emphasis has been placed upon polarisation dependant propagation in anisotropic and bianisotropic media, including hyperbolic and chiral metamaterials.

Chapter 3: Metasurfaces, What Can Be Gained From Loss?

Part of the work presented in this chapter has been published in [*69*], for which I was personally responsible for writing the first draft. The chapter includes blocks of text taken from this publication.

When attempting to manipulate the flow of light, dissipative processes which convert electromagnetic energy into other forms, such as thermal or mechanical motion, are often considered to be unwanted side-effects. This is especially true in the field of metamaterials, as discussed in (2.3), where a reliance on metallic structures, which are inherently absorptive, limits potential applications to those operating over short distances or with weak output signals. In fact, plasmonic losses are often quoted as the main reason for the lack of real world meta-devices at visible frequencies. In this chapter, we will investigate a new set of phenomena which occur because of, rather than in spite of, dissipation. Drawing inspiration from discoveries made during theoretical studies into non-Hermitian quantum operators, described in (2.1.4), the design principles outlined in (2.3) will be applied to the development of non-Hermitian, anisotropic metasurfaces.

After reviewing previous work regarding electromagnetic analogues of quantum systems with spatially varying dissipation, the consequences of *PT* symmetry breaking and exceptional point mode coalescence for the response of an effectively homogeneous medium will be discussed. In particular, novel functionalities including polarisation phase transitions and spectral singularities have been found, providing a new degree of freedom for controlling

polarisation states of light. As well as modelling our designs using FDTD simulations, experimental verification has been carried out at THz frequencies using THz-TDS.

3.1: Introduction to *PT* symmetric Electromagnetics

As explained in (2.1.4), non-Hermitian quantum mechanical Hamiltonians which are invariant under the simultaneous transformations of parity and time-reversal can possess either real or imaginary eigenvalues. Most interestingly, the variation of some external parameter can actually cause such a system to transition suddenly from one type of solution to the other, altering its dynamical behaviour dramatically. Unfortunately, the requirement for a precisely balanced potential energy landscape $V(\boldsymbol{r}) = V^*(-\boldsymbol{r})$ makes experimentally validating these models incredibly challenging. However, a few years after Bender's theoretical investigation, Guo *et al* provided a classical electromagnetic demonstration[*70*]. By exploiting the formal equivalence between the time dependent Schrödinger equation, Eq.2.1, and the optical wave equation within the paraxial approximation

$$-i\frac{\partial E}{\partial z} = \frac{1}{2n_0k_0}\frac{\partial^2 E}{\partial x^2} + k_0 n(x)E, \qquad [3.1]$$

where k_0 is the free-space wavenumber and $n(x)$ is the deviation from the background refractive index n_0. Here, variations in the electric field profile as the beam propagates along the spatial z coordinate can be seen to mimic the temporal evolution of a quantum particle. $k_0 n(x)$, therefore, plays the role of an optical potential. Clearly, Eq.3.1 is *PT* symmetric if $n(x) = n^*(-x)$. To satisfy this condition non-trivially, i.e. $n(x) \neq n(-x)$, two single mode waveguides constructed out of dielectric materials with $n_{1,2} = n_r \pm in_i$ can be placed side by

side. For convenience, the propagating solution within each waveguide $E_{1,2}(x,y,z) = U_{1,2}f_{1,2}(x,y)e^{i\beta_{1,2}z}$ can be used as the basis for a set of coupled mode equations

$$i\frac{\partial}{\partial z}\begin{pmatrix}U_1\\U_2\end{pmatrix} = \begin{pmatrix}\beta_1 & \kappa\\ \kappa^* & \beta_2\end{pmatrix}\begin{pmatrix}U_1\\U_2\end{pmatrix}, \qquad [3.2]$$

where κ is given by the overlap integral between the fields E_1 and E_2 for a given separation distance. The eigenvalues of Eq.3.2 are given by

$$k_z = -\left(\frac{\beta_1+\beta_2}{2}\right) \pm \sqrt{|\kappa|^2 + \left(\frac{\beta_1-\beta_2}{2}\right)^2}. \qquad [3.3]$$

From this expression, we can see that if $\beta_2 = \beta_1^*$ spontaneous *PT* symmetry breaking occurs upon varying κ or $Im(\beta_1)$. For $|\kappa| > |Im(\beta_1)|$, k_z is real and the eigenmodes propagate through the double channel structure without dissipating. While the eigenmodes evolve unitarily however, if energy is injected into just one port, the non-orthogonality of the associated fields given by $(U_1, U_2) = (1, \pm exp(\pm i \sin^{-1}(Im(\beta_1)/\kappa)))$, which is a

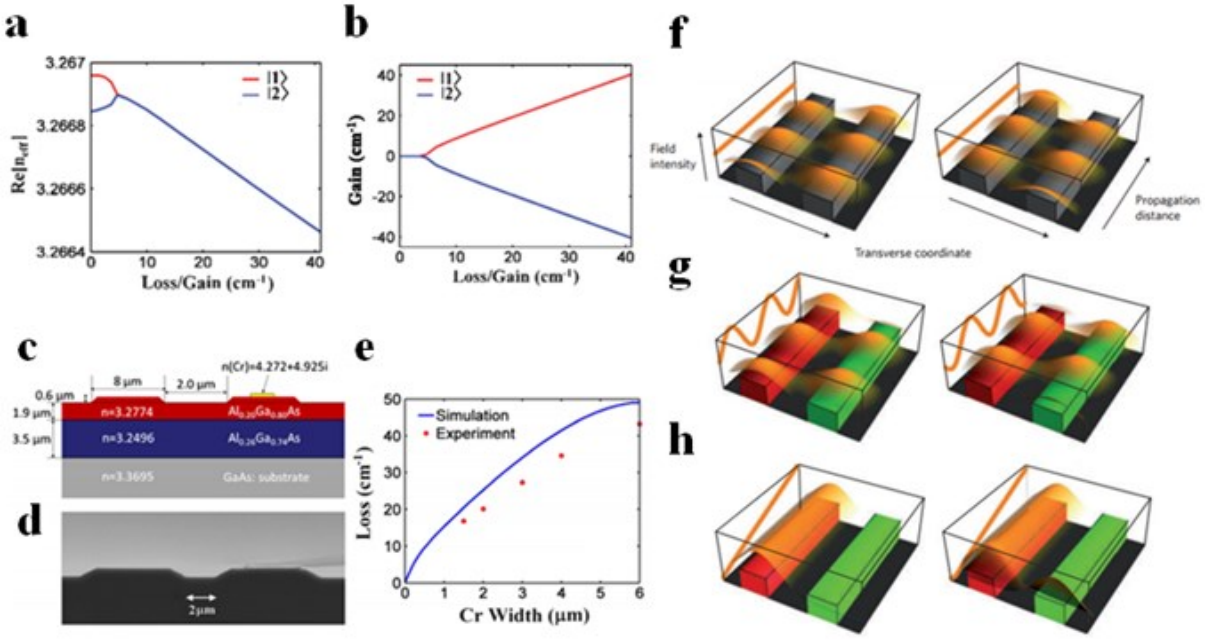

Figure 3.1: Side coupled *PT* symmetric waveguides. a) Effective refractive indices and b) dissipation factors for coupled eigemodes. c) Schematic and d) SEM image of *PT* waveguide design. e) Plot of dissipation factor for ridge waveguide mode of structure on right hand side of c and d with varying width of Chromium strip[*70*]. f-h) Transmitted optical field through coupled waveguide pair, with energy injected into left guide for left column and right guide in right column. f) Lossless waveguides. g) *PT* waveguides, red=gain and green=loss, in exact phase. h) *PT* waveguides with broken *PT* symmetry. The orange curves represent the total optical power[*115*].

consequence of working with a non-Hermitian Hamiltonian, causes the total optical power to oscillate as a function of z[*70*, *71*]. What's more, the efficiency with which energy is converted between the two channels, after propagating a given distance, depends strongly on which port has been excited. When $\frac{|\kappa|}{|Im(\beta_1)|}$ drops below the EP $|\kappa| = |Im(\beta_1)|$, the qualitative behaviour of the system changes; with k_z being complex and the eigenvectors becoming $(U_1, U_2) = (1, iexp(\mp \cosh^{-1}(Im(\beta_1)/\kappa)))$, the transmission of light through the system becomes dominated by the amplifying waveguide $Im(\beta) < 0$. In this case, the asymmetry in the response is further accentuated, with the light always exiting via the same waveguide. Although the exact *PT* symmetric condition $n_i(x) = -n_i(-x)$ can only be satisfied with loss and gain, even with $Im(\beta_{1,2}) > 0$ Eq.3.3 still reveals a bifurcation in k_z as long as $Re(\beta_1) = Re(\beta_2)$ and $Im(\beta_1) \neq Im(\beta_2)$. This can be understood by the fact that a simple gauge transformation allows a common decay factor $(Im(\beta_1) + Im(\beta_2))/2$ to be extracted, retrieving a mathematical description identical to that of an active system. In these passive *PT* structures increasing the amount of absorption can have the counter intuitive effect of increasing the transmitted power[*70*].

The coupled mode approach discussed above highlights the power of modern optical engineering methods as a platform for exploring such subtle wave phenomena. The parity operator $P = x \rightarrow -x$, constrains the real and imaginary parts of the index profile to be precise symmetric and antisymmetric functions of position, respectively, for Eq.3.1 to be *PT* invariant. On the other hand, Eq.3.2 only requires the effective mode indices associated with the two waveguides to be balanced $\beta_2 = \beta_1^*$, irrespective of the particular designs being used. This is important because even with the wide array of optical materials available, finding two with exactly the same $Re(n)$ is difficult. Engineering a specific complex effective index on the other hand, by borrowing techniques from the semiconductor electronics industry, is

fairly straightforward. In [*70*] for example, a thin Chromium strip was added to just one of a pair of ridge waveguides fabricated on top of an AlGaAs heterostructure, as shown in Figure 3.1c,d. By making a number of samples with different strip widths the absorption coefficient of one of the guided modes could be varied, shown in Figure 3.1e, allowing the phase transition to be mapped out. Later, an exact *PT* transition was demonstrated by selectively pumping one of two optical channels within a photorefractive substrate made from Fe-doped $LiNbO_3$[*71*].

As discussed above, for a pair of side coupled waveguides with balanced loss and gain, the presence of non-orthogonal eigenstates leads to pronounced asymmetric mode

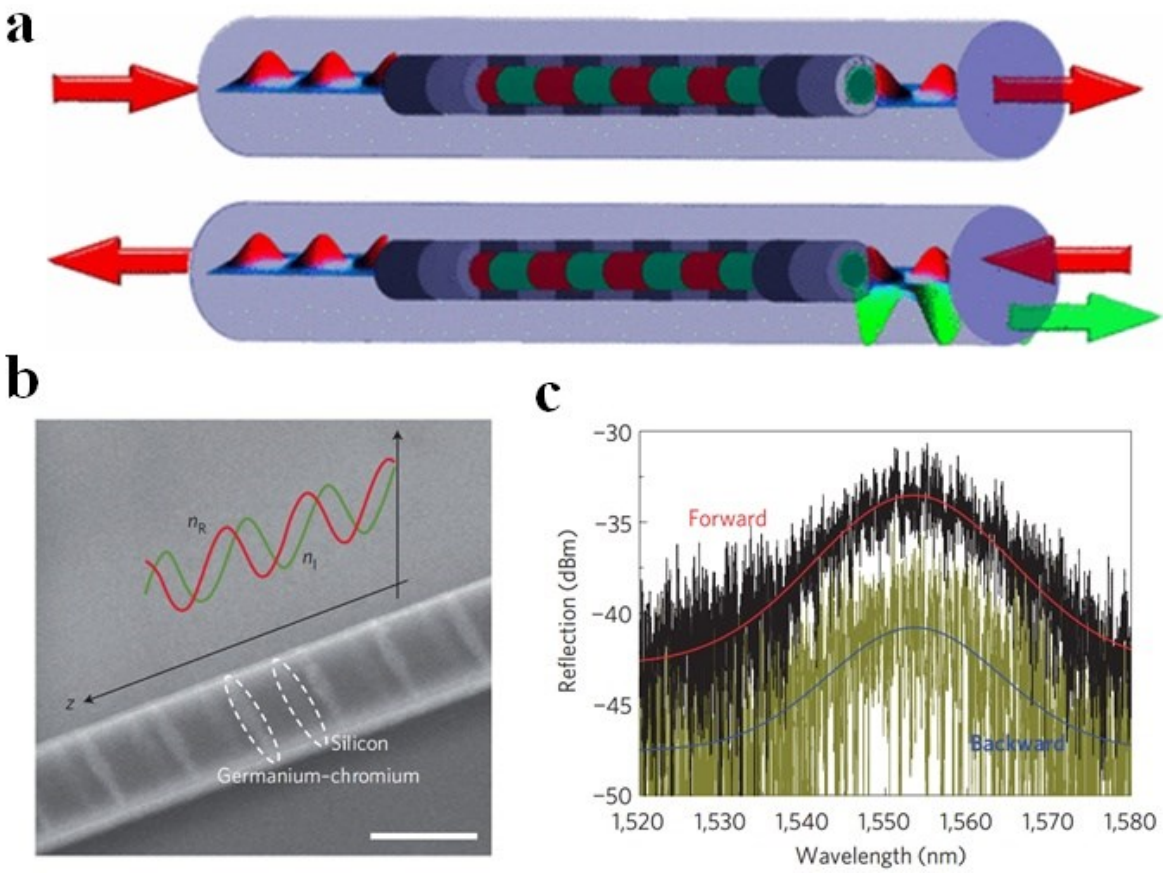

Figure 3.2: Unidirectional transparency in *PT* symmetric Bragg gratings. a) Schematic representation of *PT* Bragg grating with a loss-gain modulation depth corresponding to an EP. While the transmission is always unity, the reflection only goes to zero for left incident waves. b) SEM image of passive *PT* structure. c) Directionally dependant reflection measurement of sample shown in "c". "a" and "b, c" reproduced from Refs [*72*] and [*73*], respectively.

conversion. In other work, this asymmetry was shown to have interesting consequences for the reflection of light from a periodic arrangement of a similarly *PT* symmetric refractive index modulation along the propagation direction[*72*]. While the transmission through such a structure must be reciprocal, the reflection can varying depending on which side is being illuminated. Remarkably, the EP eigenmode coalescence, which occurs for a particular ratio between the modulation depths of the real and imaginary parts of the refractive index, causes reflections to vanish but from only one side, shown in Figure 3.2a. Essentially, in this configuration, the absorbing medium exactly cancels the Bragg scattered field in one direction, while in the opposite direction the field is enhanced by the amplifying medium. As unitary transmission is maintained for an active system, such a structure is said to be unidirectionally invisible. In 2012, Feng *et al* provided a demonstration of this phenomenon in a passive experiment involving an intricate Silicon waveguide design[*73*], shown in Figure 3.2b. Although the incident light could of course not be transmitted perfectly, strong directionality in the reflected signal was observed, shown in Figure 3.2c.

Inspired by the useful properties discovered with surprisingly simple *PT* setups, researchers have also begun to explore wave dynamics in lattice systems with loss and gain[*74–76*]. In this case, new effects including nonreciprocal Bloch oscillations[*74*] and double negative refraction[*75*] have been predicted. While precisely balanced complex index variations are difficult to fabricate in 2 or 3 dimensions, a particularly interesting way of investigating such structures has been demonstrated using a pair of coupled optical fibre loops[*77*]. By tuning the difference in length between the loops and dynamically modulating the amplitude and phase of a circulating pulse, wave propagation through a whole host of spatial networks can be modelled as purely temporal changes. Not only does this method represent an elegant tool for simulating *PT* arrays, but it may also lead to novel pulse shaping functionalities enabled by mapping from real space behaviour. As well as revealing new

physics, recently, *PT* symmetric optical devices have also been proposed including CPA-laser/absorbers[*78*] and lasing mode suppression[*79*].

At this point we should note that non-Hermitian dynamics and the physical consequences of exceptional points were explored long before Bender and colleagues formulated their proposed extension to quantum theory. In 1902, Voigt, and Pancharatnam in a later re-examination, showed that light propagating in certain directions through an absorbing biaxial crystal would experience a non-Hermitian permittivity tensor. They also found that along certain "singular axes" only one circularly polarised eigenstate exists. Based on geometric arguments, Pancharatnam hypothesized that an orthogonally polarised wave incident in this direction would, contrary to Voigt's belief that perfect reflection should occur, be slowly converted to the eigenstate while propagating through the crystal[*80*]. Pancharatnam's prediction was confirmed by measurements showing that the transmitted intensity is actually greatest for circularly polarised incidence with the opposite handedness to that of the eigenmode[*81*]. It is exactly this form of light-matter interaction which will be the focus of the following sections in this chapter. Not only will we reveal how metamaterials provide a convenient way of engineering and enhancing such properties, but also how they make novel phenomena, such as arbitrarily polarised singular waves, accessible. More recently, EPs have also been observed in microwave cavity experiments where the spatial structure of the resonances involved could be analysed in great detail[*82–84*].

3.2: Numerical Treatment of Metasurfaces

Throughout this chapter, we will rely heavily on the coupled dipole approximation to engineer and understand the response of our metastructure designs. However, before proceeding to experimental demonstrations of any phenomena that have been predicted, numerical full-wave simulations will be performed to provide an accurate forecast of the

outcome. Specifically, the transient and frequency domain solvers within the commercial software package CST Microwave Studio™ will be employed. The transient solver makes use of the finite difference time domain method which tracks the temporal evolution of an initial field distribution by solving the time dependant Maxwell's equations on a discrete hexahedral grid. By setting up a plane wave excitation for a single unit cell with periodic boundary conditions, the interaction between a Gaussian photonic beam and a large periodic metasurface can be well approximated. When oblique incidence is required, the frequency solver, which relies on the finite element method to solve Maxwell's equations at discrete frequencies, will be used in conjunction with Floquet waveguide ports. As only THz devices will be considered in this chapter, metallic objects will be represented by lossy Drude permittivities, parameterised in terms of their DC conductivities. The silicon substrate will be described as a lossless, dispersionless dielectric $\varepsilon_s = 11.7$.

3.3: Metasurface Fabrication and Characterisation

Changes to photonic polarisation states that occur after interacting with artificial structures will form the main focus of investigations in the following sections. However, it is the specific polarisation eigenstates that will be important, not just the transmission or conversion efficiencies in a particular basis. In order to determine these eigenstates, the phase of the transmitted light must be measured. A technique known as Ellipsometry, in which polarising components are varied dynamically, can provide the relative phase between TE and TM transmitted waves resulting from a particular incident polarisation. However, the lack of information regarding the absolute phase still makes determining the full Jones matrix complicated and besides, commercial versions of such systems are unavailable at THz

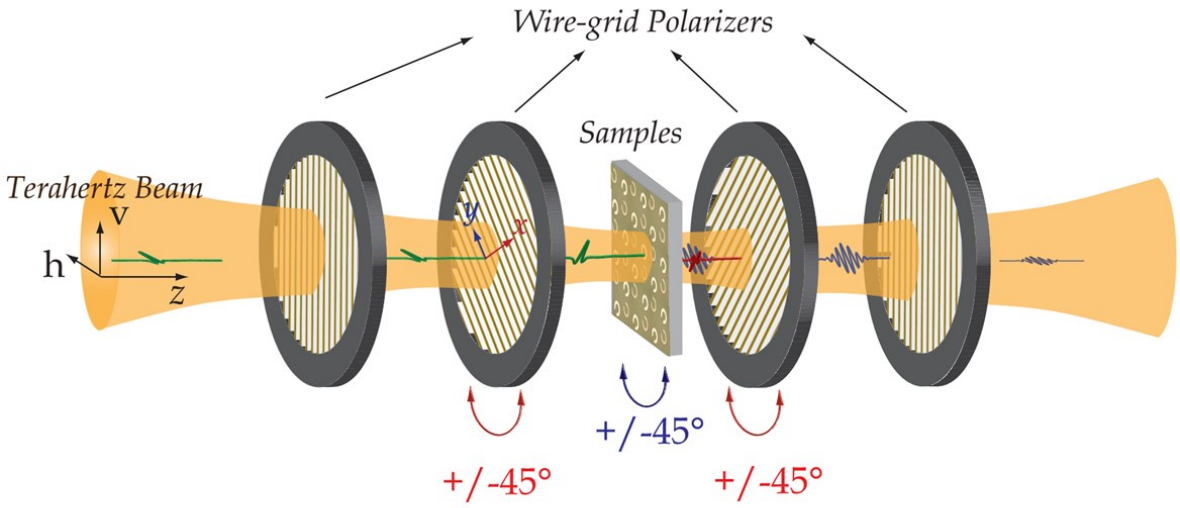

Figure 3.3: Schematic representation of polarising configuration. By rotating the second and third wire-grid polarisers to +45° or -45° with respect to the first and fourth polarisers, which share the same alignment, all four linear transmission coefficients, $\tilde{t}_{xx}$, $\tilde{t}_{yy}$, $\tilde{t}_{yx}$ and $\tilde{t}_{xy}$ can be measured.

frequencies, our desired regime due to the favourability of metallic properties. Instead we have chosen to use Terahertz time domain spectroscopy (THz-TDS) which allows the time dependant electric field strength of a terahertz pulse, emitted by a photoconductive antenna, to be measured after passing through a sample. Specifically, the system consists of four parabolic mirrors placed between the transmitter and receiver which are arranged in an 8-F confocal geometry enabling a frequency independent beam waist of ~5mm at the sample. After taking the Fourier transform of the time signal and normalising against transmission through the bare substrate $\tilde{t} = \tilde{E}_{sample}/\tilde{E}_{ref}$, this measurement results in a complex transmission spectrum. Finally, the anisotropy of our metasurfaces requires this process to be repeated for the four possible linear input/output polarisation combinations, Figure 3.3.

Metallic structures that are resonant in the THz regime tend to be tens of micrometres in size. We have therefore employed photolithography to fabricate our designs. As shown in Figure 3.4, a separate chrome mask was first created for each ring geometry and then used to expose a negative photoresist on top of a silicon substrate. After evaporating a thin $\sim 300nm$ layer of silver, lead or gold, the process is completed by lifting off the remaining photoresist

to leave an array of isolated metal structures. Where more than one metal is required, the

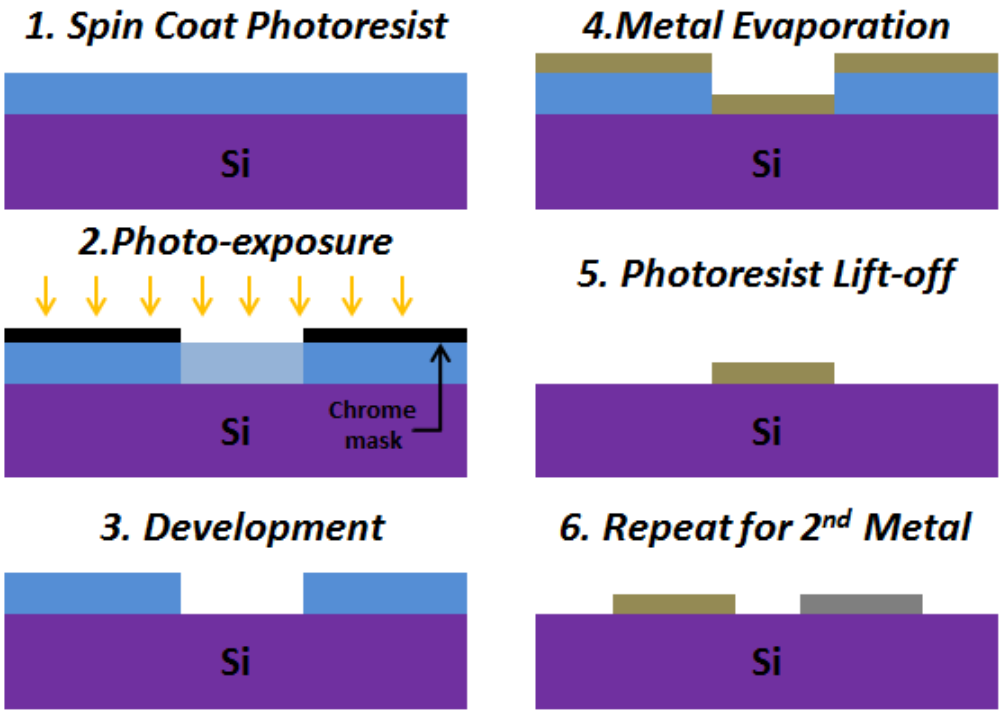

Figure 3.4: Illustration of the fabrication steps used to create metasurface samples.

previous steps are repeated using alignment marks on the photomask to achieve a specified separation between objects made from the different materials.

3.4: Manifestation of *PT* Symmetry Breaking in Polarisation Space

As described in (3.1), up until now photonic investigations of *PT* symmetry breaking have for the most part, focussed on diffraction from index variations satisfying the condition $n(\boldsymbol{r}) = n^*(-\boldsymbol{r})$. However, the mathematical structure underpinning the interesting physics observed in these experiments is not uniquely related to spatial symmetry. Any dynamical system in which the rate of decay varies under the action of some field transformation must be governed by a non-Hermitian differential operator. With this in mind, here we decide to

focus on another photonic degree of freedom, namely the electromagnetic polarisation. While the importance of symmetry and symmetry breaking for enhancing optical activity, asymmetric transmission, birefringence etc. has been thoroughly investigated, much less effort has been directed towards understanding the role played by loss. As well as representing a fundamentally new approach to exploring *PT* concepts, we also therefore, expect the current study into carefully balanced polarisation dependent dissipation to provide useful insights for the development of future photonic devices.

Restricting our discussion to monochromatic plane wave propagation, all possible solutions can be written in the form of frequency dependent Jones vectors

$$\boldsymbol{E} = \begin{pmatrix} \tilde{E}_x(\omega) \\ \tilde{E}_y(\omega) \end{pmatrix} = \begin{pmatrix} E_x(\omega)e^{i\varphi_x(\omega)} \\ E_y(\omega)e^{i\varphi_y(\omega)} \end{pmatrix}. \quad [3.4]$$

In general, these states correspond physically to electric fields which sweep out elliptical shapes as time progresses. Ignoring the overall intensity, any given polarisation ellipse can be expressed by two key geometrical parameters, the orientation angle ψ defined via

$$\tan 2\psi = \frac{2E_xE_y}{E_x^2 - E_y^2}\cos(\varphi_y - \varphi_x) \quad [3.5]$$

and the ellipticity angle χ defined via

$$\sin 2\chi = \frac{2E_xE_y}{E_x^2 + E_y^2}\sin(\varphi_y - \varphi_x), \quad [3.6]$$

shown in Figure 3.5a. Throughout this chapter, Jones vectors associated with theoretically and experimentally obtained transmission data will be plotted on the Poincare sphere, shown in Figure 3.5b, which is a convenient graphical representation with ψ and χ as polar coordinates. Any alteration to the state of a wave, taken here to be travelling in the z direction, after interacting with some photonic device can then be accounted for by the action of a 2×2 matrix

$$\widetilde{\boldsymbol{E}}_{\boldsymbol{t}} = \begin{pmatrix} \tilde{t}_{xx} & \tilde{t}_{xy} \\ \tilde{t}_{yx} & \tilde{t}_{yy} \end{pmatrix} \widetilde{\boldsymbol{E}}_{\boldsymbol{i}} = \hat{\boldsymbol{J}}_{\boldsymbol{t}} \widetilde{\boldsymbol{E}}_{\boldsymbol{i}}, \qquad [3.7]$$

as explained at the end of (2.2.3). In general, $\tilde{t}_{xx}$, $\tilde{t}_{yy}$, $\tilde{t}_{yx}$ and $\tilde{t}_{xy}$ are complex and different. Problems involving polarisation modification are typically, therefore, non-Hermitian. We are particularly interested in operations for which $\tilde{t}_{xx} = \tilde{t}_{yy}^{*}$ and $\tilde{t}_{xy} = \tilde{t}_{yx}^{*}$, meaning that Eq.3.7 remains invariant under the simultaneous $\boldsymbol{P} = \boldsymbol{\sigma_x}$ and $\boldsymbol{T} = *$ transformations, i.e. $\boldsymbol{PTJ} \equiv \boldsymbol{JPT}$, where $\boldsymbol{\sigma_x}$ is a Pauli matrix and $*$ represents complex conjugation. As we are only considering systems constructed from linear materials, meaning that the electromagnetic fields have harmonic time dependence, $\boldsymbol{T}$ like for quantum states and optical waveguide modes can be thought of as a time reversal operator. On the other hand, while $\boldsymbol{P}$ will be

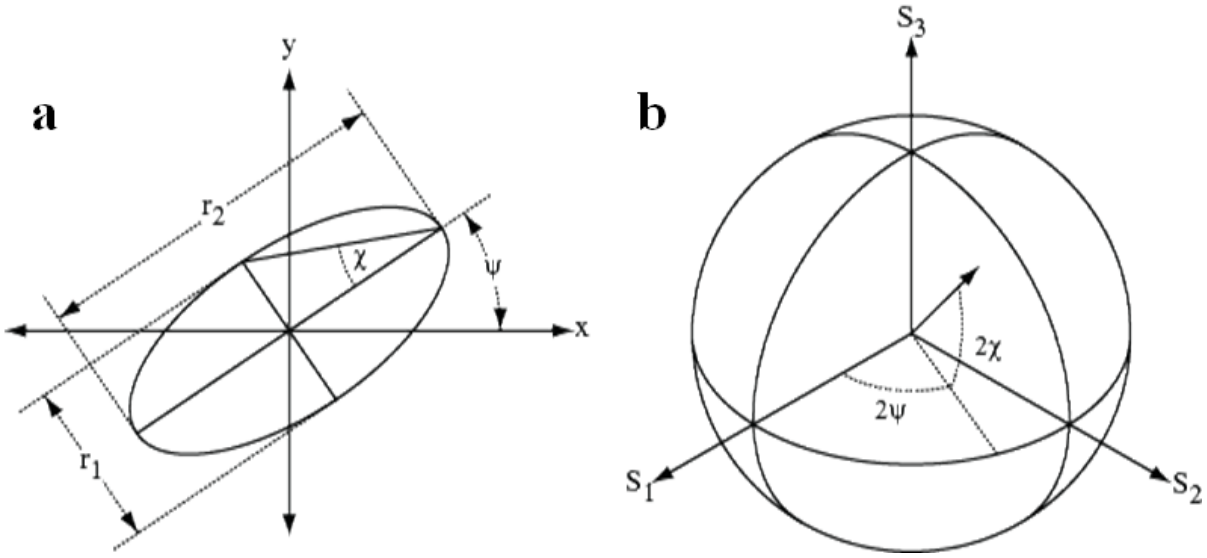

Figure 3.5: Representation of generalised polarisation ellipses. a) Ellipse plotted in Cartesian coordinates showing the geometrical significance of $\boldsymbol{\psi}$ and $\boldsymbol{\chi}$. b) The Poincare sphere used for graphically representing photonic polarisation states, linearly polarisation lies on the equatorial circle $\boldsymbol{\chi = 0}$ and circular polarisations $\boldsymbol{\chi = \pm \pi/2}$ lie at the north and south poles[*85*].

referred to as parity, rather than the usual three dimensional operation $(x, y, z) \rightarrow (-x, -y, -z)$ for a vector field, here $\boldsymbol{P}$ is a one dimensional reflection about the plane $x = y$. Also, even though this condition is mathematically identical to that discussed in the context of Eq.3.2, physically $\boldsymbol{P}$ here has a very different meaning. Instead of representing a discretised version of the traditional one-dimensional parity operation $\boldsymbol{E}(\boldsymbol{r}) \rightarrow \boldsymbol{E}(-\boldsymbol{r})$, when

acting on Jones matrices $\boldsymbol{P}$ is a local but anisotropic field transformation, e.g. $E_x(\boldsymbol{r}) \rightarrow E_y(\boldsymbol{r})$. By varying the ratio $Im(\tilde{t}_{xx})/|\tilde{t}_{xy}|$, the eigen-transmission coefficients

$$\tilde{t} = Re(\tilde{t}_{xx}) \pm \sqrt{|\tilde{t}_{xy}|^2 - Im(\tilde{t}_{xx})^2}, \qquad [3.8]$$

can be seen to undergo a transition from real valued $\tilde{t}$ for $|\tilde{t}_{xy}| > |Im(\tilde{t}_{xx})|$ to complex $\tilde{t}$ for $|\tilde{t}_{xy}| < |Im(\tilde{t}_{xx})|$. At the same time, the corresponding polarisation eigenvectors change suddenly from

$$\frac{\tilde{E}_y}{\tilde{E}_x} = \pm e^{-iarg(\tilde{t}_{xy})} e^{\pm i\, sin^{-1}\left(\frac{|Im(\tilde{t}_{xx})|}{|\tilde{t}_{xy}|}\right)} \qquad [3.9]$$

for $\left(|\tilde{t}_{xy}| > |Im(\tilde{t}_{xx})|\right)$, to

$$\frac{\tilde{E}_y}{\tilde{E}_x} = ie^{-iarg(\tilde{t}_{xy})} e^{\mp\, cosh^{-1}\left(\frac{|Im(\tilde{t}_{xx})|}{|\tilde{t}_{xy}|}\right)} \qquad [3.10]$$

for $\left(|\tilde{t}_{xy}| < |Im(\tilde{t}_{xx})|\right)$. Unlike for the waveguide systems investigated in [*70*, *71*], the

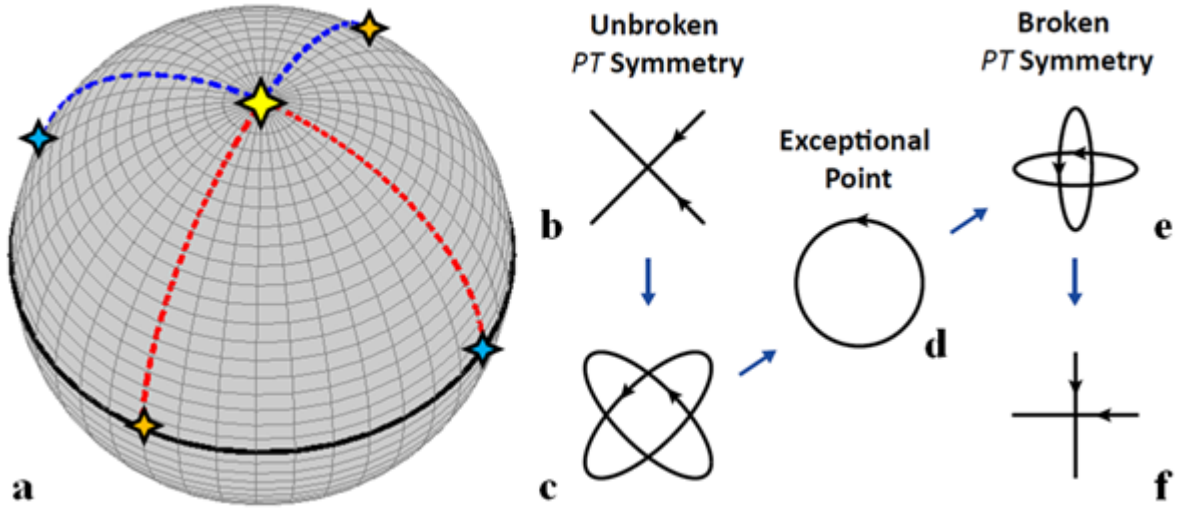

Figure 3.6: *PT* symmetry breaking in polarisation space. a) Eigen polarisation states of *PT* symmetric Jones matrix for real-valued $\tilde{\boldsymbol{t}}_{\boldsymbol{xy}} = \boldsymbol{0} \rightarrow \infty$ plotted on the Poincare sphere. b, c) Polarisation ellipses for unbroken *PT* symmetry, i.e. Eq.3.9, with 'b' also corresponding to coordinates marked by orange stars in 'a'. d) Single left handed circularly polarised eigenstate for $\tilde{\boldsymbol{t}}_{\boldsymbol{xy}} = |\boldsymbol{Im}(\tilde{\boldsymbol{t}}_{\boldsymbol{xx}})|$, also marked by yellow star in 'a'. e, f) Polarisation ellipses for broken *PT* symmetry, i.e. Eq.3.10, with 'f' also corresponding to coordinates marked by blue stars in 'a'.

specific details of these modes, as well as their overlap, are important. As illustrated in Figure 3.6, for real-valued $\tilde{t}_{xy}$ Eq.3.9 describes a pair of ellipses with major axes oriented along $\pm 45^{\circ}$ with respect to $\hat{x}$. Eq.3.10 on the other hand corresponds to elliptical fields with $\hat{x}$ and $\hat{y}$ oriented major axes. In this case, *PT* symmetry is said to be broken as the eigenstates of $\boldsymbol{J}$ are no longer eigenstates of the $\boldsymbol{PT}$ operator but are instead exchanged when it acts upon them. From Figure 3.6a we can also see that, for fixed $sgn\left(|Im(\tilde{t}_{xx})|/\tilde{t}_{xy}\right)$, the eigen-polarisation coordinates all lie on the same Poincare hemisphere, indicating that they all share the same sense of rotation. This non-orthogonality, which is a clear manifestation of non-Hermiticity, becomes most extreme at the EP where only LCP light can pass through the system without being partially converted to its orthogonal state, namely RCP. Interestingly, throughout this parametric variation only the ellipticities, i.e. the elevation angles on the Poincare sphere, are tuned continuously. The orientation angles remain fixed except for a sharp 45° twist that occurs when passing through the EP. What's more, although Eq.3.7, which is written in the Cartesian basis, formed the starting point of our analysis, polarisation states can be expressed as the relative complex amplitude of any two antipodal coordinates on the Poincare sphere. As the mathematical form of Eqs.3.8-3.10 is independent of the chosen basis, it should therefore be possible to observe phase transitions in which ψ, χ or even both ψ and χ jump suddenly in response to the variation of some parameter.

Up until this point, we have simply discussed the properties of an abstract *PT* symmetric Jones matrix. The next question is how can we physically realise such a system? Firstly, a significant departure of this particular problem from conventional non-Hermitian dynamics is that the imaginary part of the transmission coefficient corresponds to phase retardation of a wave rather than dissipation. Hence, even the description of a lossless birefringent medium requires the use of a complex Jones matrix. However, relying on an accumulated phase difference between orthogonal waves to achieve a carefully balanced

output means that the behaviour will be highly sensitive to the relationship between the device thickness and the wavelength, leading to strong dispersion. Here we wish to explore *PT* symmetry within media with locally well-defined polarisation eigenstates. In this case, the material properties themselves, i.e. the polarisability tensor, must be non-Hermitian and the presence of dissipation is again necessary. As explained in (2.3), metamaterials represent the ideal platform for realising a tailored electromagnetic response, especially when we seek precise, rather than simply large, values. In actual fact, because we only care about changes to the field directions and not the propagation characteristics of the transmitted light, metasurfaces which consist of a single monolayer of artificial structures will be employed, simplifying the sample fabrication significantly.

To begin, we consider an idealised metasurface consisting of a two dimensionally periodic, square array of "meta-molecules" with lattice constant d. Each molecule is made from a pair of "meta-atoms" in the form of electric dipole antennas which oscillate in plane

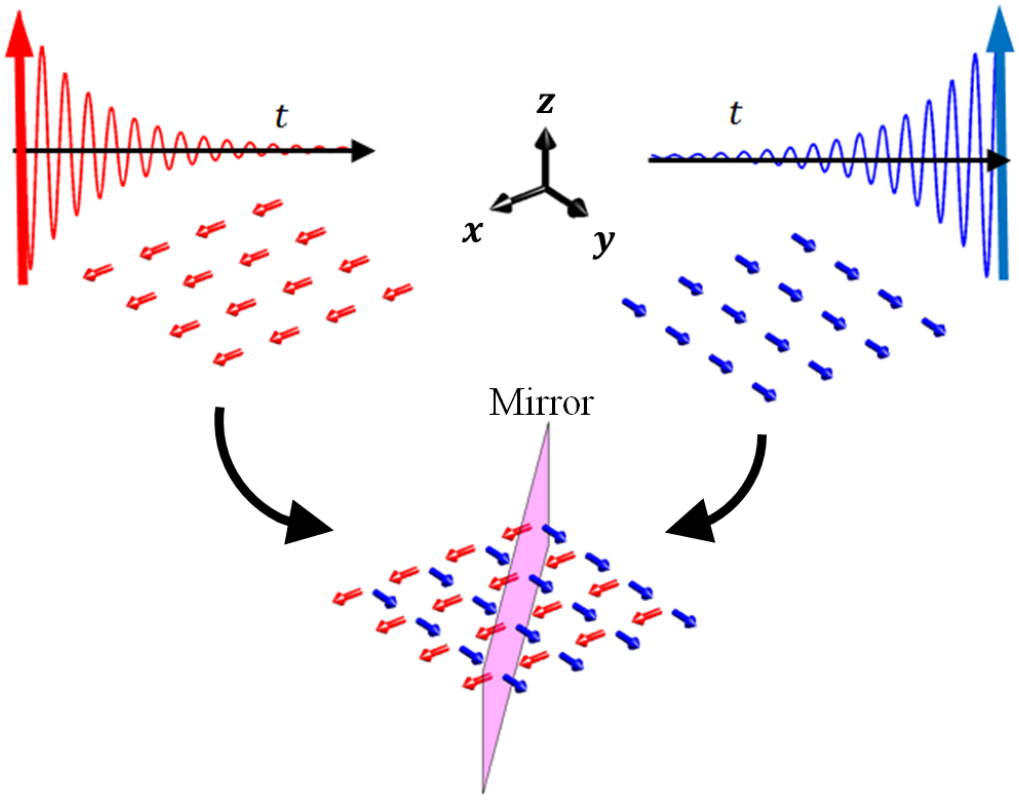

Figure 3.7: Coupled array of oscillating electric dipole moments with red and blue dipoles experiencing loss and gain, respectively.

and are oriented perpendicular to one another $\hat{p}_{x,y} = \tilde{p}_{x,y}(\omega)e^{i\omega t}$, as illustrated in Figure 3.7. The interaction between an individual dipole moment and a local monochromatic electric field $\widehat{\boldsymbol{E}}_{\boldsymbol{loc}} = \left(\tilde{E}_{lx}, \tilde{E}_{ly}\right)e^{i\omega t}$ can then be described by a Lorentzian resonance model

$$\left(\omega_{x,y}^2 - \omega^2 + i2\omega\gamma_{x,y}\right)\tilde{p}_{x,y} = \omega_{x,y}g_{x,y}\tilde{E}_{lx,ly}. \quad [3.11]$$

Crucially, if d is smaller than the wavelengths of propagating solutions in the surrounding media, diffraction is prohibited and the metasurface will only reflect or transmit an incident plane wave. However, this doesn't mean that the scattered wave can be found by simply replacing $\widehat{\boldsymbol{E}}_{\boldsymbol{loc}}$ by the incident radiation field $\widehat{\boldsymbol{E}}_{\boldsymbol{inc}}$, as the mutual dipole coupling still can't be ignored. Instead, $\widehat{\boldsymbol{E}}_{\boldsymbol{loc}}$ at the location of a given antenna should be written as

$$\begin{pmatrix}\tilde{E}_{lx}\\ \tilde{E}_{ly}\end{pmatrix} = \widehat{\boldsymbol{E}}_{\boldsymbol{inc}} + \begin{pmatrix}G_{xx} & G_{xy}\\ G_{yx} & G_{yy}\end{pmatrix}\begin{pmatrix}\tilde{p}_x\\ \tilde{p}_y\end{pmatrix}, \quad [3.12]$$

where G_{ij} represents a summation of i oriented fields produced by all other j oriented antennas and $G_{xy} = G_{yx}$ as we consider only reciprocal constitutive materials. By working close to resonance $\left(\delta_{x,y} = \omega - \omega_{x,y} \ll \omega_{x,y}\right)$ and in the weak damping limit $\left(\gamma_{x,y} \ll \omega_{x,y}\right)$, the induced response of the metasurface to incoming light can then be expressed by

$$\begin{pmatrix}\delta_x + i\gamma_x + G_{xx} & G_{xy}\\ G_{xy} & \delta_y + i\gamma_y + G_{yy}\end{pmatrix}\begin{pmatrix}\tilde{p}_x\\ \tilde{p}_y\end{pmatrix} = \begin{pmatrix}g_x\tilde{E}_{inc,x}\\ g_y\tilde{E}_{inc,y}\end{pmatrix}. \quad [3.13]$$

If we restrict our discussion for the time being to normal incidence $k_x = k_y = 0$, the corresponding Jones matrix for transmission is simply given by the superposition of the incident field $\widehat{\boldsymbol{E}}_{\boldsymbol{inc}}$ and the field scattered by the dipole array in the forward direction $\frac{i\omega\eta_0}{2d^2}\left(g_x\tilde{p}_x, g_y\tilde{p}_y\right)$: `

$$\begin{pmatrix}\tilde{E}_{tx}\\ \tilde{E}_{ty}\end{pmatrix} = \left[\overleftrightarrow{I} + A\begin{pmatrix}g_x^2\left(\delta_y + i\gamma_y + G_{yy}\right) & -g_xg_yG_{xy}\\ -g_xg_yG_{xy} & g_y^2(\delta_x + i\gamma_x + G_{xx})\end{pmatrix}\right]\begin{pmatrix}\tilde{E}_{ix}\\ \tilde{E}_{iy}\end{pmatrix}, \quad [3.14]$$

where

$$A = \frac{i\omega\eta_0}{2d^2((\delta_x + i\gamma_x + G_{xx})(\delta_y + i\gamma_y + G_{yy}) - G_{xy}^2)}. \quad [3.15]$$

Clearly any changes to the state of polarisation must be governed by the matrix in the second term of Eq.3.14, while the multiplicative factor A and the additional identity matrix can only influence spectral variations. As explained previously, we wish to explore the requirements for such a matrix to be *PT* symmetric. First however we can make some simplifying observations. Because the summation terms G_{ij} depend purely on the lattice geometry, the use of a square unit cell fixes $G_{xx} = G_{yy}$. What's more, as the x and y oriented dipoles radiate into orthogonally polarised channels, they can only interact via their quasi-static electric near fields and so G_{xy} must simply be a constant real number. Consequently, the symmetry of the Jones matrix is wholly determined by the local quantities $\delta_{x,y}, \gamma_{x,y}$ and $g_{x,y}$. In particular, we can see that the condition for a metasurface to be non-Hermitian but *PT* symmetric becomes $g_x = g_y$, $\delta_x = \delta_y$, $\gamma_x \neq \gamma_y$and $\gamma_x + \gamma_y = -2Im(G_{xx})$. As $0 < Im(G_{xx})$, to satisfy the last relationship one of the two sets of antennas must amplify the incident E-field. Here, for experimental convenience we will deal only with passive systems $\gamma_y > \gamma_x > 0$. Nevertheless, similarly to previous works[*70*, *73*], Eq.3.14 can be separated into a lossy isotropic part and an anisotropic *PT* part

$$\begin{pmatrix} \tilde{E}_{tx} \\ \tilde{E}_{ty} \end{pmatrix} = [1 + g_x^2 AS]\vec{I}\begin{pmatrix} \tilde{E}_{ix} \\ \tilde{E}_{iy} \end{pmatrix} - g_x^2 A \begin{pmatrix} -i\Gamma & G_{xy} \\ G_{xy} & i\Gamma \end{pmatrix}\begin{pmatrix} \tilde{E}_{ix} \\ \tilde{E}_{iy} \end{pmatrix}, \quad [3.16]$$

where $S = \delta_x + G_{xx} + i(\gamma_y + \gamma_x)/2$ and $\Gamma = (\gamma_y - \gamma_x)/2$. Although the physical system being considered is a coupled set of lossy resonators, Eq.3.16 could equally well describe an oscillator model with balanced loss and gain (2nd term on right-hand side of Eq.3.16) embedded in an absorptive background medium (1st term on right-hand side of Eq.3.16). As per the analysis summarised in Figure 3.6, variation of Γ/G_{xy} brings about a phase transition

in the polarisation eigenstates. Originating from the inherent dispersion of the component antennas, the corresponding transmission eigen-spectra

$$\tilde{t}_{eig}(\omega) = 1 + \frac{i\omega\eta_0 g_x^2\left(S \pm \sqrt{G_{xy}^2 - \Gamma^2}\right)}{2d^2((\delta_x + i\gamma_x + G_{xx})\left(\delta_x + i\gamma_y + G_{xx}\right) - G_{xy}^2)} \quad [3.17]$$

take the form of two separate resonant features with different natural frequencies for $\Gamma < G_{xy}$ but different linewidths for $\Gamma > G_{xy}$. As these are purely hybridised modes, not relying on any interference effects, the two expressions in Eq.3.17 represent curves with a simple Lorentzian shape. This spectral signature indicates that the coupled antennas are responding as two physically independent, but highly overlapping, sets of elliptical dipoles. On the other hand, conventional systems, such as the bilayer chiral geometries discussed in (2.3.4), have modes which are approximately orthogonal.

Having derived the conditions that need to be met for a collection of dipole emitters to exhibit *PT* symmetric behaviour, we now proceed to the design of a realistic *PT* metasurface. Many possible forms exist but our chosen meta-atom for this purpose is the SRR, for reasons that will be made clear later on. As discussed in (2.3.3), the LC resonance ω_0 of such a structure can be controlled by tailoring its specific size and shape. Although this fundamental mode possesses two radiative outlets, one of magnetic and one of electric origin, when working at normal incidence each ring can be considered as a single electric dipole moment centred approximately on the gap in that ring. The radiative coupling strength g depends, therefore, on the specific geometry of this gap. It is clear then that the most straightforward way, or indeed the only practical way, of creating an anisotropic *PT* metasurface is to use structurally identical antennas for both x and y oriented arrays. This just leaves the question of how to independently engineer the dissipation of the resonators. The parameter γ, used above, describes the rate at which the total energy contained within an oscillator decays in time. Two mechanisms, radiation and absorption contribute to this decay. In most other

metamaterial investigations seeking to exploit or manipulate dissipation, attention is commonly directed towards the former mechanism while Ohmic or material loss is considered a limiting factor. On the contrary, for the present study absorption provides the only available method for satisfying $\gamma_x \neq \gamma_y$and $g_x = g_y$ simultaneously. Specifically, we can construct the same SRR design out of two metals with different imaginary parts of their permittivities. A complication for this approach is that material variations can also affect the resonant frequency. This is especially true at optical frequencies as plasmonic modes are highly sensitive to changes in the real part of the dielectric function. Fortunately, the characteristic length scale of THz resonators is much larger than the skin depth of most metals because of their huge dynamic conductivities. Consequently, the electromagnetic boundary condition created at the surface of a SRR, and in turn its natural frequency, vary only very slightly with changes to the permittivity. On the other hand, the field penetrating into the structure is still sufficient to achieve a significant attenuate of the oscillation.

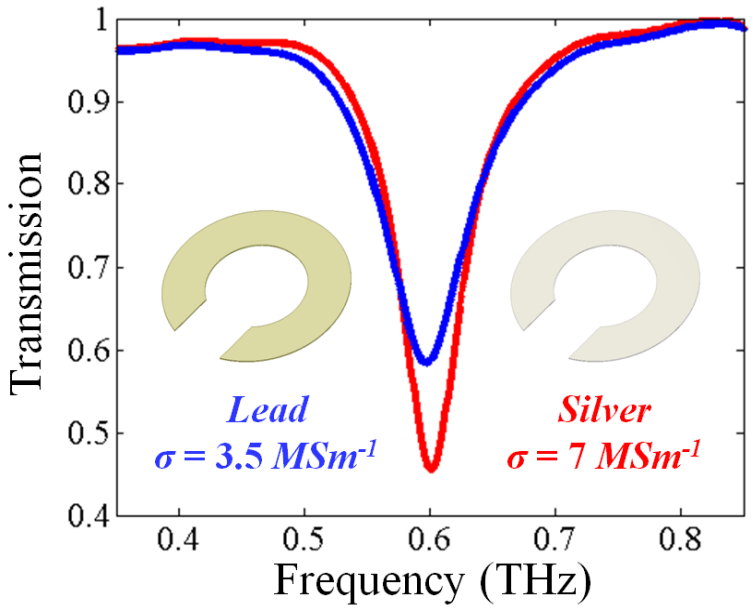

Figure 3.8: FDTD simulations of the transmitted amplitude through Lead (blue) and Silver (red) SRR arrays. The larger penetration depth of Lead compared to Silver leads to a pronounced broadening of the linewidth compared to the very subtle frequency shift.

Figure 3.8 shows the simulated transmission spectra for a set of Lead and Silver rings, described via the Drude model with DC conductivities $\sigma = 3.5MSm^{-1}$ and $\sigma = 7MSm^{-1}$, respectively. It is clear to see that the different material properties give rise to distinct linewidths whilst maintaining very similar mode frequencies.

By employing different metals we can easily satisfy the conditions for *PT* symmetry. To observe a phase transition, next we seek to tune the coupling parameter G_{xy}.When interlacing two orthogonally oriented SRR arrays, the energy transferred from one array to the other is determined by the overlap between the isolated resonant near field patterns. As already discussed, the electric response resembles a periodic dipolar function of the in plane coordinates. Unlike for the radiation emitted to the far field, magnetic induction plays an

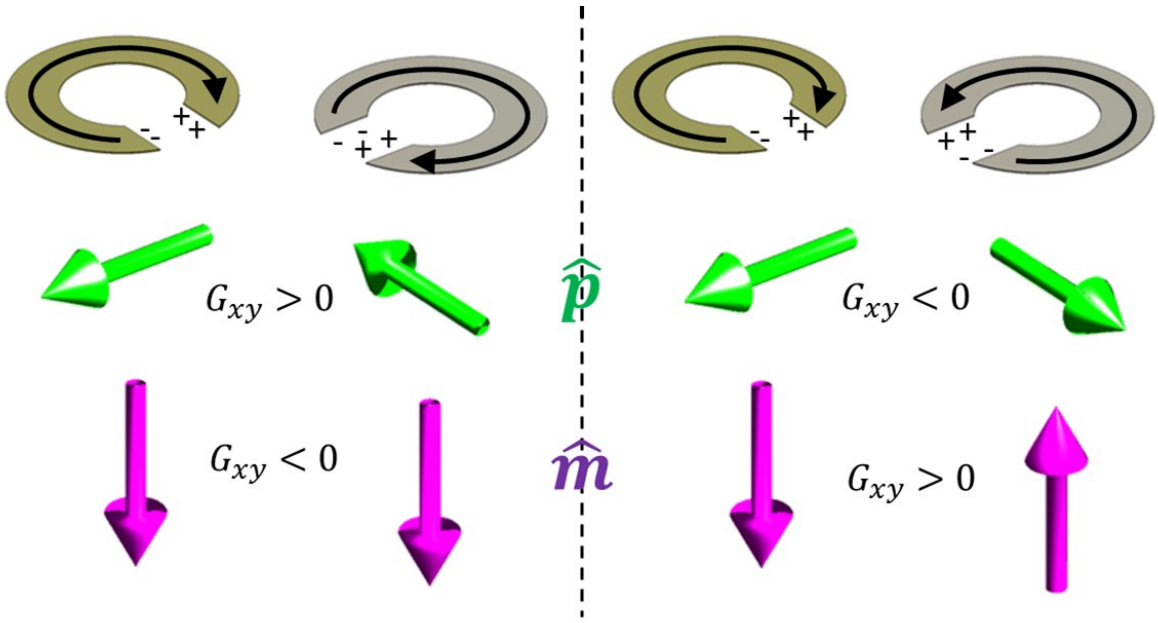

Figure 3.9: Dipole coupling between orthogonally oriented SRRs. a) Symmetric current distribution represents antisymmetric (symmetric) electric (magnetic) dipole configuration providing positive (negative) contribution to the coupling coefficient. b) Antisymmetric current distribution represents antisymmetric (symmetric) magnetic (electric) dipole configuration providing positive (negative) contribution to the coupling coefficient.

important role in the inter-ring coupling strength. Interestingly, from Figure 3.9 we can see that when orthogonally arranged the capacitive and inductive SRR interactions have opposite signs. Thus, depending on the chosen configuration the two mechanisms could potentially

cancel providing access to the weak coupling limit. Another important feature of these particular antennas is that the electric field is highly localised in the gaps. Therefore, by using a relatively larger ring structure the resonant wavelength can be made to be much bigger than the gaps while still being smaller than the array period, meaning that strong nearest neighbour coupling should take place with minimal lattice suppression.

To numerically confirm our analytical predictions, simulations of normally incident plane wave transmission through metasurfaces composed of meta-molecules with different relative SRR positions, have been carried out. By calculating for both x and y polarised incident excitations, the four complex Cartesian spectra $\tilde{t}_{xx}$, $\tilde{t}_{yy}$, $\tilde{t}_{yx}$ and $\tilde{t}_{xy}$ can be found. Subsequently, the 2×2 transmission Jones matrix comprising these four complex coefficients can be diagonalised at each frequency. The resulting polarisation eigen-states and corresponding transmission spectra are shown in Figure 3.10. As expected from the analysis above, when nearest neighbour SRRs are placed in close proximity with their gaps facing one another strong electric dipole coupling leads to pronounced resonant frequency splitting, Figure 3.10b. The associated polarisation states are almost linear and oriented along $y = \pm x$, Figure 3.10g. In this configuration the difference in material loss is therefore seen to have very little effect. When the rings are moved further apart, eventually, inductive coupling takes over, flipping the handedness of both modes, as evidenced by the single data point occupying the southern hemisphere in Figure 3.10a. The electric and magnetic interactions are therefore guaranteed to cancel out at a particular distance, $\sim 19\mu m$ in Figure 3.10f/k, leaving practically independent x and y polarised responses with spectral features very similar to the isolated case shown in Figure 3.8. Consequently, the arrangement we have chosen makes the full range of values for G_{xy}/Γ accessible. Between the two extremes $G_{xy}/\Gamma = 0$ and $G_{xy}/\Gamma \gg 1$ the

simulated metasurface response, shown in Figure 3.10a, follows the *PT* dipole

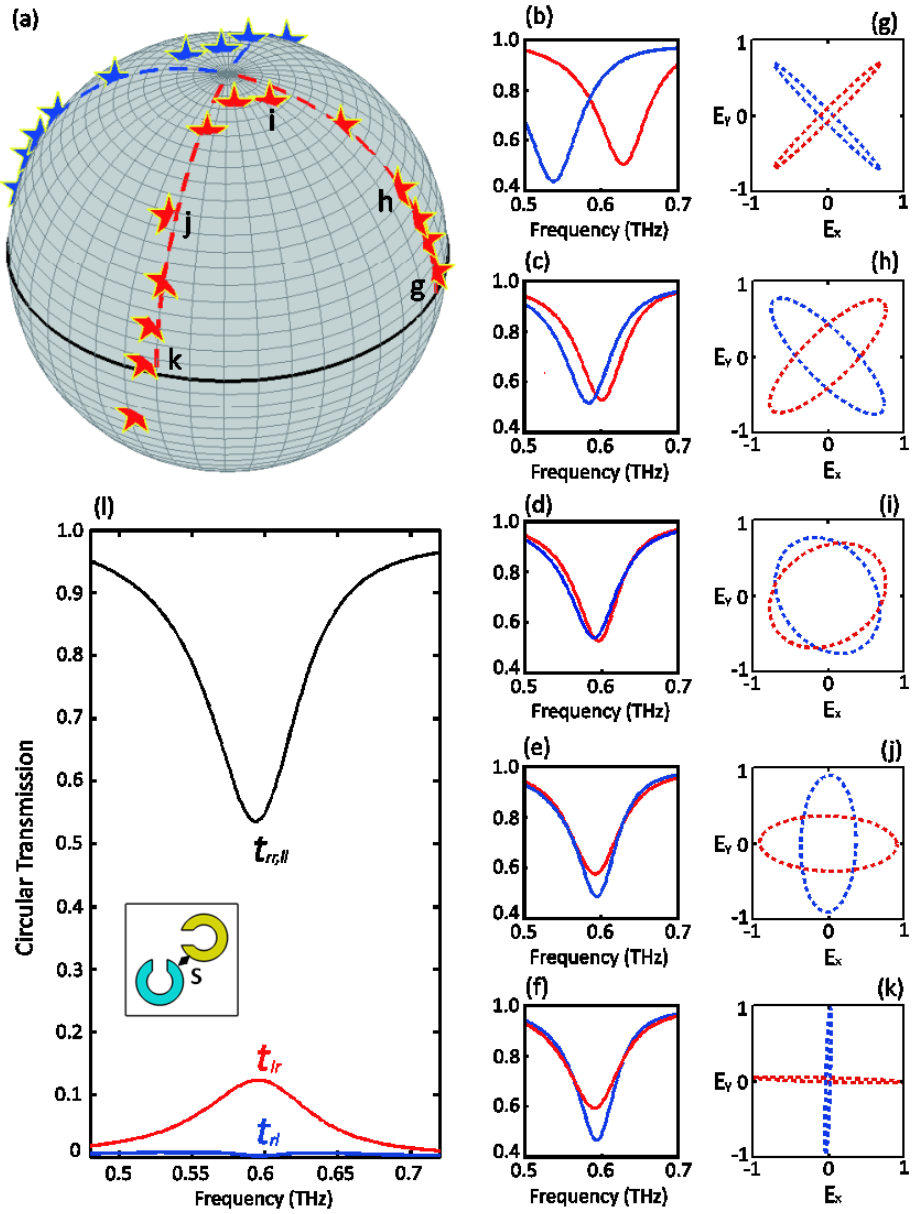

Figure 3.10: Full-wave simulation results for a *PT* symmetric metasurface, the unit cell of which appears in the inset of subplot (l) (detailed dimensions are given in Figure 3.11a), with variable coupling strength, controlled by changing the distance between more and less lossy SRRs, denoted by '**S**' in the inset of (l),between 2 and 20µm. a) Polarisation eigenstates for different SRR separations plotted on the Poincare sphere with LCP at the northpole, the dashed lines represent the eigenstates of an ideal *PT* symmetric dipole model with varying coupling coefficients and the single star occupying the southern hemisphere represents a change of sign of the coupling coefficient caused by the domination of the inductive coupling at large ring separation. b-f) show sampled transmission spectra for the eigenpolarisation states g-k) which correspond to points labelled in (a), ring separation in µm = 2 (b, g), 12 (c, h), 14.5 (d, i), 16 (e, j), 19 (f, k). l) Circular transmission spectra for SRR configuration closest to the EP (d, i). Figure and caption from [*69*].

model very closely, with a sudden 45° rotation of the polarisation eigenstates, caused by *PT* symmetry breaking, clearly visible at $\sim 14.5\mu m$. A slight deviation from the ideal transition does occur, however, at the EP. Rather than coalescing exactly, it can be seen that the eigenmodes always have a finite difference in their ellipticities. The origin of this avoided crossing will be discussed later on. Nevertheless, in the configuration closest to the EP, the circularly polarised transmission spectra, shown in Figure 3.10l, exhibit asymmetric conversion efficiencies $|\tilde{t}_{rl}| \neq |\tilde{t}_{lr}|$ with $|\tilde{t}_{rl}| \approx 0$ across the entire resonance feature. This is indicative of the system behaving to a good approximation as an array of left handed circularly polarised dipole moments.

As well as confirming our analytical model, the numerical results also reveal the relationship between physical changes to the metastructure and the transition that occurs for the Jones matrix. Interestingly, the subtle variation of a single geometric feature is seen to be responsible for the drastic alteration to the polarisation response. This is unusual for such a well ordered metamaterial system, where the eigenstates associated with simple Lorentzian resonances normally depend on the effect of global symmetry operations, such as rotation and inversion[*31*]. Figure 3.10 also provides an insight into the role played by loss in asymmetric transmission. In [*86*] it was shown that, for a 2D structure, circularly polarised asymmetric transmission correlated directly with an increase in the anisotropy of loss. Here, on the other hand, a balance between loss and coupling $G_{xy} = \Gamma$ optimises this particular effect. Therefore, decreasing G_{xy} away from the EP, or increasing Γ by the duality between G_{xy} and Γ in Eq.3.16, will actually reduce the ellipticity of the eigenmodes, thereby diminishing the asymmetry of the circular conversion efficiency.

To experimentally demonstrate *PT* symmetry breaking in polarisation space, a number of different samples have been fabricated based on the SRR design simulated in

Figure 3.10. By carrying out two successive photolithographic processes, a set of lossy rings made of lead could be created on the same silicon substrate as a set of less lossy silver rings.

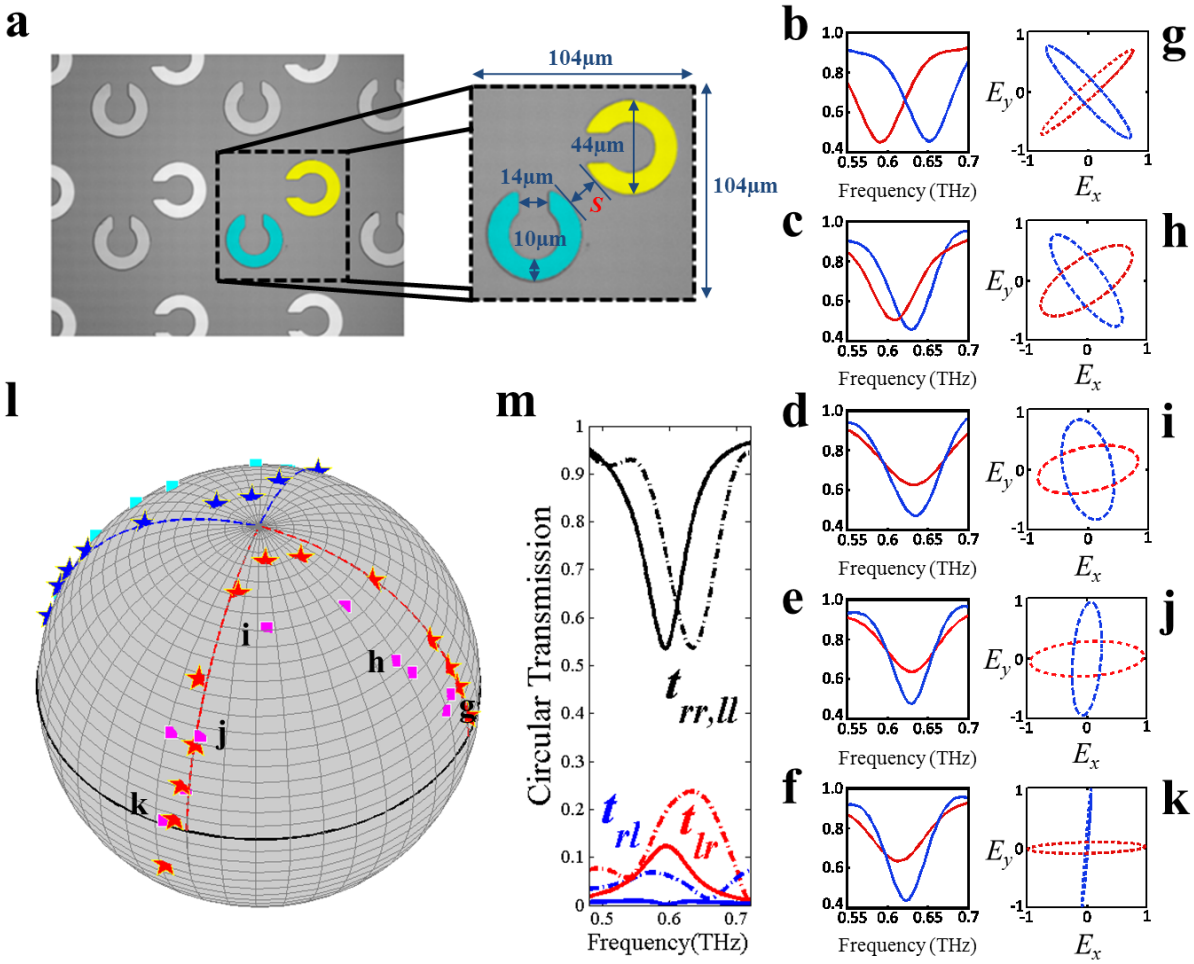

Figure 3.11: THz-TDS measurements for a PT symmetric metasurface with variable coupling strength, controlled by changing the distance between Lead and Silver SRRs, labelled by *S* in (a), between 2 and 20µm. a) Photograph of PT symmetric metasurface composed of 300nm thick silver (yellow) and lead (turquoise) SRRs on Silicon substrate. b-f) Sampled transmission spectra for the eigenpolarisation states (g-k) which correspond to points labelled in (l), nominal ring separation *S* in µm = 2 (b, g), 10 (c, h), 11.5 (d, i), 16 (e, j), 20 (f, k). l) Polarisation eigenstates for different *S* plotted on the Poincare sphere, the dashed lines represent the eigenstates of an ideal PT symmetric dipole model, red and blue stars represent simulated data and turquoise and purple squares represent measured data**.** m) Circular transmission spectra for SRR configuration closest to the EP, measured and simulated results represented by dashed (d, i) and solid lines, respectively. Figure and caption modified from [*69*].

This procedure also allowed the relative positioning of the two sets to be varied from sample to sample, providing a range of configurations with different coupling strengths. A photographic image of an example metasurface is shown in Figure 3.11a. After measuring the

four frequency dependant elements of the Jones transmission matrices using THz-TDS, the eigenstates of each structure could be analysed. In Figure 3.11b-k, a clear transition from resonant splitting to relative broadening is observed, accompanied by a definite 45^o rotation of the corresponding polarisation states, i.e. a 90^o azimuthal rotation on the Poincare sphere. Good correspondence between the trend of the experimental data and our theoretical results can also be seen in Figure 3.11l. The slight scattering of the points plotted on the Poincare sphere can be attributed to measurement errors. The difficultly in orienting each sample in precisely the same direction with respect to the polarisers limits the accuracy with which the azimuthal coordinates can be determined. Similar errors are responsible for the fact that the ellipticities of the two eigenstates associated with a particular metasurface are not exactly the same and that their azimuthal angles do not differ by precisely 90^o. These conditions should always hold for normally incident illumination of a 2D structure. A more serious issue, however, is the avoided crossing that occurs close to the *EP*, which is larger than for the simulated data and too significant to be explained by uncertainties in the measurements.

To explore the reasons behind the deviations from ideal *PT* symmetry observed above, both theoretically and experimentally, the various parameters that control the polarisabilities for each system need to be interrogated. While Eqs.3.14 and 3.15 describe the transmission through our metasurfaces, they also contain the quantity G_{xx} which is a slowly converging sum over the entire lattice. We have already explained how this summation plays no part in the *PT* symmetric transition. Therefore, a retrieval method, which has proven effective for SRR arrays which are very similar to the design explored here, will be employed[*87*]. By applying the Fresnel equations to a homogeneous, dielectric slab of thickness t between a substrate with refractive index n_s and a vacuum, the transmission through an ultrathin $t \ll \lambda$ set of electric dipoles antennas can be written approximately in terms of the individual antenna polarizabilites $\tilde{\alpha}$ as[*87*]

$$\tilde{t}(\omega) \approx \frac{2n_s}{1 + n_s - i\frac{2\pi}{d^2\lambda}\tilde{\alpha}(\omega)}. \qquad [3.18]$$

Typically this expression is only used when the incident *E*-field vector is aligned with linear dipole moments. However, it could equally well describe the response of a metasurface to any incident wave for which the transmitted polarisation remains unchanged, *i.e.* any polarisation eigenstate. After inverting Eq.3.18, a Lorentzian function

$$\tilde{\alpha}(\omega) = A + \frac{g}{\omega - \omega_0 + i\gamma} \qquad [3.19]$$

has been fitted to the simulated and measured eigen transmission spectra with varying SRR separation, shown in Figure 3.12. As expected, the instantaneous bifurcation of the resonant frequencies and linewidths associated with ideal *PT* symmetry breaking has been replaced by a clear but more gradual transition. The properties of the corresponding antennas can then be

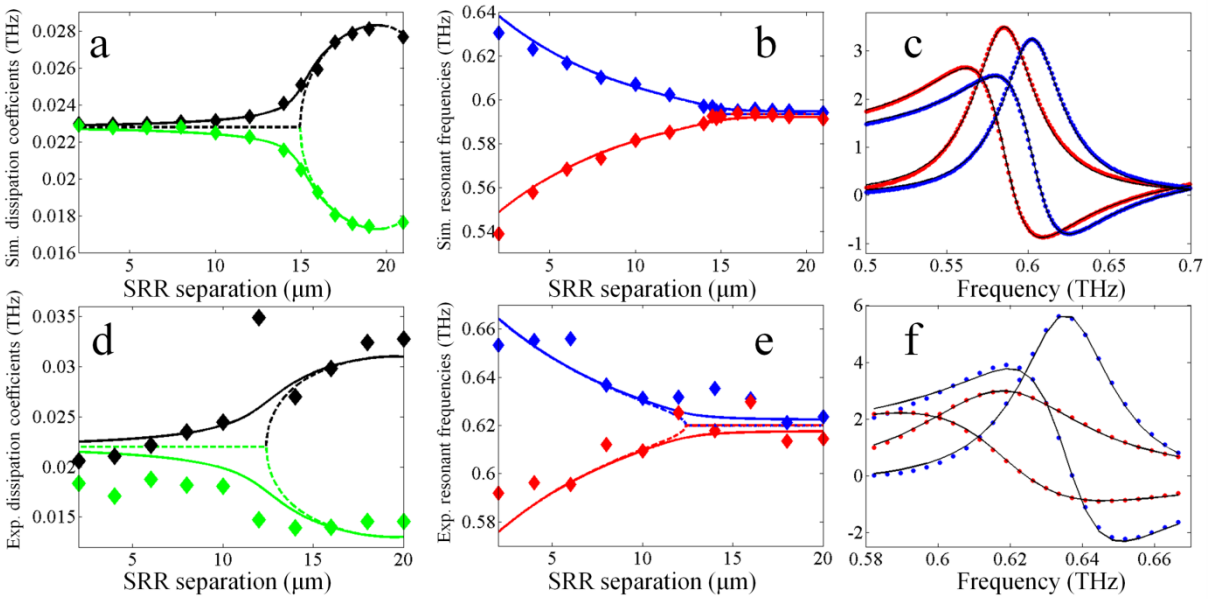

Figure 3.12: Dissipation coefficients (a, d) and resonant frequencies (b, e) in THz associated with the eigenstates of the polarisability matrix, for simulation (a-c) and experiment (d-f). Solid lines represent the eigenvalues of an almost *PT* symmetric matrix constructed from avaraged parameter values from Figure 3.13, with in particular $\boldsymbol{\delta = 0.0023}$ THz (a, b) and $\boldsymbol{\delta = 0.0073}$ THz (d, e). A cubic fit was used to relate $\boldsymbol{G_{xy}}$ to SRR separation. Dashed lines represent the eigenvalues of an ideal PT symmetric matrix with the same parameterisation as the solid lines except for $\boldsymbol{\delta = 0}$. Examples of fitted curves (solid black) alongside data (dotted colour) are shown in c and f for simulated and measured results, respectively.

found by using the eigenstates of the Jones matrices $\boldsymbol{J_t} = \boldsymbol{X} diag(\tilde{t}_1, \tilde{t}_2)\boldsymbol{X^{-1}}$ to transform the polarisabilities back to the Cartesian basis

$$\begin{pmatrix} \tilde{\alpha}_{xx}(\omega) & \tilde{\alpha}_{xy}(\omega) \\ \tilde{\alpha}_{yx}(\omega) & \tilde{\alpha}_{yy}(\omega) \end{pmatrix} = \boldsymbol{X} \begin{pmatrix} \tilde{\alpha}_1 & 0 \\ 0 & \tilde{\alpha}_2 \end{pmatrix} \boldsymbol{X^{-1}} \qquad [3.20]$$

and then fitting the functions

$$|\alpha_{xx}(\omega)| = \left| A + \frac{g_x^2(\omega - \omega_y + i\gamma_y)}{(\omega - \omega_x + i\gamma_x)(\omega - \omega_y + i\gamma_y) - G_{xy}^2} \right|$$

$$|\alpha_{yy}(\omega)| = \left| A + \frac{g_y^2(\omega - \omega_x + i\gamma_x)}{(\omega - \omega_x + i\gamma_x)(\omega - \omega_y + i\gamma_y) - G_{xy}^2} \right| \qquad [3.21]$$

$$\alpha_{xy}(\omega) = \frac{g_x^2 g_y^2 G_{xy}}{(\omega - \omega_x + i\gamma_x)(\omega - \omega_y + i\gamma_y) - G_{xy}^2}.$$

From Figure 3.13a the simulated meta-structure is seen to respond to changes in SRR separation as predicted, with the dissipation coefficients remaining constant, $\gamma_x \sim 0.0285$ THz and $\gamma_y \sim 0.0178$ THz, while the coupling strength decreases with increased separation before dropping to zero and changing sign at a critical distance ~19um. As well as the expected properties, a fairly constant resonant frequency shift $\delta \sim 0.0023$ THz is also present which explains the anti-crossing behaviour of the eigenvalues in Figure 3.12. If the diagonal components of the polarisability matrix have different real as well as imaginary parts, the system is not exactly *PT* symmetric. Consequently, the discriminant of the transmission eigenvalues becomes complex and therefore never vanishes for real G_{xy}, which is guaranteed by the periodic nature of the simulations and the orthogonality of the two sets of SRR's. Although the parameters, presented in Figure 3.13b, retrieved from the experimental data appear more scattered, the trend of the results still follows that of Figure 3.13a with relatively fixed values for the dissipation coefficients and a decaying coupling coefficient. There is also a larger resonant frequency shift $\delta \sim 0.0073$ THz compared to simulation.

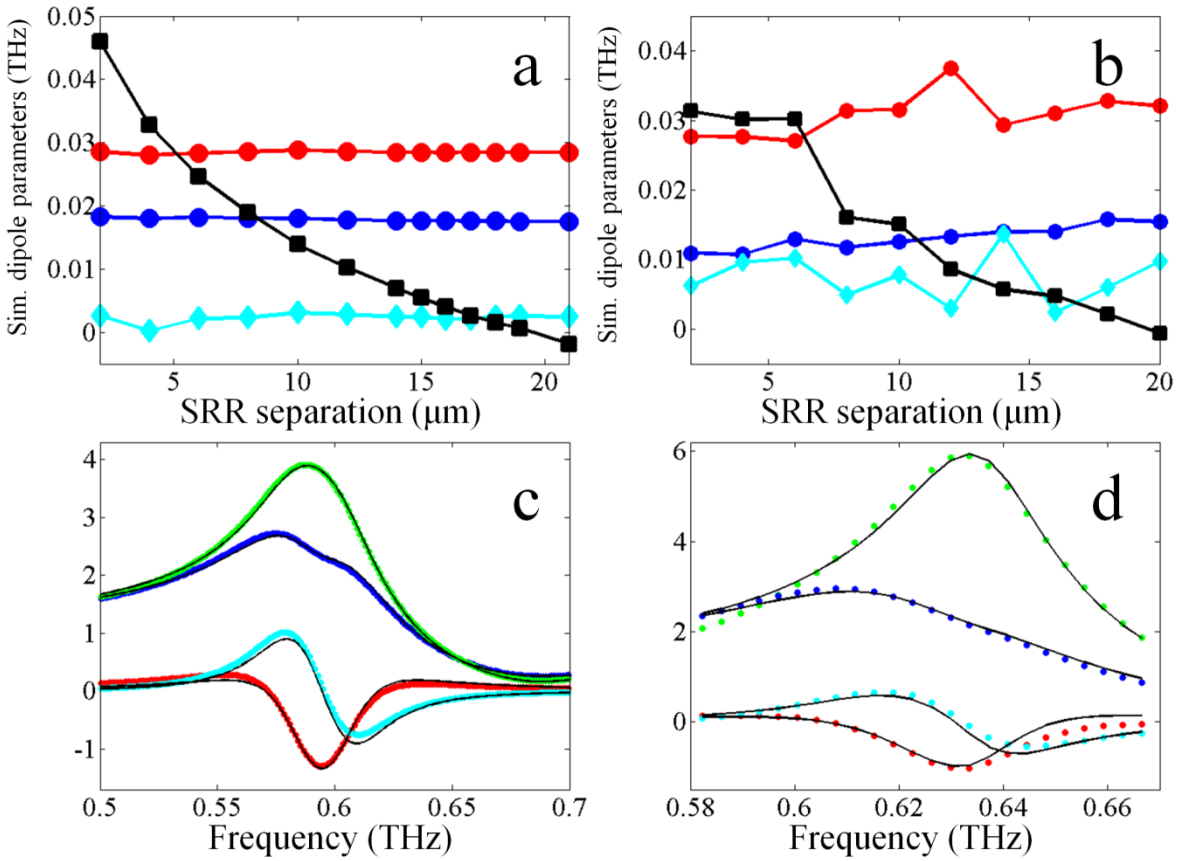

Figure 3.13: Effective parameter retrieval. Fitted values for, $\boldsymbol{\delta = |\omega_x - \omega_y|}$ (cyan diamonds), $\boldsymbol{\gamma_x}$ (red circles), $\boldsymbol{\gamma_y}$ (blue circles) and $\boldsymbol{G_{xy}}$ (black squares) in THz for simulation (a) and experiment (b). Examples of fitted curves (solid black) alongside data (dotted colour) are shown in c and d for simulated and measured results, respectively.

Given the complicated two-step process required to combine SRR's of different metals, we believe that both the scattering of the data and the large δ can be attributed to fabrication error. In Figure 3.12 the eigenvalues of a *PT* symmetric matrix after the inclusion of an appropriate resonant frequency shift match our metasurface polarisability eigenvalues well indicating that δ is indeed the main source of deviation from exact *PT* symmetry found in Figure 3.10 and Figure 3.11.

3.5: Chiral *PT* Symmetric Metamolecules

Having successfully demonstrated that *PT* symmetry breaking can produce a 45^o rotation of the polarisation eigenstates for ultrathin metasurfaces, it is natural to ask whether further dissipation induced transitions can be realised. As previously mentioned, the representation of the relevant parity operator $\boldsymbol{P} = \sigma_x$ is independent of the physical choice of basis states. This means that we can explore different trajectories on the Poincare sphere by coupling together meta-atoms which radiate via elliptically, rather than linearly, polarised light. At normal incidence, planar structures can only emit to the far field by forming electric dipole moments. Unfortunately, rotating electric dipoles are necessarily forbidden unless we break reciprocity and so only the behaviour presented in Figure 3.10 and Figure 3.11 can be observed for 2D metasurfaces. However, as discussed in (2.3.4), coupled, collinear, electric and magnetic dipoles can selectively interact with electromagnetic wave fields rotating in a particular direction. Optical activity and circular dichroism represent special cases of this phenomenon. Again from (2.3.4) we know that resonant structures must be chiral to exhibit the required combination of dipolar sources. With this in mind, the prescription outlined in (3.4) can be adapted to create a new *PT* meta-molecule out of chiral meta-atoms. For example, the coil geometry considered in Figure 2.15, which is the archetypal antenna for achieving such a response, can be employed. Unlike 2D objects for which rotation can mimic inversion, for the two coils to radiate via antipodal points on the Poincare sphere, thus avoiding a radiative anti-Hermitian coupling contribution, they must be enantiomers of one another. An example of such a structure is shown in Figure 3.14. While this design is a perfectly reasonable option, the intricate nature of the 3D shapes involved means that the fabrication of a device working at frequencies outside of the microwave regime will be very difficult if not impossible. Moreover, coming up with a design for achieving a particular

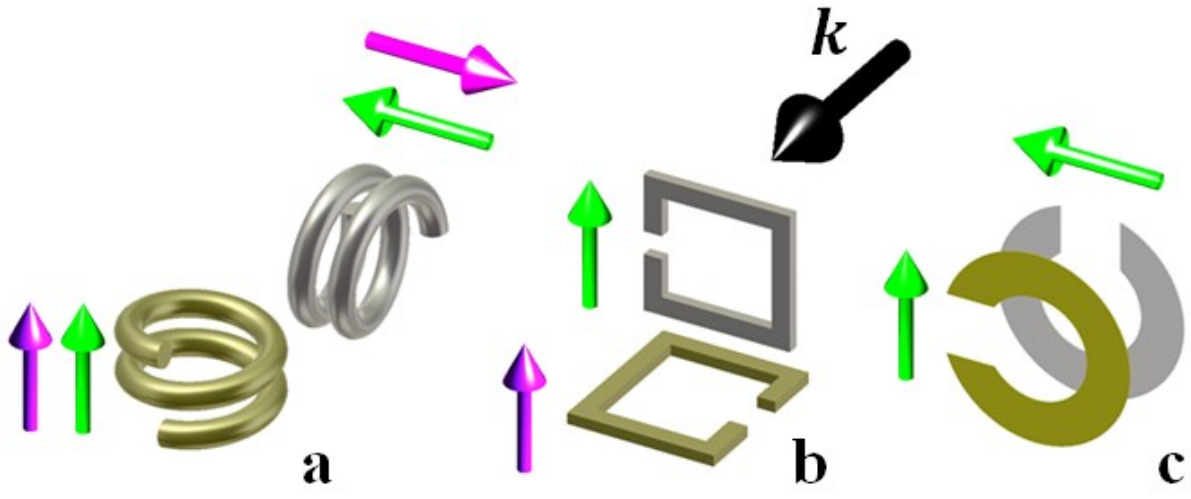

Figure 3.14: *PT* symmetric, chiral meta-molecules. a) Coupling between enantiomer meta-atoms. b) Coupling between non-chiral SRRs, radiating via a magnetic and electric moment. c) Coupled SRRs, both radiating via electric dipole moments, displaced in the propagation direction. Electric (magnetic) dipole moments are represented by green (magenta) arrows.

elliptical polarisation basis is a non-trivial task. Another approach is to persist with simple linearly polarised, and therefore non-chiral, dipole antennas but engineer a complex, Hermitian coupling coefficient between them. From Eqs.3.9/10 a complex $\tilde{t}_{xy}$ can be seen to shift the polarisation eigenstates of the system by the constant elevation angle $\arg(\tilde{t}_{xy})$ on the Poincare sphere at the azimuthal coordinate occupied for unbroken *PT* symmetry. One way of achieving an imaginary $\tilde{t}_{xy}$ is to take a resonator with a radiating magnetic dipole and couple it to a separate resonator with a radiating electric dipole moment. Such a system exhibits the same polarisation phase transition as one composed of coupled chiral objects, each possessing a circularly polarised eigenmode, except that *PT* symmetry broken and unbroken regions are exchanged. While the example illustrated in Figure 3.14b is somewhat simpler than the design shown in Figure 3.14a, this approach suffers from the fundamental asymmetry between sources of electric and magnetic fields. The need to use two very different meta-atom structures means that the corresponding resonant frequencies and radiation efficiencies must be carefully tuned to ensure that they match. This will make the device very sensitive to errors in both the design and fabrication processes. However, one final method remains.

While reciprocity forbids $\arg(\tilde{t}_{xy}) \neq 0$ for orthogonal, collocated electric dipole moments, if the antennas are displaced in the propagation direction the near-field coupling matrix on the left-hand side of Eq.3.13 still applies but the corresponding fields are now emitted from different points in space. This can be described as a local light-matter interaction by relating these two points, separated by a distance *s*, in the radiation field via the dynamic phase accumulated $E(s) = e^{i\frac{2\pi s}{\lambda}}E(0)$. The transmission is then given once again by Eq.3.16 but with $\arg(\tilde{t}_{xy}) = \frac{2\pi s}{\lambda}$. Importantly, this configuration can be realised in a multilayer design, as demonstrated in [*88*], which only requires planar fabrication techniques as were employed in section (3.4).

Figure 3.15 reveals the simulated results for transmission through double layer metasurfaces consisting of orthogonally oriented metal bars. To avoid Fabry-Perot type behaviour which would spoil the simple dipolar response, the structures are completely

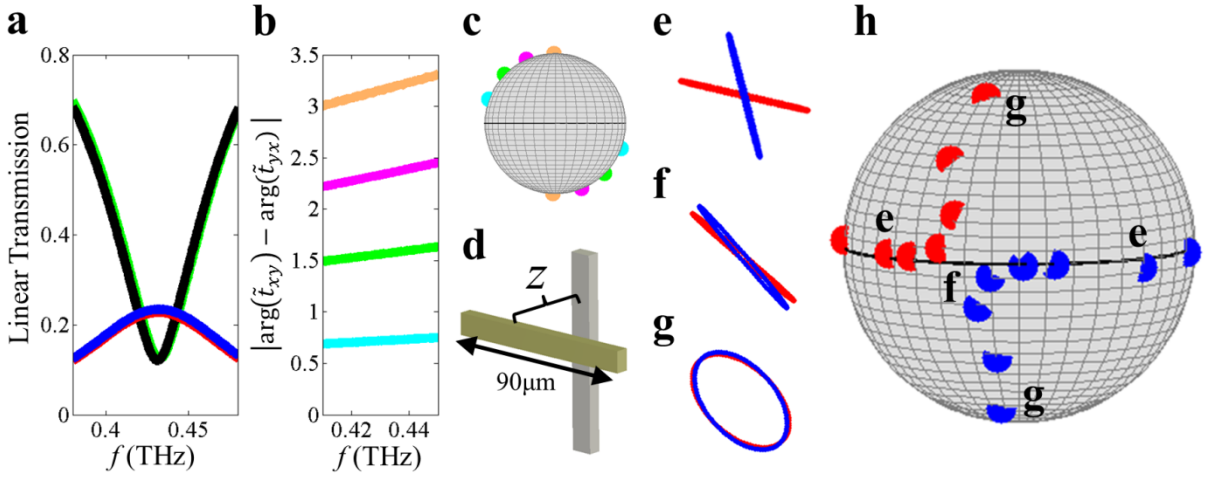

Figure 3.15: Simulated bilayer chiral metamolecule. b) Phase difference between the two linear polarisation conversion coefficients for structure in 'd', but for two silver bars, with z=12μ (cyan), 25μ (green), 37μ (pink) and 50μ (orange). a) Amplitudes of linearly polarised transmission coefficients corresponding to z=25μ (green curve) in 'b', $|\boldsymbol{t_{yx}}|$, $|\boldsymbol{t_{xy}}|$, $|\boldsymbol{t_{xx}}|$ and $|\boldsymbol{t_{yy}}|$ are red, blue, black and green, respectively. c) Polarisation eigenstates corresponding to 'b'. e-g) Eigen polarisation ellipses for coordinates in 'h'. h) By tuning the separation between lead and silver bars in the propagation direction to be a quarter of the free space wavelength at resonance, $\boldsymbol{z \sim 50\mu}$, and varying the in-plane coupling configuration a linearly polarised *EP* is found, seen in 'f', at the transition between linear and elliptical states.

submerged within a slab of silicon. In accordance with the arguments presented above, when using just one metal, varying the separation between the two layers causes a change in $\arg(\tilde{t}_{xy})$, seen in Figure 3.15b, while $|\tilde{t}_{xy}| \approx |\tilde{t}_{yx}|$ is maintained, evident by the almost complete overlap between the red and blue curves in Figure 3.15a. Consequently, the ellipticity of the polarisation eigenstates in the strong coupling limit can be manipulated continuously, shown in Figure 3.15c. When different metals, with different loss, are considered, changes to the relative in plane positioning of the two arrays can be used to control $\mathrm{abs}(\tilde{t}_{xy})$. Indeed Figure 3.15e-h reveals that for a particular layer thickness a transition from linear eigenstates with varying relative orientation to identical ellipses with opposite rotation direction is produced. In this case, a linearly polarised *EP* occurs. This platform therefore makes available all of the possible polarisation phase transitions. Moreover, arbitrarily polarised *EP*s can be realised easily.

To conclude this discussion we note that even though coupling induced transitions have formed the focus of our simulations and experiments up until now, systems with fixed coupling strengths but varying absorption should provide exactly the same response. Recently, a number of different techniques for actively tuning the linewidths of meta-atoms have been demonstrated, exploiting for example, the electrically dependent conductivity of graphene, the photoactive response of silicon or thermally varying phase change materials, such as vanadium dioxide. Taking this approach to *PT* symmetry would enable the development of a new class of polarisation modulation devices. For instance, if the structure explored in Figure 3.15 was modified such that the interlayer phase accumulated by the wave and the loss of one set of SRRs could be tuned dynamically via independent mechanisms, then a single metasurface could generate arbitrary eigen-polarisation pairs.

3.6: Exceptional Points and Polarisation Phase Singularities

The preceding sections have covered the development of a new class of *PT* symmetric metasurfaces which exhibit a host of novel polarising properties as a result of using carefully balanced resonators with differing rates of absorption. In this final part of chapter 3, we seek to explore the wider parameter space within which these delicate phenomena exist. It is clear that the interesting physics associated with *PT* symmetry breaking stems from the presence of *EP*s. However, although ***PT*** invariance guarantees that a Hamiltonian will pass exactly through such a singular parametric coordinate, *EP*s are not limited to these specific problems. In fact, they are common features of complex parameter spaces. The most complete investigations of the dynamics of a system in the vicinity of *EP*s have centred on lossy microwave cavity experiments[*82–84*]. These studies benefit from the ability to meticulously control the structural properties of the setup, thereby manipulating the corresponding electromagnetic eigenmodes. Just as importantly, the ease with which local field probes and sources can be created also enables the resonances to be selectively excited and their resonant frequencies and field patterns to be measured in fine detail. Consequently, parametric loops which encircle an *EP* have been shown to cause the eigenstates to exchange eigenvalues whilst one of the modes picks up a path dependent geometric phase, signifying the presence of a non-trivial topological structure[*83*]. Here we wish to extend our discussion presented in (3.4) to the more general case of non-Hermitian and non-*PT* symmetric metasurfaces in order to observe this interesting behaviour near a polarisation based *EP*.

In particular, we return to Eq.3.14 but this time the constraint $g_x = g_y$, forcing orthogonal dipoles to radiate with the same efficiency, is relaxed. Maintaining a square lattice

of meta-molecules $G_{xx} = G_{yy}$, the Jones matrix is given, up to an additional term proportional to the identity matrix, by

$$\boldsymbol{J} = A\begin{pmatrix} g_x^2(\omega - \omega_y + i\gamma_y) & -g_x g_y G_{xy} \\ -g_x g_y G_{xy} & g_y^2(\omega - \omega_x + i\gamma_x) \end{pmatrix}. \quad [3.22]$$

Importantly, in Eq.3.22 $(Re(\tilde{t}_{xx}) - Re(\tilde{t}_{yy}))$ depends on ω. This means that the polarisation response must now be dispersive. Therefore, unlike a balanced system governed by Eq.3.16, a range of coordinates within a non-Hermitian parameter space can be explored by measuring the transmission spectrum through a single metasurface with $g_x \neq g_y$. Moreover, Eq.3.22 is *PT* symmetric at a single frequency $\omega = (\omega_y g_x^2 - \omega_x g_y^2)/(g_x^2 - g_y^2)$ and thus, an *EP* will be found after varying the coupling G_{xy} or dissipation parameters $g_{x,y}$ and $\gamma_{x,y}$. The eigenvalue map for an example of such a variation is illustrated in Figure 3.16a. From this we can see

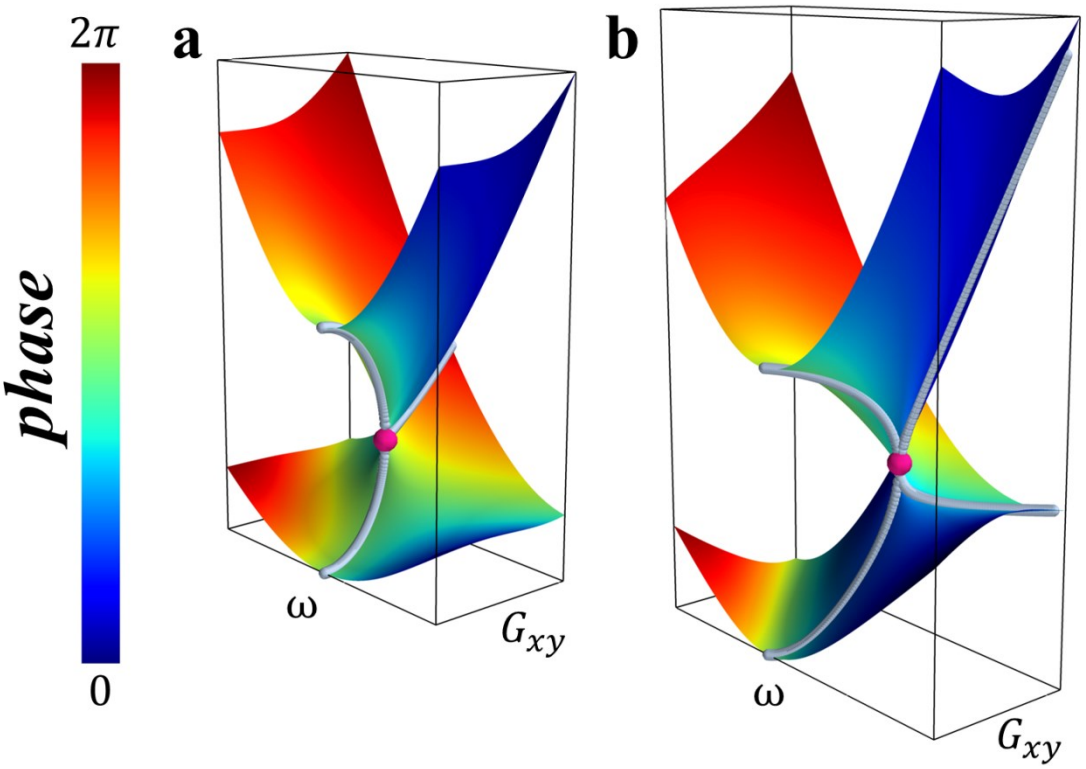

Figure 3.16: Dispersion of transmission coefficients for Polarisation eigenstates of non-Hermitian metasurfaces. Eigenvalue amplitudes from matrix in Eq.3.19 with $\boldsymbol{\omega_y = \omega_x = 2}$, $\boldsymbol{\gamma_y = \gamma_x = 1}$, $\boldsymbol{g_y = 1}$, $\boldsymbol{g_x = 2.5}$. In (b) a constant anti-Hermitian term has also been added $\boldsymbol{Im(\tilde{t}_{xy}) = 0.5}$. *EP*s are marked by pink dots and grey lines represent coordinates for which either $\boldsymbol{Re(\Delta\tilde{t}_{eig}) = 0}$ or $\boldsymbol{Im(\Delta\tilde{t}_{eig}) = 0}$.

clearly the reason behind the strange behaviour of *PT* symmetry breaking. Rather than two independent polarisation states, the transmission through an anisotropically lossy structure is governed by a single self-intersecting Riemann surface. This is counter intuitive given the fact that we arrived at Eq.3.22 by hybridising two well defined oscillators. More than simply causing eigenstate coalescence the *EP* is, therefore, a parametric discontinuity which must exist to allow the manifold to be smooth elsewhere. As such, the effect that an *EP* has on the wider parameter space is reminiscent of Dirac like linear degeneracies. In fact, Eq.3.22 can be analysed in the context of a complex extension to Eq.2.5, with degeneracies once again representing effective monopoles[*89*]. Correspondingly, the *EP* found in the description of light transmitted through our anisotropic metasurface is topologically protected. This is seen in Figure 3.16b. By adding an imaginary part to G_{xy}, breaking the *PT* symmetry of Eq.3.22 for all ω, the eigenvalue map is altered significantly and the *EP* changes position but remains intact.

To realise such a metamolecule we need to incorporate antennas with similar resonant frequencies but sufficient structural differences to produce $g_x \neq g_y$. This situation is akin to the condition for observing EIT in metamaterials, as discussed in (2.3.5). Those studies,

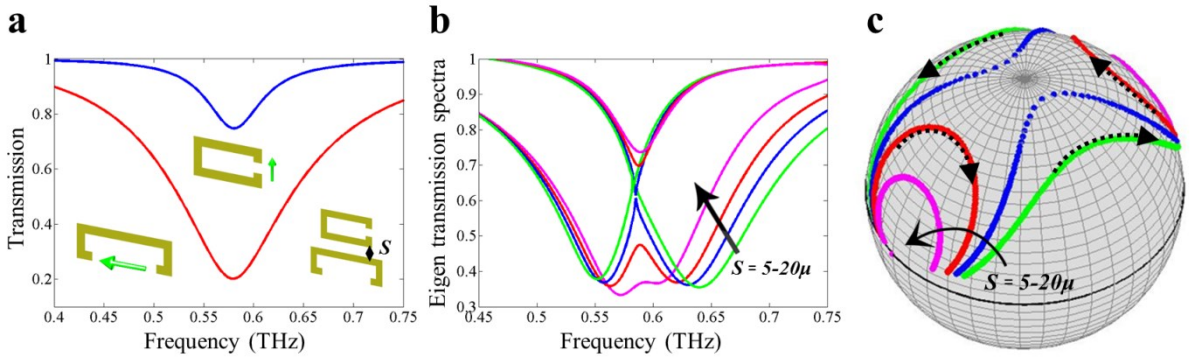

Figure 3.17: Non-Hermitian metasurface near EP. a) Transmission through relatively bright and dark metaatoms in isolation. b) Eigen-transmission spectra for metamolecules, an example of which is shown in 'a', with SRR separation 'S' varied between 5 (green) and 20μ (purple). c) polarisation eigenstates corresponding to 'b', with dashed arrows showing a cyclical variation in the eigenstates which represents two loops around the EP in the $(\boldsymbol{\omega} - \boldsymbol{G_{xy}})$ parameter space.

however, simply sought to maximise both the mutual interaction and overall loss contrast between the elements, leading logically to the use of a completely dark quadrupole mode. Here on the other hand, the difference in radiative loss needs to be roughly balanced by the coupling strength and so a meta-atom which can radiate via a small but finite dipole moment is required. Consequently, SRRs are again chosen to be the subcomponents of our metamolecule. As the electric dipole strength associated with a subwavelength capacitive gap is proportional to the corresponding plate separation, perpendicular rings with different gap sizes can be employed to ensure that $g_x \neq g_y$, while the resonant frequencies can be realigned by varying the relative areas they enclose, shown in Figure 3.17a. Although Ohmic loss is necessary it doesn't have to be anisotropic and so gold has been used for both structures to simplify the fabrication process. Figure 3.17b reveals the eigen-transmission spectra for different resonator positions within the unit cell. Clear correspondence between these simulated results and Figure 3.16a is seen, with the qualitative nature of the dispersion changing dramatically when the *EP* is crossed. The unique topological structure of this parameter space also shows up in the frequency dependence of the polarisation eigenstates, shown in Figure 3.17c. For weak coupling two loops appear on the Poincare sphere located near the linear *x* and *y* polarised coordinates, representing the perturbed responses of the isolated rings. For strong coupling however, open curves are formed connecting between *x* and *y* polarisations, describing eigenstates which contain an equal contribution from both rings. A cyclical path returning to the same state after encircling the *EP* is also drawn, corresponding to a double loop in the underlying parameter space, which agrees with previous experiments performed using microwave cavities[*83*, *84*].

Although Figure 3.17b and c present results obtained after diagonalising the Jones matrices, interesting behaviour can also be seen in the transmission directly without post processing. Figure 3.18 shows the circularly polarised transmission spectra. As expected from

section (3.4), close to the critical coupling strength and for $\omega = (\omega_y g_x^2 - \omega_x g_y^2)/(g_x^2 - g_y^2)$ the conversion from LCP to RCP vanishes while significant conversion from RCP to LCP remains. However, unlike Figure 3.10l where a flat response is found, in Figure 3.18a t_{rl} can be seen to disperse almost linearly away from the *EP*. This can be explained by looking at the

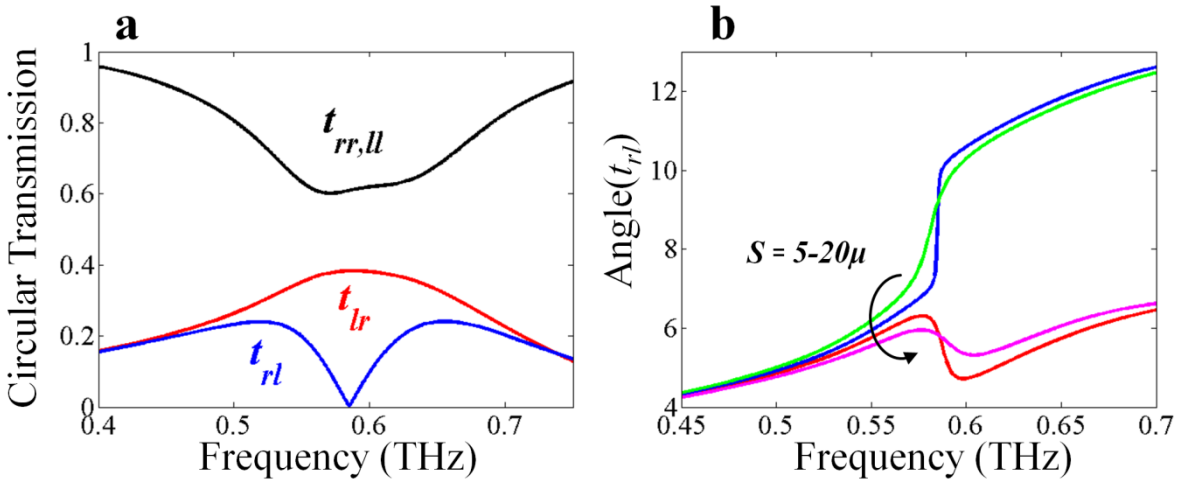

Figure 3.18: Circularly polarised transmission through non-Hermitian metasurface near *EP*. a) Transmitted amplitudes for metamolecule configuration closest to the *EP*, corresponding to the blue curve in Figure 3.17. b) with SRR separation 'S' varied between 5μ (green) and 20μ (purple), with colour coding matching Figure 3.17b and Figure 3.17c.

corresponding phase angle in the wider parameter space. Figure 3.18b reveals that $\arg(t_{rl})$ forms a spiral shape, similar to the real space structure of a Laguerre-Gauss beam. Such a profile must have a discontinuity at the centre which can only happen if the intensity goes to zero. As discussed previously, an *EP* behaves as an effective monopole. The behaviour of t_{rl} in Figure 3.18 can therefore be understood as a manifestation of the geometric phase accumulated by the eigen-polarisation states upon circling the north pole of the Poincare sphere. As well as being of fundamental interest, phase singularities occurring in plasmonic systems have been investigated recently due to their potential for use in sensing applications[*90*].

Next we turn to the experimental observation of a metasurface *EP*. Thus far, we have focussed on the $(\omega - G_{xy})$ parameter space, which can only be mapped out by once again fabricating and comparing a number of different samples or somehow dynamically

modulating the inter ring coupling strength. An important thing to remember, however, is that such an *EP* is topologically robust. So any smooth alteration to the symmetry of the light-metamolecule interaction will modify the relationship between the components of the Jones matrix, potentially shifting the singular coordinate across the real frequency axis. One such alteration that is particularly straightforward to implement is a variation in the incident angle. The reasons we expect this to strongly affect the polarisation response are two-fold. Firstly, from the Fresnel equations, the background transmission from the air to the substrate will become anisotropic, requiring a real diagonal matrix to be added to Eq.3.22. Also the overlap between the dipole moments of the SRRs and the transverse radiation fields will be modified, depending on weather the gap of a particular ring lies in the incident plane, potentially changing g_x or g_y. Although obliquely incident illumination complicates the polarisability

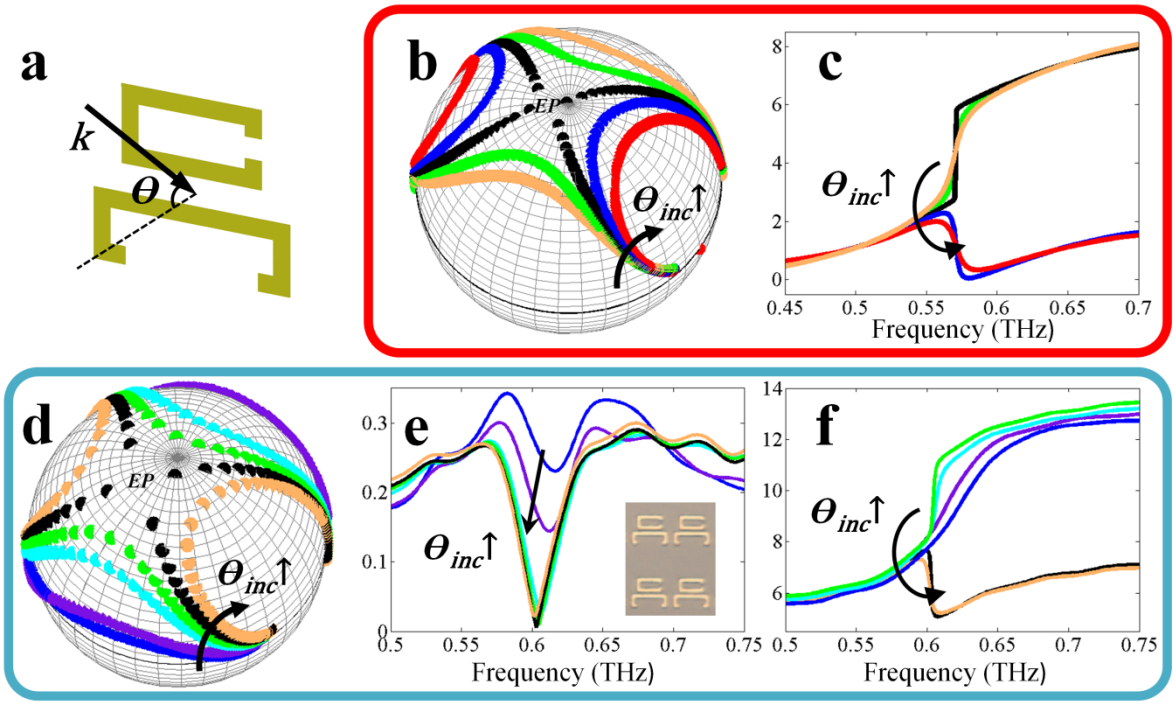

Figure 3.19: Variation of non-Hermitian metasurface transmission with incident angle. a) Illustration of incident plane with respect to metamolecule. b) and c) Simulated eigen polarisation states and $\arg(t_{rl})$, respectively, for θ =0° (orange) to 50° (red). d), e) and f) THz-TDS measurements of the eigen polarisation states, $|t_{rl}|$ and $\arg(t_{rl})$, respectively, for θ =0° (blue) to 43° (orange). Microscope image of the sample is shown in the inset of 'e'.

somewhat, introducing chirality, bianisotropy and also radiative coupling; since the phenomenon in question is rooted in the global properties of the spectral information, we need only concern ourselves directly with the frequency dependence of the Jones matrix. Figure 3.19 reveals our simulated and measured data for incident angle dependent transmission through a single metasurface, showing good agreement. These results can also be seen to closely resemble the behaviour found in Figure 3.17 and Figure 3.18, except that the *EP* has shifted away from LCP. Despite the poor quality of the fabricated sample, remarkably, the measured phase dislocation and associated dark spot in the circular conversion efficiency t_{rl} close to the critical angle, represented by the black curves in Figure 3.19e and f, perform just as well as the ideal periodic structure evaluated numerically. This is a signature of the topological origin of such a spectral feature. We should note that all of the information given in Figure 3.19 has been found from linearly polarised measurements and then transformed using basis transformations. However, this is simply an issue of convenience as linear polarisers perform much better than circular polarisers at THz frequencies. There is also no reason to expect that the phenomenon observed here cannot be reproduced in the optical domain. Although *EP*s occurring within metamaterial transmission/reflection spectra have been investigated previously[*91–93*], to the best of our knowledge, we are the first to demonstrate tuning across such a singularity, allowing the phase gradient to be made arbitrarily steep. In [*90*] it was demonstrated that a similarly robust frequency dependent phase jump, found for the reflection from nanoparticle arrays with a local plasmon resonance close to the Rayleigh cut-off, can be used for extremely sensitive biochemical detection. *EP*s may also, therefore, represent a useful alternative to these devices, relying purely on local anisotropic resonators.

3.8: Chapter Summary

Throughout this chapter we have demonstrated that anisotropic metasurfaces represent a natural platform for investigating non-Hermitian physics. By employing dipolar resonators to selectively absorb specific polarisation states of light and controlling the metamolecule configuration to introduce polarisation conversion, a novel phase transition has been observed, resulting from *PT* symmetry breaking. Polarisation phase transitions have also been predicted to occur along different routes on the Poincare sphere if the phase as well as the amplitude of the near-field interaction can be manipulated. Finally, in the last part of this chapter the topological structure of a non-Hermitian degeneracy found in the description of light propagating through a metasurface with anisotropic radiation coupling was shown to produce a spectral phase singularity. Exploiting their robustness to parametric variations, we have experimentally tuned across an *EP* observed at a critical angle of incidence. For all experimental investigations THz-TDS has been used giving the phase and amplitude of the Jones matrix for transmission through our samples. This data has then been processed to reveal the full eigenmode structure of the problem, providing a convenient tool for analysing a non-Hermitian electromagnetic system in complete detail for a high frequency wave platform, instead of the microwave cavities that have been explored previously.

Chapter 4: Topological Photonic Phase in Chiral Hyperbolic metamaterials

Part of the work presented in this chapter has been published in [*94*], for which I was personally responsible for writing the first draft. The chapter includes blocks of text taken from this publication.

Modern developments in electromagnetic, nanoscale and material sciences have led to tremendous improvements in the performance of optical components, in terms of their efficiencies, sensitivities and miniaturisation. With this unprecedented level of control, researchers are becoming more ambitious in their attempts to apply light to technological problems. An example of this is the desire to develop 3D integrated photonic circuits which mimic their electronic counterparts but could potentially operate at optical frequencies and could therefore process information at a much higher rate. To realise such a device, however, it is imperative that we possess the capability to reliably transmit light between arbitrary points in space. This is difficult to achieve with conventional wave guiding structures because of scattering losses. An approach that has received a lot of attention recently for overcoming these losses is to replicate the topological protection of quantum waves at the boundaries of particular insulating crystals. Specifically, Maxwell's equations have been shown to map to topologically nontrivial quantum Hamiltonians for certain periodic arrangements of special photonic materials. In this chapter, we will investigate the possibility of exploiting topological arguments within the description of polarisation dependent photonic transport for creating highly-confined, robust, one-way waveguides without breaking time-reversal symmetry.

Following an initial discussion of recent proposals and demonstrations of photonic crystal topological insulators, we will investigate the natural spin-orbit interaction that exists for plane electromagnetic waves propagating in homogeneous materials. Metamaterial theory will then be employed to the task of engineering a topologically nontrivial phase in a system with only subwavelength structural variations. Using a combination of analytical and numerical techniques, the existence of topologically protected surface waves will be verified in both the effective medium approximation and for realistic metamaterial structures in the microwave frequency regime.

4.1: Topological Photonic Crystals

The rejection of light at certain frequencies by a one dimensionally periodic arrangement of dielectric layers has been known since Lord Rayleigh's thorough analysis of wave behaviour at the end of the 18 hundreds[*95*]. Nevertheless, higher dimensional versions of such periodic systems were first considered much later. These so called photonic crystals can perfectly reflect light of specified frequencies from a range of incident angles. What's more, the ability of a localised embedded emitter to radiate can be entirely suppressed without the inherent losses associated with metallic cavities. In this sense, a strong analogy can be drawn between photonic crystals and electronic band insulators[*95*]. For the optical domain, structures varying periodically in only two dimensions, with index variations guiding the wave in the third, have become particularly popular due to the relative ease with which they can be fabricated using nanoscale lithography[*96*]. As well as fully localised modes, one dimensional defects within periodic dielectrics can be used as waveguides with properties tailorable to suit a multitude of applications[*97*].

As discussed in (2.1.3), in recent years a fundamentally new type of electronic band insulator has received a lot of attention. These so called topological insulators still prohibit

electrons from travelling through the bulk, but propagating modes allowing current to flow at the boundaries are guaranteed to exist, deriving from the topology of the bulk band structure rather than the detailed formation of the boundaries. Usefully, the non-degeneracy of these modes forces the corresponding electrons to travel in one direction, preventing them from scattering off of lattice defects or imperfections. Importantly, topological properties of such condensed matter systems arise purely from the wave nature of the quantum states rather than the fermionic character of the electrons. This fact has driven a number of groups to search for photonic crystal analogues of topological insulators.

The most straightforward way of creating topologically non-trivial electronic edge states is to apply a magnetic field normal to a 2D metal, leading to the IQHE. By definition photons do not interact with magnetic fields, however, if a DC E/B-field is applied to gyroelectric or gyromagnetic materials, the resulting permittivity or permeability tensors

$$\varepsilon_r, \mu_r = \begin{pmatrix} \alpha & i\delta E_z/B_z & 0 \\ -i\delta E_z/B_z & \alpha & 0 \\ 0 & 0 & \beta \end{pmatrix}, \qquad [4.1]$$

inherit the nonreciprocal form of the induced cyclotron orbits. This response is well known to cause the Faraday Effect in which linear polarisation is rotated upon transmission, similarly to optical activity. In 2008, Ragu and Haldane showed that if a 2D photonic crystal made of such materials was designed such that there exists an isolated Dirac like degeneracy, the application of an external field could lift this degeneracy leading to a complete bandgap between topologically non-trivial bulk bands[*98*]. Physically this process corresponds to counter rotating combinations of orthogonal dipole fields at the Dirac point being energetically separated, in a non-reciprocal form of the type of spin-orbit coupling found in heavy semiconductors. The resulting one-way edge states were experimentally verified later by Wang *et al*[*99*]. More recently, Khanikaev *et al.* showed that a reciprocal equivalent of this spin-orbit interaction could arise from magneto-electric coupling[*100*]. In particular, an

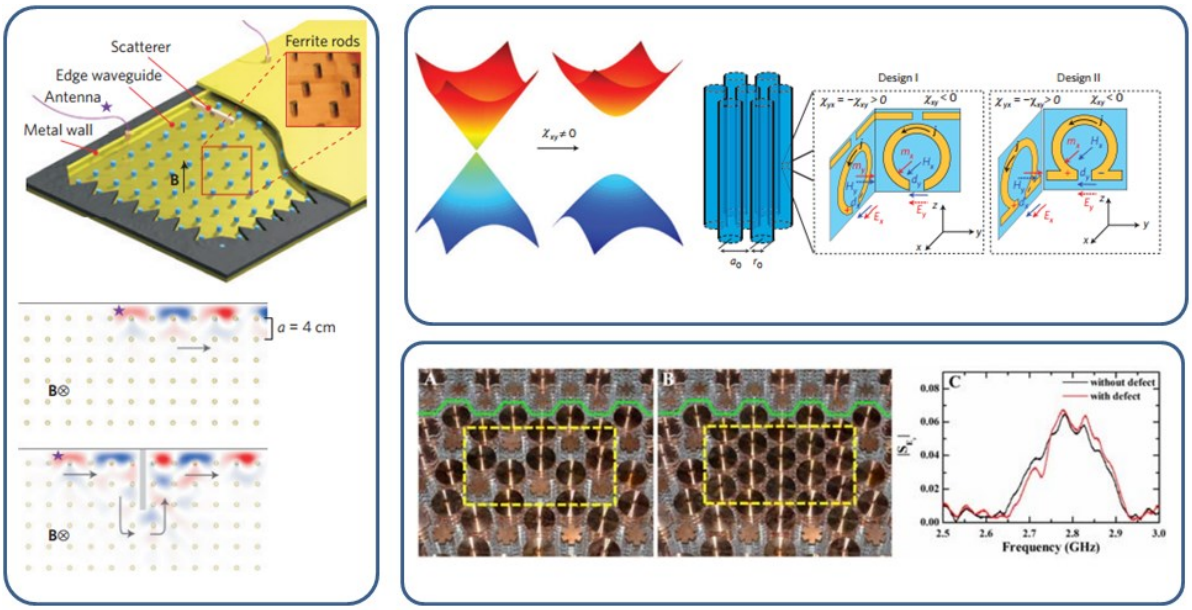

Figure 4.1: 2D Photonic topological insulators from spin orbit coupling. a) An array of gyromagnetic rods give rise to one way back-scatter immune edge states when a ***B*** field is applied[*99*]. b) Dirac point degeneracy of hexagonal photonic crystal is lifted in a topologically nontrivial fashion by employing bianisotopic metamaterials. Two example meta-atom designs for realising this response, composed of SRRs and split wires, are shown[*100*]. c) Images of topologically nontrivial bianisotropic photonic crystal edge without defect (A) and with defect. Very similar transmission is shown in (C) for the corresponding edge modes[*101*].

antisymmetric bianisotropy tensor was proposed which, when applied in the context of a hexagonal photonic crystal, allowed for a mapping between Maxwell's equations and the Kane model for topological graphene. Correspondingly, spin polarised edge states were predicted to exist with counter rotating dipole fields only able to travel in opposite directions. A catch for this approach is that unlike electronic spin which is preserved by time-reversal symmetry due to Kramer's theorem, photonic polarisation is sensitive to the detailed material properties involved. To prevent mixing between counter propagating excitations, an extra constraint $\varepsilon_r = \mu_r$ is required. As this specific form of bianisotropy cannot be found in nature, it was suggested that metamaterials could be employed to realise the desired response. However, the very precise parametric relationships that need to be met, makes the design and fabrication of an appropriate subwavelength structure very challenging. Instead, 2D periodic arrangements of larger objects which lack inversion symmetry in the out of plane direction have been shown to provide the necessary magneto-electric coupling with spin degeneracy,

allowing for a photonic topological insulating phase to be observed experimentally[*101*]. As DC electric/magnetic fields fail to induce a significantly nonreciprocal response above tens of GHz and fabrication tolerances become very important for small scale devices, in practice both of these schemes are limited to microwave frequencies.

An entirely different approach that has also been proposed is to engineer an effective magnetic field for light. This possibility can be understood by considering the fact that Lorentz forces actually enter the electronic Hamiltonian via the vector potential $\boldsymbol{A}(\boldsymbol{r})$, defined by $\boldsymbol{B}(\boldsymbol{r}) = \nabla \times \boldsymbol{A}(\boldsymbol{r})$. Therefore, a periodic scalar potential with a uniform $\boldsymbol{B}$ can always be represented by overlaying a non-periodic spatial variation on to the regular lattice. For example, in [*102*] a 2D resonator array with dynamically modulated coupling strengths was shown to produce one way edge states after a linear gradient in the hopping phase was introduced. Unfortunately, accurate control over the relative phase between many oscillators simultaneously is incredibly difficult to achieve. Time reversal invariant versions of this technique, however, have been more successful. Rechtsman *et al*. for instance demonstrated that the evolution of a light field distribution while propagating through a lattice of helically wound optical waveguides can mimic the motion of a charged particle in a time varying potential[*103*]. In this sense, the behaviour can also be considered as a Floquet Topological Insulator. As long as the periodicity along the propagation direction is maintained, scattering from $\boldsymbol{k}$ and $-\boldsymbol{k}$ is prohibited and so the waves at the surface are protected. Similarly, Hafezi *et al.* have realised an effective vector potential in a SOI platform by treating counter rotating ring resonator modes as spin[*104*]. Coupling each lattice site by a secondary ring, the spin states can be preserved as long as the structures used guide the wave adiabatically. A spatial variation in the coupler lengths can then produce an effective gauge potential, with opposite signs for the two spins, and protected edge states. Both [*103*] and [*104*] rely on carefully

fabricated samples to prevent backscattering as they are only immune to disorder larger than

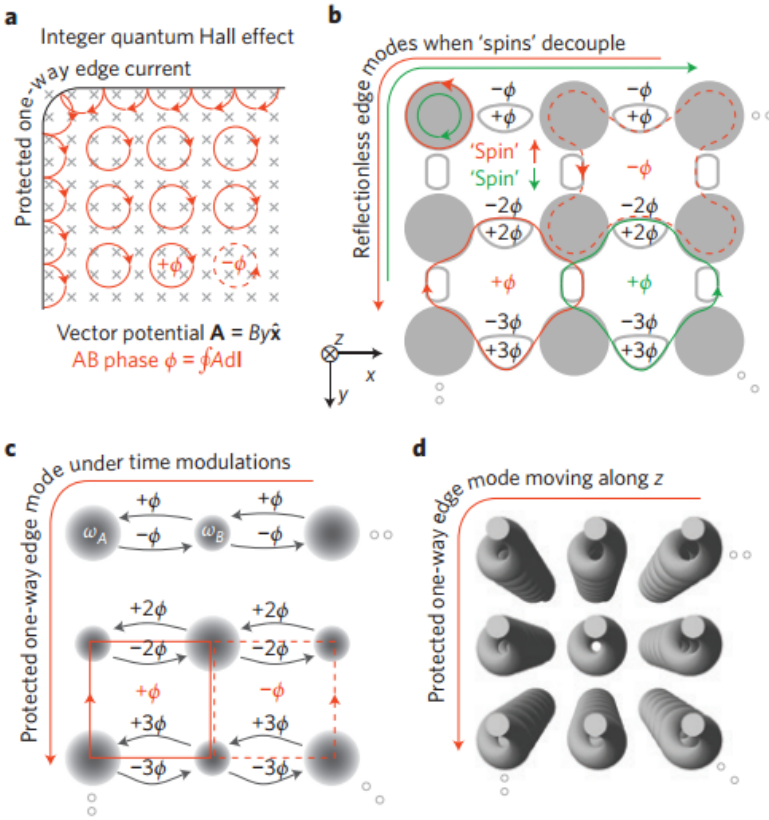

Figure 4.2: Topological photonic phases from effective magnetic fields, reproduced form Ref [*106*]**.** a) Spatial phase variation of bulk and edge states in IQHE. Effective photonic gauge potentials induced by spatially varying b) ring resonators, c) dynamically modulated resonator coupling and d) helical waveguides.

the wavelength. Finally, a photonic analogue of a Weyl semimetal has also been proposed. By considering the effect of Inversion and time reversal symmetry breaking perturbations to a highly symmetric gyroid photonic crystal, pairs of Weyl point degeneracies were found in an otherwise complete band gap. As is known from electronic investigations, these degeneracies act like momentum space monopoles leading to topologically non-trivial surface behaviour[*105*]. Further details regarding the systems discussed above can be found in the review article[*106*].

One thing that these previous schemes have in common is that they all seek to replicate the features of topological quantum systems by energetically separating artificially

engineered counter rotating wave functions. Here we wish to explore topological properties unique to electromagnetic waves. Then by exploiting the power of metamaterials to manipulate the relationship between photonic polarisation and propagation characteristics, a fundamentally new topologically non-trivial phase will be proposed.

4.2: Electromagnetic Plane Waves and Momentum Space Monopoles

Clearly, the topology of a Bloch state defined on a periodic reciprocal lattice can have some remarkable consequences for wave propagation within crystal structures. However, one of the first systems to which Berry's geometric analysis was applied was classical wave optics. Even in this fairly simple setting fascinating results can emerge.

Taking perhaps the simplest electromagnetic problem of a homogeneous space filled with an isotropic dielectric $n = \sqrt{\varepsilon_r}$, the source free Maxwell equations admit plane wave solutions with the isotropic dispersion relation $\omega = c|\boldsymbol{k}|/n$. The corresponding fields are constrained to lie in the plane $\boldsymbol{k} \cdot \boldsymbol{E} = \boldsymbol{k} \cdot \boldsymbol{B} = 0$ and are related to each other by $\boldsymbol{k} \times \boldsymbol{E} = \frac{|\boldsymbol{k}|}{n}\boldsymbol{B}$. For circular polarisations $\boldsymbol{B} = \sigma i \boldsymbol{E}$, where $\sigma = \pm 1$ corresponding to LCP and RCP, the general solution for $\boldsymbol{E}$ can then be written as

$$\boldsymbol{k} \times \boldsymbol{E} = \sigma \frac{|\boldsymbol{k}|}{n} \boldsymbol{E}. \qquad [4.2]$$

Interestingly, the left hand side of this equation can be expressed in terms the spin-1 matrices $(S^a)_{bc} = -i\varepsilon_{abc}$(where $\varepsilon_{abc}$is the Levi-Civita symbol) as $\boldsymbol{k} \times \boldsymbol{E} = (\boldsymbol{k} \cdot \boldsymbol{S})\boldsymbol{E}$. This reveals a formal equivalence between the role played by $\boldsymbol{k}$ for electromagnetic wave propagation and the action of a magnetic field $\boldsymbol{B}$ on a spin-1 particle

$$(\boldsymbol{B}\cdot\boldsymbol{S})|\boldsymbol{\psi}\rangle = \lambda|\boldsymbol{\psi}\rangle. \qquad [4.3]$$

We have already seen in (2.1.2) that in the presence of a magnetic field which is slowly and cyclically rotated, a spin-½ particle will accumulate a geometric phase dependant on the particular shape swept out by $\boldsymbol{B}[11]$. This phase factor originates from the monopole sources of Berry curvature generated by the square root singularity of the eigenvalues at the origin $\boldsymbol{B} = 0$. Generalising to spin-s, the form of the curvature remains the same but the topological charge associated with the monopoles becomes $s[11]$. Therefore, a circularly polarised photon whose propagation direction is varied adiabatically will experience a Berry curvature field

$$\boldsymbol{\Omega}_{\sigma} = \sigma\frac{\boldsymbol{k}}{|\boldsymbol{k}|^3}. \qquad [4.4]$$

The consequences of this can be observed in a fairly simple experiment. By sending a linearly polarised beam of light down a single mode optical fibre which is helically wound in space, the polarisation can be seen to rotate after $\boldsymbol{k}$ returns to the same direction as the incident excitation. Assuming an ideal system of a perfectly smooth and round fibre with a

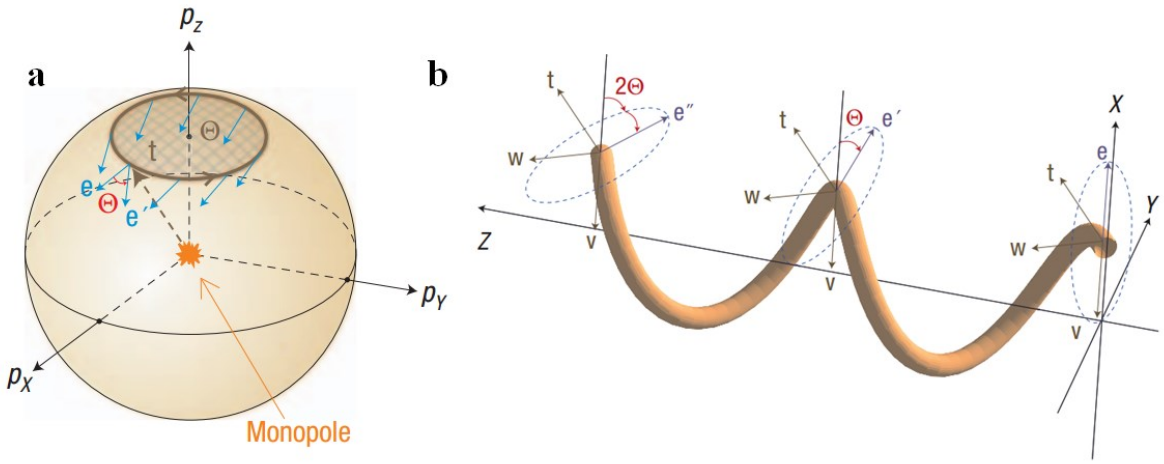

Figure 4.3: Geometric phase accumulated by electromagnetic wave propagating through helical fibre, reproduced from Ref [*108*]**.** a) Parallel transport of field vector produces rotation **Θ** after travelling around a circle on the Equi-frequency sphere, which can also be considered as a geometric phase driven by the enclosed Berry flux produced by a topological monopole. b) Schematic representation of polarisation rotation within helical fibre.

sufficiently gentle curve, the left and right handed components of the linear mode can be treated independently. As $|\boldsymbol{k}|$ remains fixed, twists in the guiding geometry can be represented by paths on the equi-frequency sphere. Applying Eq.4.4 within Eq.2.4 for circular loops on the sphere parameterised in terms of their elevation angles ϑ, the dependence of the berry phase on the pitch angle of the coil can then be shown to take the form

$$\Phi_\sigma = 2\pi\sigma(1 - \cos\vartheta). \qquad [4.5]$$

The geometrically accumulated phase difference $2\Phi_\sigma$ between LCP and RCP waves can therefore be seen to mimic the polarisation rotation that occurs within optically active media[*107*].

Importantly, even though the dynamic reorientation of a particle with relativistic spin is a truly quantum problem, monopoles in the description, which are at the heart of the interesting physics exhibited by this system, arise purely from Dirac points in the dispersion relation. For this reason, path dependent changes to the polarisation of an electromagnetic wave as a result of alterations made to its trajectory can be derived simply from Maxwell's classical theory. With the transversality conditions $\boldsymbol{k}\cdot\boldsymbol{E} = \boldsymbol{k}\cdot\boldsymbol{B} = 0$, the rotation of a linear excitation after travelling through a twisted fibre can be found by parallel transporting the $\boldsymbol{E}$ field vector tangent to the $\boldsymbol{k}$-sphere along a specified curve[*108*]. From this perspective, the inherent relationship between photonic polarisation and $\boldsymbol{k}$, commonly referred to as spin orbit coupling, also has interesting consequences beyond the limits of adiabatic evolution. For example, the transmission or reflection of light obliquely incident upon a dielectric interface will experience a lateral shift, with LCP and RCP moving in opposite directions. This is known as the spin Hall effect of light as it is similar to the spin dependant deflection of electrons that occurs in certain heavy semiconductors[*109*]. However, although this

comparison is often used, an important difference exists between these two phenomena. While electrons require particular crystal structures with broken inversion symmetry to provide a spin-orbit interaction, photons are intrinsically spin-orbit coupled, experiencing Hall type deflections purely from variations in momentum. Physically, the distinction arises because electrons, unlike photons, have a finite rest mass leading to quadratic rather than linear dispersion at low energies. It is this inherent property of light waves that we wish to explore and exploit in the coming sections.

Returning to the momentum space of electromagnetic waves in a simple homogeneous, isotropic medium, we note that as well as considering the Berry flux through open surfaces we can also integrate Eq.4.4 on an entire equi-frequency sphere. Rather than describing the geometric phase associated with a particular ray trajectory, this gives the net topological charge contained within that sphere, $q = \sigma 4\pi$. As discussed in (2.1.2/3), this calculation will actually produce the same q for any closed surface in the wider $\omega(\boldsymbol{k})$ space as long as it contains the monopole at $|\boldsymbol{k}| = 0$, otherwise $q = 0$. q is therefore said to be a topological invariant. Making a connection with the systems discussed in the previous section, the Chern number $C = q/2\pi$. Despite being fairly obvious from a geometric interpretation of classical wave theory, the result $C = \pm 2$ for such a simple photonic system is rather exciting. That is because it is these Chern invariants that are at the heart of the quantum Hall type phases which have received so much attention recently. However, Due to the degeneracy that exists between LCP and RCP modes, such a medium is still topologically trivial. We are, on the other hand, presented with an intriguing possibility. If we could engineer the dispersion relations for LCP and RCP waves independently, perhaps we could create a topologically non-trivial phase within a completely homogeneous environment. As will be demonstrated in the next section, metamaterials are ideally suited to this task.

4.3: Non-trivial Topology in Effective Media

In this section, guided by concepts outlined in (2.3), we will explore the possibility of creating a topologically non-trivial, homogeneous medium, within which wave propagation is fully determined by the local permittivity ε_r, permeability μ_r and magneto-electric γ tensors, defined via the constitutive relations Eqs.2.46/7. Specifically, starting from free-space which has already been shown to exhibit an interesting topological structure, we wish to find a parametric configuration with EFSs well separated in $\boldsymbol{k}$-space and possessing non-zero Chern numbers. The most important consideration for this endeavour is the role played by the photonic helicity. Although we have placed great emphasis on the existence of topological charges for free-space waves, the corresponding Berry curvature fields only emerge after fixing the polarisation to either LCP or RCP. Therefore, while many material parameter combinations may provide an appropriately birefringent response, lifting the polarisation degeneracy, they may not preserve the topological character of the original $\boldsymbol{k}$-spheres. A logical first step then is to consider an isotropic but chiral, or optically active, medium with a non-zero scalar valued γ. In this case, the degenerate modes for $\gamma = 0$ separate into two new spherical EFSs with different radii $|\boldsymbol{k}_\sigma| = \omega n_\sigma / c$, where $n_\sigma = \sqrt{\mu_r \varepsilon_r} + \sigma\gamma$, as shown in Figure 4.4c. As Eq.4.2 still holds, the corresponding Chern numbers once again take the values $C = \sigma 2$. Crucially, however, these topological invariants are now unambiguous as they do not depend on the representation of the fields. In this respect we have achieved our goal, with different Chern numbers belonging to eigenstates which occupy distinct regions of $\boldsymbol{k}$-space. Specifically, $C = 2\mathrm{sgn}(\gamma)$ and $C = -2\mathrm{sgn}(\gamma)$ for states at large and small $\boldsymbol{k}$, respectively. Our original motivation for engineering such a response was the expectation that it would lead to interesting boundary behaviour when the medium is truncated. Unfortunately, in the linear regime energy conservation only fixes the frequency of an electromagnetic wave, and

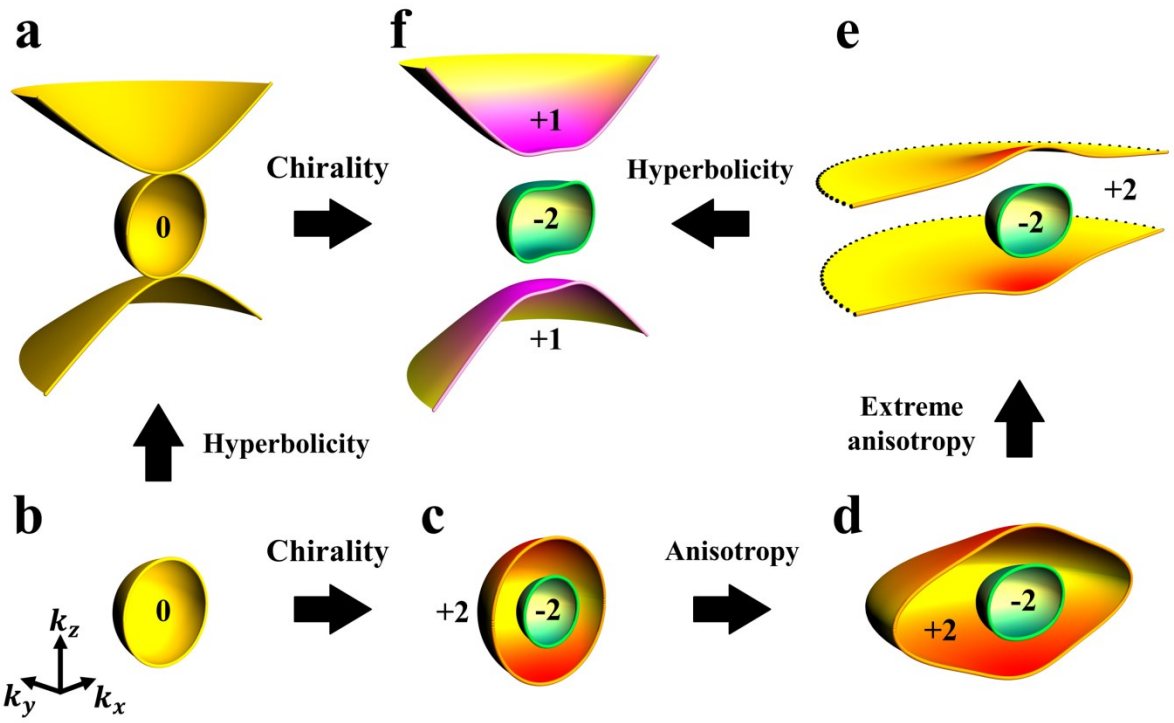

Figure 4.4: Evolution of equi-frequency surfaces and their Chern numbers due to changing material parameters. a, hyperbolic medium ε_r = diag(4, 4, -3), γ = 0. b, isotropic non-chiral medium ε_r = 4, γ = 0. c, isotropic chiral medium ε_r = 4, γ = 0.5. d, anisotropic chiral medium ε_r = diag(4, 4, 30), γ = 0.5. e, Highly anisotropic chiral medium ε_r = diag(4, 4, ∞), γ = 0.5, black dotted lines show the plot boundary of infinitely extended sheets. f, hyperbolic chiral medium ε_r = diag(4, 4, -3), γ = 0.5. μ_r is set to 0.5 for all plots. The numeric label assigned to each surface represents its associated Chern number. Figure and caption adapted from [*94*].

so bulk propagating states will, in general, dominate a photonic system if they exist at the excitation frequency. However, from section (2.2.4) we know that surface modes can still be supported in voids within the bulk dispersion of a transparent material as long as translational symmetry is present. In particular, the absence of travelling wave solutions spanning an entire 2D plane in $\boldsymbol{k}$-space allows surface and volume waves to be completely decoupled via translational invariance along a single Cartesian coordinate. Such a system can be considered as an interface between a pair of 2D photonic insulators. To satisfy this condition, the simple chiral medium (Figure 4.4c) which only has radially separated EFSs, requires further modifications. Anisotropy in particular can be used to introduce a directionally dependent birefringence. For the most general case of tensor-valued $\boldsymbol{\varepsilon_r}$, $\boldsymbol{\mu_r}$ and $\boldsymbol{\gamma}$, applying the constitutive relations Eqs.2.46/7 to Maxwell's equations, we obtain the plane wave equation

$$\boldsymbol{\mu_r}[\boldsymbol{k}\times\boldsymbol{\mu_r^{-1}}\boldsymbol{k}\times+ik_0(\boldsymbol{\gamma}\boldsymbol{\mu_r^{-1}}\boldsymbol{k}\times+\boldsymbol{k}\times\boldsymbol{\mu_r^{-1}}\boldsymbol{\gamma})+k_0^2(\boldsymbol{\varepsilon_r}-\boldsymbol{\gamma}\boldsymbol{\mu_r^{-1}}\boldsymbol{\gamma})]\boldsymbol{E}=0, \quad [4.6]$$

where $k_0 = \omega/c$ is the free-space wave number. Working with Eq.4.6 in matrix form $\boldsymbol{M}\cdot\boldsymbol{E}=0$ and starting with the simplified situation of scalar valued μ_r and γ but a uniaxial permittivity tensor $\boldsymbol{\varepsilon_r} = diag(\varepsilon_i, \varepsilon_i, \varepsilon_z)$, the dispersion relation is given by $|\boldsymbol{M}| = 0$,

$$\begin{vmatrix} k_y^2+k_z^2+k_0^2(\gamma^2-\mu_r\varepsilon_i) & -k_xk_y+2i\gamma k_0k_z & -k_xk_z-2i\gamma k_0k_y \\ -k_xk_y-2i\gamma k_0k_z & k_x^2+k_z^2+k_0^2(\gamma^2-\mu_r\varepsilon_i) & -k_yk_z+2i\gamma k_0k_x \\ -k_xk_z+2i\gamma k_0k_y & -k_yk_z-2i\gamma k_0k_x & k_y^2+k_x^2+k_0^2(\gamma^2-\mu_r\varepsilon_z) \end{vmatrix} = 0. \quad [4.7]$$

Setting $k_0 = 1$ and numerically mapping out the $\boldsymbol{k}$ coordinates which satisfy Eq.4.7, we can then investigate how changes to the material parameters affect the shape of the EFSs. In the following, a continuous parametric transformation from an isotropic, chiral medium to a topologically non-trivial medium with complete voids in $\boldsymbol{k}$-space is described.

By introducing anisotropy along the z direction such that $\varepsilon_z > \varepsilon_i$, both $\boldsymbol{k}$-spheres, shown in Figure 4.4c, become elliptically distorted, with the outer surface experiencing a larger deformation, *i.e.* the in-plane radius k_r is seen to increase dramatically, as shown in Figure 4.4d. Further increasing ε_z towards infinity then causes k_r of the outer $\boldsymbol{k}$-surface to become extremely large (Figure 4.4e). While the Berry curvature distribution, plotted in Figure 4.5, loses its uniformity in such a highly anisotropic system, with increased concentration near $k_r = 0$ and decaying to zero for $k_z \to 0$, as long as the two EFSs do not reconnect throughout this transformation, their topological identities, and therefore Chern numbers, must be preserved. Figure 4.4f shows that finally pushing ε_z through ∞ to negative values while keeping ε_i fixed acts to transform the outer $(\sigma\gamma > 0)$ $\boldsymbol{k}$-surface from a closed surface to a slightly deformed two-sheeted hyperboloid, while the inner $(\sigma\gamma < 0)$ $\boldsymbol{k}$-surface once again remains closed. The Chern number of the central $(\sigma\gamma < 0)$ $\boldsymbol{k}$-surface is therefore unaltered with respect to the isotropic case, $C = -2sgn(\gamma)$, while the two hyperbolic sheets

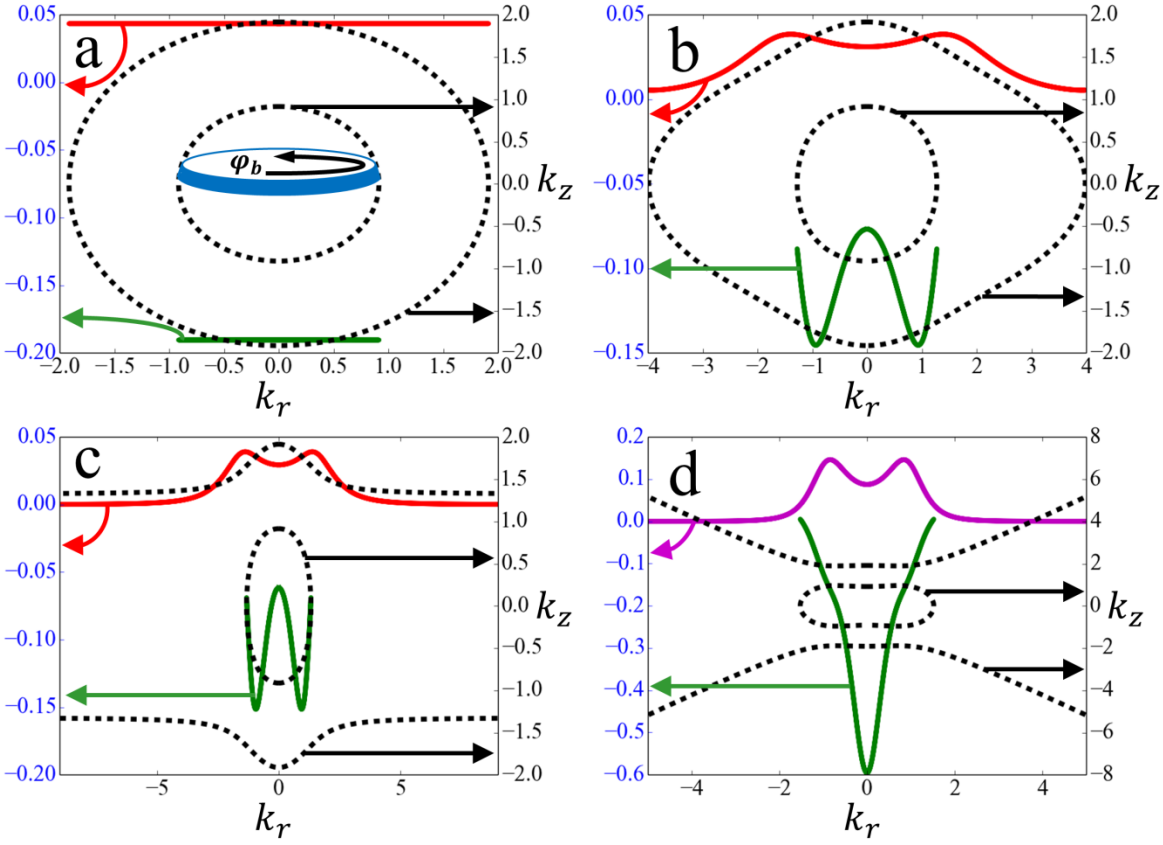

Figure 4.5: EFS Berry curvature distributions. a, b, c and d correspond to Figure 4.4c, d, e and f, respectively. Dashed curves plotted on right y-axes (coloured black) represent radial EFCs $\boldsymbol{k_z}\left(\boldsymbol{k_r} = \sqrt{\left(\boldsymbol{k_x^2} + \boldsymbol{k_y^2}\right)}\right)$ and solid curves plotted on left y-axes (coloured blue) represent the associated k dependent Berry curvature distributions, green=inner contours and purple/red=outer contours. The curvature has been calculated by numerically differentiating the $\boldsymbol{k_r}$ dependent berry phase and normalising against the k-surface area, as illustrated in 'a'.

possess identical Chern numbers that sum to the opposite value, i.e., $C = sgn(\gamma)$ for each sheet. The chiral hyperbolic metamaterial thus displays three well separated and topologically non-trivial EFSs. In particular, two complete voids can be seen in the z direction meaning that only evanescent modes exist for this particular range of k_z. Similarly, light is unable to propagate through a simple dielectric for $|\boldsymbol{k}| > n\omega/c$. But, we know from above that the Chern numbers vanish for this medium due to the degeneracy between LCP and RCP waves. In fact, the fundamental difference between these two cases can only be discerned at an interface formed between the chiral-hyperbolic and dielectric media. At such an interface, a

topological transition should guarantee the existence of a surface wave in the forbidden regions of the bulk dispersion.

4.4: Topologically Protected Surface Waves

We now turn to studying how these topological features manifest themselves on the boundary of our metamaterial. In what follows we investigate systems with continuous translational invariance in the z direction, thereby conserving k_z. The topologically non-trivial EFSs are then expected to be joined by surface equi-frequency arcs, similar to Fermi arcs in topological semimetals. To confirm this, now we solve for surface waves at a planar interface between a semi-infinite chiral hyperbolic medium and a semi-infinite vacuum. As well as requiring the metamaterial's permittivity to be hyperbolic, choosing positive tensor elements that are significantly greater than one ensures that there exists a range of k_z values for which bulk waves are prohibited on both sides of the boundary. The general method of solving for propagating electromagnetic modes confined to the interface between materials with different properties was outlined in section (2.2.4). Here we follow the same prescription except for one slight deviation. Usually the components of $\boldsymbol{k}$ for waves travelling through a lossless medium are either real or imaginary. From Eq.4.7, however, we find that between the chiral hyperbolic EFSs they can actually take complex values. Unlike for SPPs or Dyakonov waves, with our chiral-hyperbolic medium we therefore need to look for solutions with the wave vector normal to the interface k_y being a complex number. To check that such an excitation is consistent with the absence of loss in the system, the Poynting vectors have been calculated to make sure that $Re(P_y) = 0$. Due to the problem's complicated algebraic form, $k_y(k_x, k_z)$ and the corresponding $\boldsymbol{E}$ and $\boldsymbol{H}$ fields have been solved for numerically by sweeping through the $k_x k_z$-plane within Eq.4.6/7. Using these results, solutions to the boundary condition matrix have then also been found numerically. In Figure 4.6a the results of

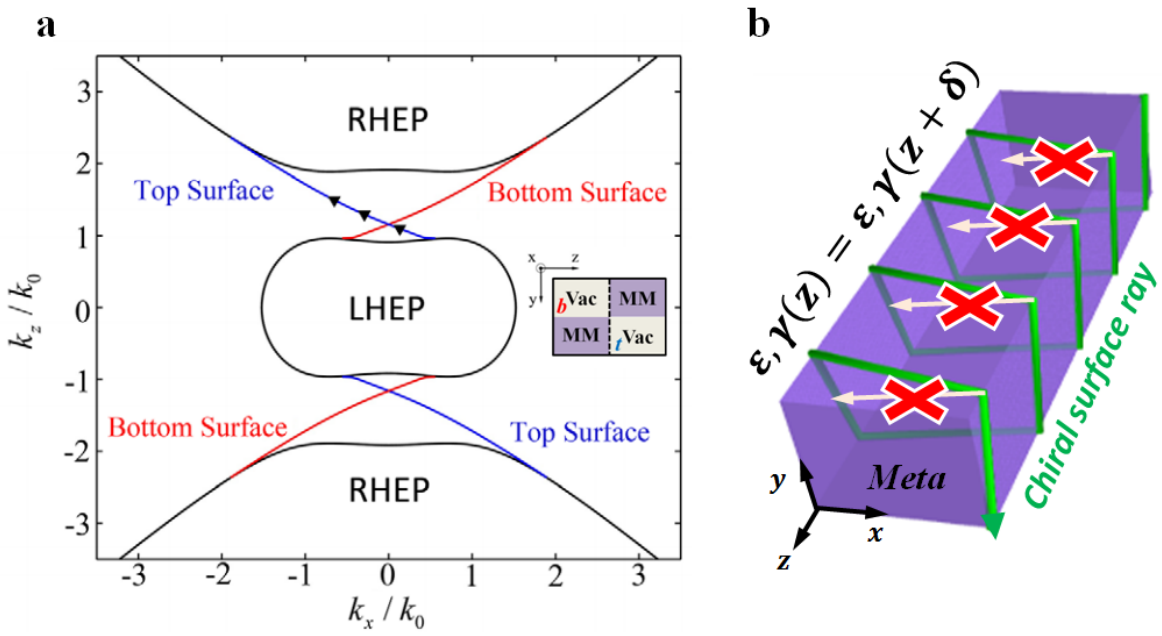

Figure 4.6: Topologically protected surface states at the interface between a chiral hyperbolic metamaterial and a vacuum. a, Volume (black) and Surface (red and blue) state dispersion for boundary in $\boldsymbol{x-z}$ plane with top (bottom) surface defined by metamaterial (vacuum) occupying the half space, $y < 0$, as depicted in the inset. The parameters of the metamaterial are ε_r = diag(4, 4, -3), $\gamma = 0.5$. $\mu_r = 0.5$; the black triangles represent the coordinates in k space corresponding to surface states in Figure 4.7(a-c), LHEP and RHEP stand for Left and Right handed elliptical polarisation respectively. b, Chiral surface state propagating around a cylindrical metamaterial surrounded by air, despite the existence of sharp corners back-scattering is forbidden due to the absence of anticlockwise modes. The dimensions of the metamaterial in the $\boldsymbol{x-y}$ plane are assumed to be much bigger than the surface wave decay length such that the surface propagation characteristics correspond approximately to subplot (a). Figure and caption modified from [*94*].

this calculation reveal that a given surface can support just one propagating mode connecting the bulk EFSs with different Chern numbers, as expected. Importantly, the spatial separation of left and right moving surface waves at a certain k_z prevents the occurrence of backscattering from any z-invariant disorder, as schematically illustrated in Figure 4.6b.

This immunity to backscattering has also been confirmed using full wave simulations, shown in Figure 4.7, in which a right moving surface wave propagates seamlessly around a large step defect. COMSOL is used to simulate the propagation of surface states at the interface between the topological metamaterial and vacuum. The simulation is performed in the x-y plane for different propagation constants k_z in the gap between the bulk EFSs, as indicated in Figure 4.6a. As shown by Figure 4.7a-c, the surface waves are not reflected or

scattered by the presence of sharp corners. When we change the sign of the metamaterial's chirality parameter $\gamma \rightarrow -\gamma$ the surface wave still only goes one-way but now travels in the opposite direction, as shown by Figure 4.7d. This is because the helicities of the bulk polarisation states have changed sign while the dispersion is unaffected and so all of the EFS

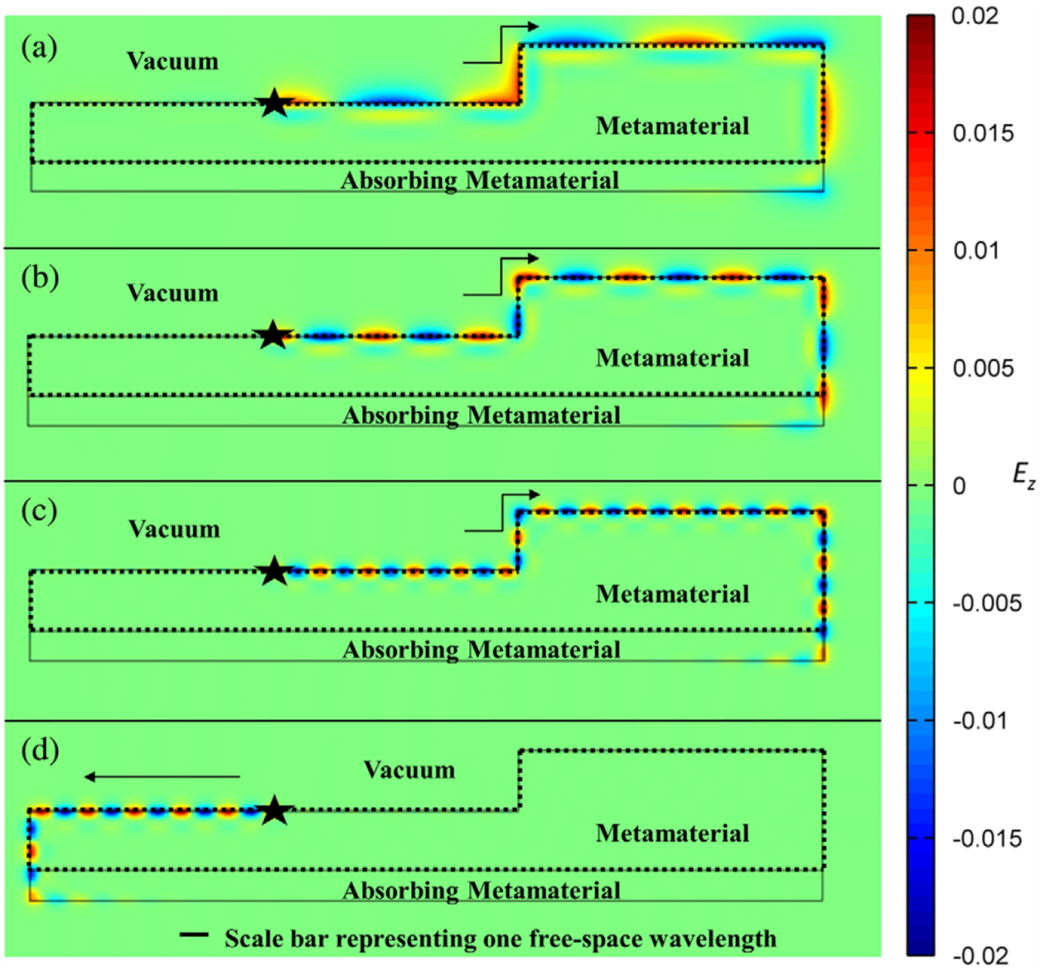

Figure 4.7: Full wave simulations of topologically protected surface waves. a-c, cross section view (x-y plane) of the field distribution at an interface between a hyperbolic chiral metamaterial and vacuum is shown with stars representing line sources with a z dependant phase gradient designed to excite electromagnetic waves with $k_z = 1.1k_0$ (a), $k_z = 1.3k_0$ (b) and $k_z = 1.5k_0$ (c), where k_0 is the free-space wavenumber. The metamaterial parameters are the same as in Fig. 6. As k_z is in the topological band gap a single surface wave can be seen propagating to the right moving smoothly through a step defect placed in its path due to the absence of left moving solutions. d), field distribution for a topological metamaterial with a negative chirality parameter γ = -0.5 at $k_z = 1.5k_0$. As the sign of the chirality parameter γ is reversed the direction of propagation is switched to the left. In all simulations an absorbing layer with the same material properties as our topological metamaterial except for a large imaginary component added to the permittivity has been used to prevent the surface waves from interfering with themselves, allowing the unidirectionality of the boundary modes to be seen clearly. Figure and caption from [*94*].

Chern numbers must change sign accordingly. These surface waves are therefore confirmed to be topologically protected.

Although the topological metamaterial parameters considered thus far are remarkably simple from a theoretical stand point, isotropic chirality to date presents some experimental challenges. However, by making further adjustments to the material properties whilst ensuring that the EFSs remain well separated and thus retain the same Chern numbers, it is easy to show that we have far from exhausted the topologically non-trivial parameter space. For example, returning to Eq.4.6 and repeating the Surface wave calculation above with biaxial permittivity and a tensor valued $\boldsymbol{\gamma} = diag(\gamma_x, \gamma_y, \gamma_z)$, the existence of non-tivial topology in metamaterials with very low symmetry can be investigated, as shown in Figure 4.8. It turns out that our metamaterial is not only simple to design but is highly robust since the non-trivial topology persists in a large portion of the full parameter space, with only two requirements that need to be satisfied. The first of these requirements is the existence of chirality. Importantly however, this chirality need not be isotropic. Amazingly, a chirality tensor with just a single in-plane component, orthogonal to the axis of the negative permittivity, is required for topologically non-trivial EFSs to exist, as shown in Figure 4.8a and 4.8b. The second constraint is that the metamaterial must possess unbounded EFSs. This can be achieved for any hyperbolic permittivity tensor with only a single negative component, but this tensor does not have to be uniaxial, as shown in Figure 4.8c and 4.8d where robust surface states are found for a system with in-plane anisotropy. One final restriction prevents the chirality from being too large with respect to the permittivity and permeability. In the uniaxial case for instance when $|\gamma| > \sqrt{\varepsilon_i \mu_r}$ all EFSs become either open or closed, and so the topologically non-trivial voids in $\boldsymbol{k}$-space vanish. Taking the example configuration used in Figure 4.6 and Figure 4.7, an upper limit on the chirality parameter $\gamma \approx 1.4$ can be found. However, since this boundary is already large compared to the

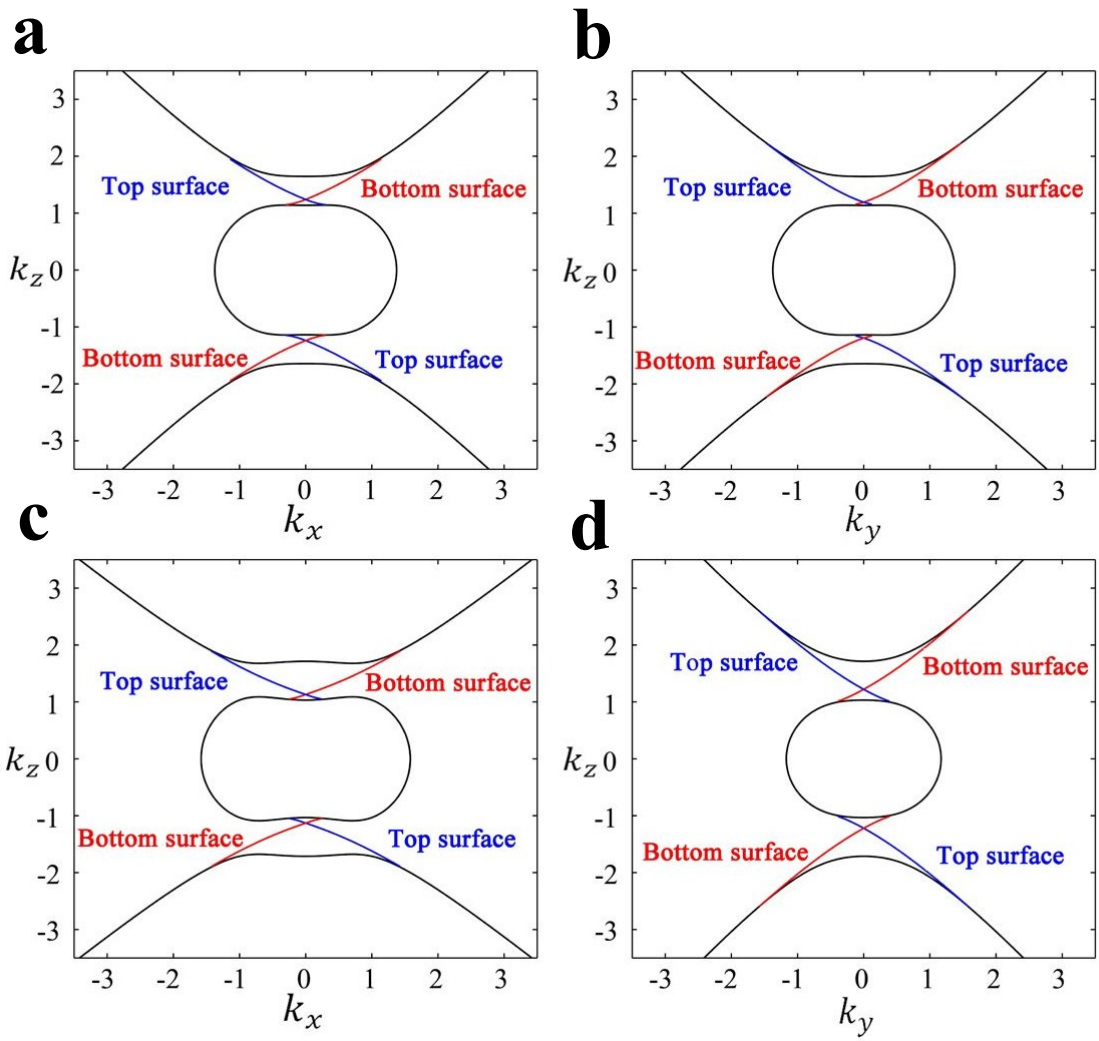

Figure 4.8: Non-trivial topology is preserved in hyperbolic chiral metamaterials with low symmetry. a, b Chirality in a single direction is sufficient to warrant the existence of nontrivial gaps and surface states. Here parameters are: ε=diag[4,4,-3], μ=0.5, γ=diag[0.5,0,0]. The topologically protected surface states are shown on both (a) x-z plane and (b) y-z plane. c, d Besides chirality in a single direction, in-plane anisotropy is further added to prove the robustness of the topology. The parameters are: ε=diag[3,5,-3], μ=0.5, γ=diag[0.5,0,0]. The topologically protected surface states are shown on both (c) x-z plane and (d) y-z plane.

magneto-electric coupling capabilities of most metamaterial designs we do not believe that it represents any real limitation upon the practicality of our scheme.

To complement our finding of nontrivial topology in chiral hyperbolic metamaterials it is instructive to look for effective metamaterial parameters that lead to topologically trivial, but still well separated, bound and unbound EFSs. For this we simply need to include magneto-electric coupling that lifts the degeneracy for waves propagating in the z direction

without introducing a rotationally dependant refractive index. Figure 4.9 reveals that these

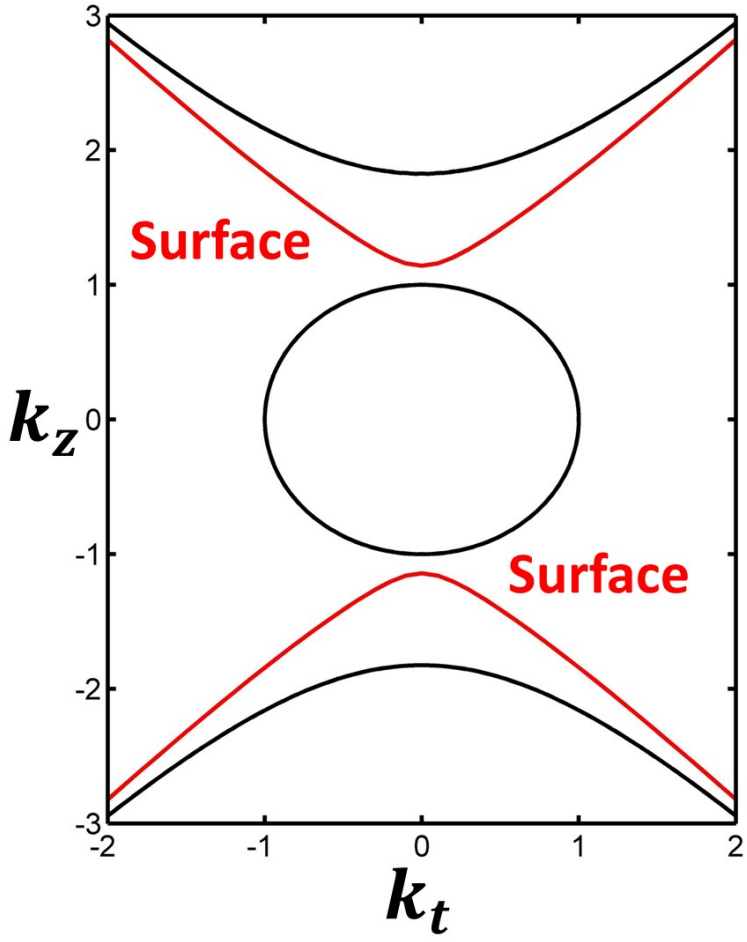

Figure 4.9: Bianisotropic, hyperbolic medium. Topologically trivial EFSs (C=0) result from the combination of bianisotropy and a hyperbolic permittivity tensor. Here parameters are: ε_r=diag[4,4,-3], μ_r=0.5, $\boldsymbol{\gamma_{xz} = -\gamma_{zx} = 1}$. Trivial surface states can be seen to originate from just one EFS, with left and right moving solutions coexisting on a single interface making them prone to scattering.

criteria can be satisfied by replacing chirality with bianisotropy, coupling E_x and H_x with H_z and E_z, respectively. In this case, surface states appear which are prone to scattering in contrast to the protected surface states found in Figs.4.6 and 4.8.

While this result may seem to imply that bianisotropic perturbations could cause backscattering of the surface states in a chiral hyperbolic medium, the topological nature of the chiral hyperbolic system guarantees that one-way surface states remain as long as the bulk EFSs stay separated. This is true provided that the chiral response is stronger than the bianisotropic response.

4.5: Topologically Non-trivial Microwave Metamaterials

Having outlined the prescription for non-trivial topology in a homogeneous medium based on the effective parameters, we now demonstrate the experimental feasibility of our scheme by designing realistic topological metamaterial structures. We choose to work in the microwave frequency regime as the lossless, dispersionless response of metals, which can be described as perfect electrical conductors (PEC), significantly simplifies the calculations. However, the design principles should remain the same for higher frequencies. From our effective medium treatment it is clear that the key ingredients for achieving topologically non-trivial EFSs are hyperbolicity and chirality, both of which have been dealt with extensively in the literature.

One thing that we have ignored up until now is the frequency dependence of the material parameters, which is usually critical in determining the behaviour of a photonic system. Fortunately, while gradients $\frac{\partial}{\partial \omega}$ appear in the energy density and can affect the overall wave amplitude, they play no part in controlling the relationship between the different fields. Therefore, dispersion is only important if we are concerned about the bandwidth of the response. We have already seen in (2.3.1/2) that a wire/plate structure behaves as an anisotropic Drude metal with $(\varepsilon_r > 0)$ for $\boldsymbol{E}$ fields perpendicular to the wires and $(\varepsilon_r < 0)$ for fields parallel to the wires, below a certain frequency. In (2.3.4) we also found that a coil geometry could produce strong optical activity, close to the resonant frequency, for waves incident perpendicular to its axis. Alongside the magneto-electric coupling, the presence of bright electric and magnetic dipoles also leads to Lorentzian Line shapes for the permittivity and permeability. We will therefore focus on frequencies below resonance to avoid $(\varepsilon_r < 0)$

and/or ($\mu_r < 0$). Combining these two structures with the coils aligned perpendicular to the wires should then reproduce the qualitative behaviour discovered with the effective medium calculations above.

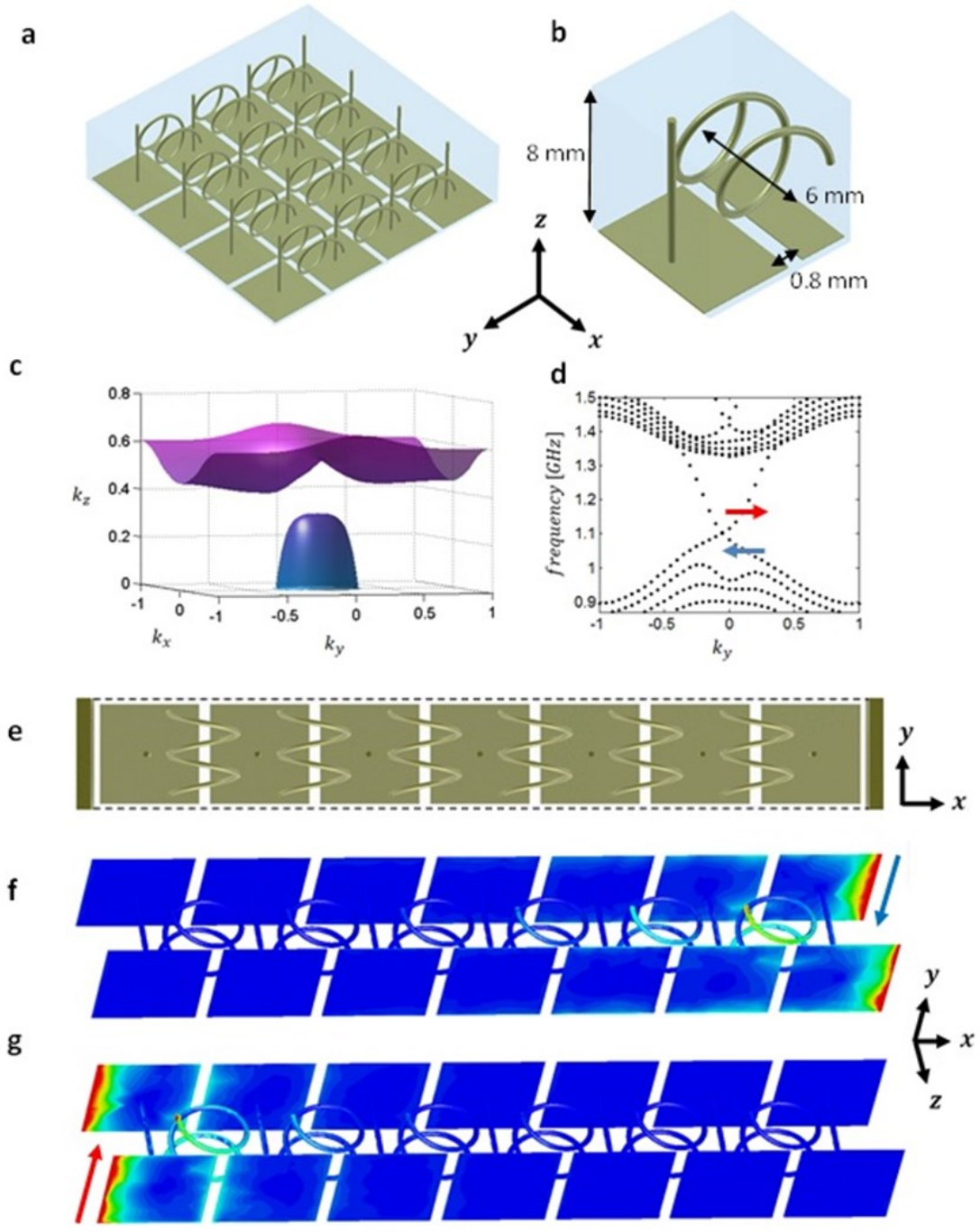

Figure 4.10: Topologically non-trivial EFS's for realistic metamaterial structure. a, b Simulated metamaterial structure with tilted view of lattice (a) and tilted view of single square unit cell (b) containing PEC wires and plates embedded in a dielectric medium, εr = 10.2, in which both straight and coiled wire radii are 0.2mm and the overall coil radius is 2.5mm. c. Calculated EFS's for structure shown in (a-b) at f = 1.1GHz, with k in units of π/d, where d is the unit cell period, revealing large topologically non-trivial gap (Δkz/kz ~ 0.3). d. Surface state dispersion for kz = 0.37π/d corresponding to supercell structure sandwiched between PEC walls shown in (e). f, g Surface state E-field patterns for ky = 0.1π/d, at f = 1.056 GHz (f) and f = 1.16 GHz (g), clearly showing that the surface modes are separated on different sides of the supercell.

By using the Eigenmode solver within CST MWS to calculate the eigenfrequencies for different boundary phase steps of a unit cell containing both the wire/plate structure and the coil structure, shown in Figure 4.10a-b, the bulk propagation characteristics of the proposed metamaterial can be investigated. In Figure 4.10c a large separation can be seen between EFS's associated with Bulk propagating modes with opposite helicities. Based On the analysis above we therefore expect this metamaterial design to support protected photonic surface states with wave vectors in the gap region.

To confirm the presence of topological order a supercell calculation involving six metamaterial unit cells contained within PEC walls, as shown in Figure 4.10e, has been performed with results presented in Figure 4.10d. Just two surface modes, isolated on opposite sides of the supercell as shown by Figure 4.10f-g, can be seen to traverse the bulk gap, signifying topological protection. Although the unit cell considered is much smaller than the free-space wavelength $\sim 25cm$ it is not deep subwavelength when compared to its wavelength inside the metamaterial, which may a cause non-local response. However, the strong optical activity originating from the coils still dominates, leading to opposite spin in the two bands in Figure 4.10c, as occurs in a completely homogeneous chirohyperbolic metamaterial. Therefore, the observation of topologically protected surface waves in this frequency regime also highlights the robustness of our scheme to non-local as well as local perturbations.

To demonstrate the versatility of the metamaterial approach to topological protection we can also design a chirohyperbolic structure with an indefinite magnetic rather than electric response, i.e. a diagonal permeability tensor with a single negative component. SRRs are typically employed for achieving $\mu < 0$. However, as explained in (2.3.3), such objects are also bianisotropic, due to the formation of an electric dipole moment in the gap, which is undesirable for our purpose. While a continuous ring only possesses a magnetic dipole, on the

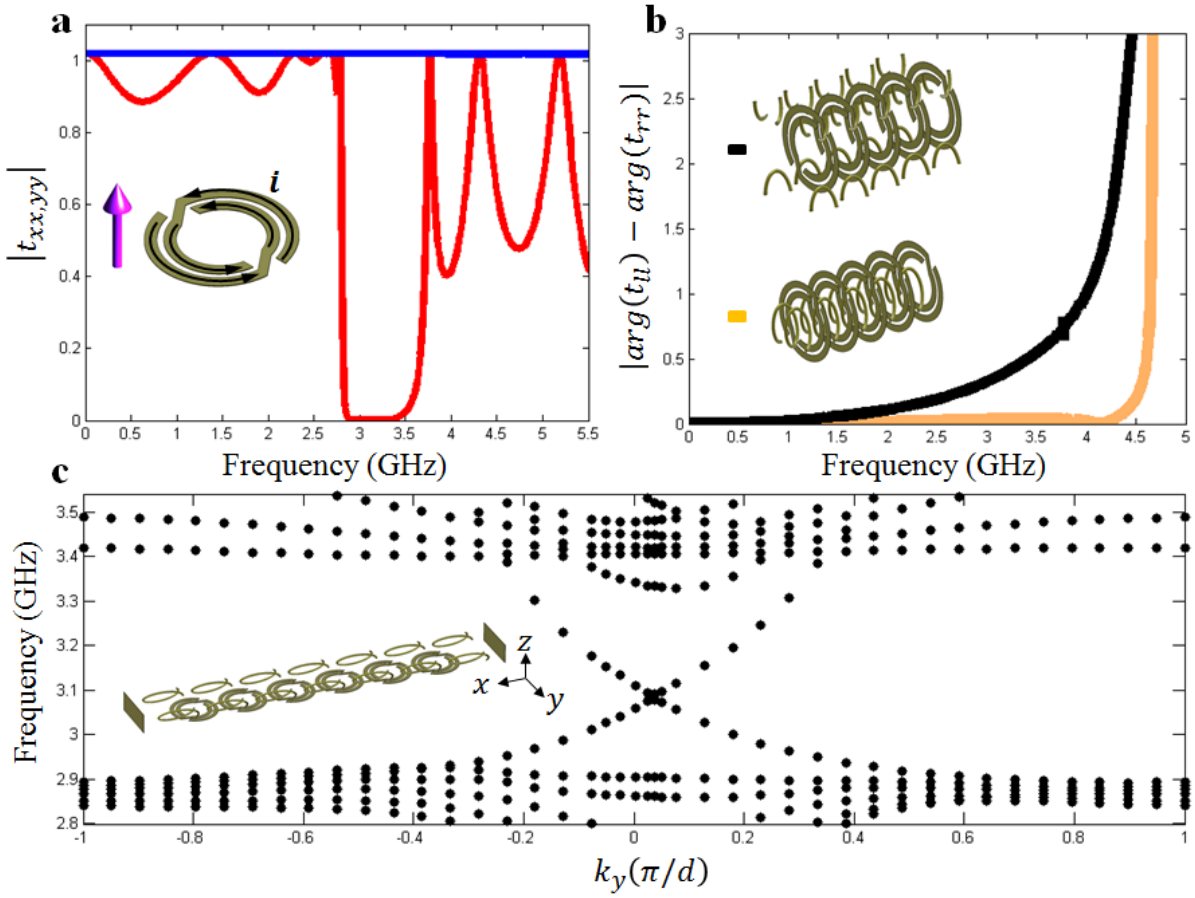

Figure 4.11: Topological metamaterial with hyperbolic permeability tensor. a) Linearly polarised transmission through 5 layer, non-bianisotropic SRR metamaterial. The wave is travelling in the plane of the rings with magnetic field aligned parallel (blue) and perpendicular (red) to this plane. b) Optical activity is suppressed when coils are centred on the SRRs. c) Surface wave dispersion for supercell shown within for $\boldsymbol{k_z = 0.227\pi/d}$.

subwavelength scale its interaction with radiation is too weak. Instead, the modified double loop design shown in Figure 4.11a has been used[*110*]. It can be seen that an incident wave experiences a stop-band around three GHz if the magnetic field is aligned with the ring axis but passes straight through otherwise. Chirality can then be once again introduced via the addition of springs, this time with a cylindrical geometry to provide a low resonant frequency whilst maintaining a small unit cell volume, preventing the SRR array from becoming too diluted which enhances the $\mu < 0$ bandwidth. As this new metamaterial contains two separate resonators, coupling is quite likely to occur. Figure 4.11b shows that this interaction can be minimised, leading to optical activity in the stop-band seen in Figure 4.11a, by placing the coils in-between the rings. Finally, the topologically non-trivial nature of this structure is

confirmed in Figure 4.11c with crossed surface states existing for a supercell contained within PEC walls. Based on the two very different examples that have been explored here, it should be possible to come up with many more designs which are suited to different fabrication processes and operating frequencies. Topological metamaterial investigations ought therefore to be well within reach of experimental verification.

4.6: Chapter Summary

In conclusion, we have theoretically demonstrated that a topologically nontrivial phase can exist without a spatially dependent optical potential in homogeneous photonic systems with completely local material properties. Although Ref [*100*] employs bianisotropic metamaterials to provide a spin-orbit interaction within a 2D photonic crystal, where nonlocality and the band structure play important roles, the resultant topological phase relies crucially on the isolated fourfold degeneracies that exist within permittivity and permeability matched photonic crystals with threefold rotational symmetry. In contrast, here we utilize an intrinsic form of spin-orbit interaction originating from the transversality of Maxwell's equations, with our metamaterial parameters chosen simply to separate out particular polarisation states in $\boldsymbol{k}$-space. While achieving bulk propagating modes with nontrivial topology in photonic crystals requires complicated arrangements of complex materials[*100*, *103*, *104*, *106*], here the nontrivial topology of our metamaterial is controlled by only a few effective material parameters, namely, the permittivity tensor and chirality. Importantly, hyperbolicity and chirality are responsible for protecting the edge states from backscattering, and so time-reversal symmetry does not need to be broken by using external magnetic fields; therefore, our design can be easily scaled to operate at any frequency. Since the building blocks of the topologically nontrivial metamaterial proposed here can be deep subwavelength, our work provides a platform for investigating highly confined topological

surface states and manipulating surface waves with potentially subwavelength resolution. Our numerical investigation into a realistic metamaterial structure clearly reveals topological behaviour in support of our initial effective medium approach; however, this is by no means the only or indeed optimal design for achieving a topological phase. In fact, the extremely large body of literature dealing with theoretical and experimental investigations of both hyperbolic metamaterials [*44*] and metamaterials with gigantic chirality [*55*, *56*, *58*], from microwave to optical frequencies, means that the experimental realization of metamaterial topological phases should be well within reach.

Chapter 5: Conclusion and Outlook

Despite the fact that human beings cannot directly perceive optical polarisation, it is one of the most widely known, best understood and technologically useful physical phenomenon known to science, finding applications in communications, imaging and even entertainment. These applications rely on birefringent materials to manipulate and detect polarised light. Recently, metamaterials have dramatically enhanced the range of properties available for such devices with much of the power behind these artificial structures stemming from their ability to couple selectively with arbitrary electric and/or magnetic field components. Even within a linear and completely homogeneous medium the most general light-matter interaction is described by a complex 6x6 polarisability tensor. There exists, therefore, a large number of possible degrees of freedom which, despite the control offered by metamaterials, has yet to be fully explored. The present thesis goes some way to addressing this, demonstrating that simply combining familiar properties together can result in surprising photonic phenomena. In particular, the role of subtle mathematical relationships, considered previously only for diffractive systems, on polarisation dependent plane wave propagation has been revealed.

Firstly, after outlining key background information, the transmission of THz radiation through metasurfaces composed of effective loss-gain dimer arrays was investigated. By exploiting the dependence of the near-field interaction between, and the far-field emission from, dipole antennas on the spatial configuration of a given metamolecule, variations in coupling strength have been shown to bring about polarisation phase transitions as a result of *PT* symmetry breaking. As well as dramatically altering the polarisation eigenstate evolution, i.e. a 45^{o} rotation of the trajectories on the Poincare sphere, the overlap between the eigenstates is proportional to the proximity of a system to the transition coordinate, known as

the exceptional point. Although the metasurfaces in question are non-Hermitian, the transmission of each normal mode can be described as the excitation of a simple Lorentzian dipole moment. Aside from providing a novel platform for studying *PT* symmetric physics, our artificial, anisotropically absorbing materials also, therefore, represent a method of realising effective, arbitrarily rotating dipole pairs. Control over polarisation eigenstates is becoming increasingly important in modern photonics research. Phase gradient metasurfaces for instance rely in a spatial variation of the local anisotropy to enable a range of functionalities, including beam steering, lensing and holography, with ultrathin devices. Hence, we believe the work presented here may open up new possibilities when incorporated into inhomogeneous systems.

The final part of chapter three explored the wider non-Hermitian parameter space surrounding an *EP* within the description of light transmitted through structures with anisotropic radiation efficiency. Specifically, the singular coordinate was shown to act as a topological monopole, leading to a geometric phase for a parametric circuit. Most interestingly, such a topological feature is robust to perturbations, which has allowed us to experimentally observe the associated phase singularity by varying the incident angle, despite the presence of imperfections in the sample fabrication and measurement setup. All experiments discussed in this thesis have been carried out using THz-TDS, agreeing well with the theoretical predictions.

In chapter four we looked into photonic wave solutions at the surfaces of Chiral-hyperbolic media. It was shown that these excitations are guaranteed to exist as they are a manifestation of the transition that must occur between two materials with topologically distinct bulk EFSs. Similarly to photonic and electronic crystal structures analysed by other groups, the boundary modes can only travel in one direction and are therefore

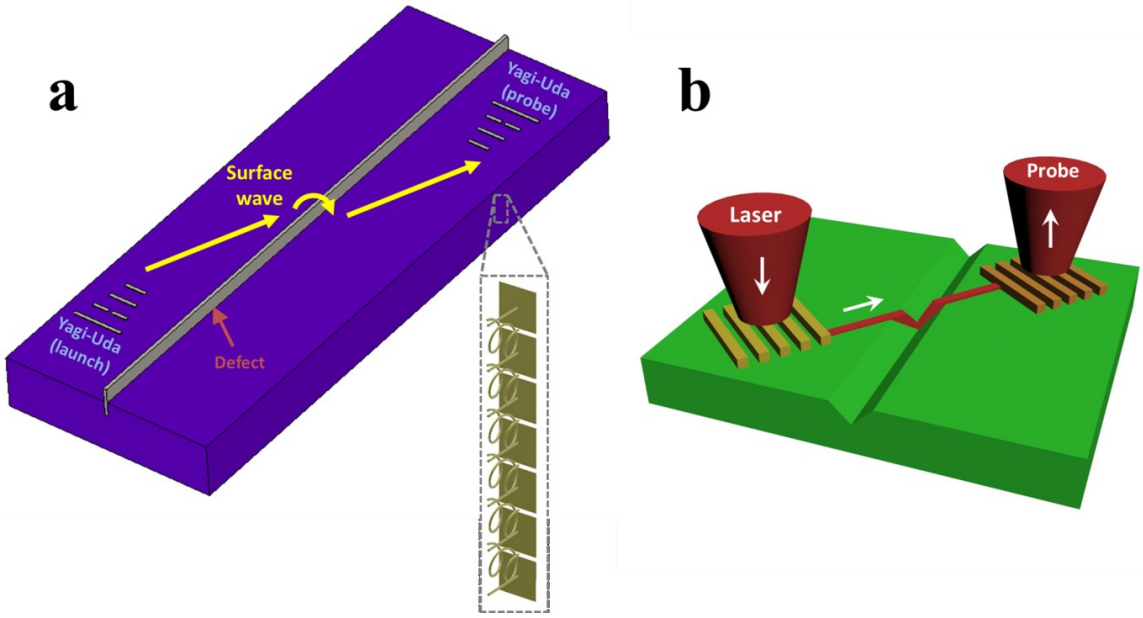

Figure 5.1: Schematics for experimentally observing topologically protected waves at the surfaces of chiral-hyperbolic metamaterials. a) Microwave setup using Yagi-Uda antennas to excite modes with a specified phase velocity. b) Optical setup using grating couplers.

robust against back-scattering from defects. Unlike photonic crystals however, the non-trivial bulk topology here arises from the inherent spin-orbit interaction, where spin=polarisation, coming from the transversality of light. Our approach is fundamentally unique in this sense as it requires no spatial variations of the fields. Consequently, chiral-hyperbolic metamaterials are not only attractive candidates for producing efficient guiding devices but may also represent an interesting platform for investigating new topological physics.

While the simulations included in (4.5) provide realistic designs for experimentally verifying our effective medium predictions at microwave frequencies, the need to isolate particular regions of reciprocal space, thus preventing the excitation of bulk waves, requires a field source to be carefully chosen. In the GHz regime, Yagi-Uda antennas directed along the $(\varepsilon, \mu < 0)$ axis and placed close to the metamaterial can be used to inject/detect modes with a particular range of phase velocities, as illustrated in Figure 5.1a. The presence of topological protection can then be probed by comparing the measured transmission efficiency across the

surface with and without a defect. Although designing and fabricating a chiral-hyperbolic medium to operate at optical frequencies would be more challenging, mainly because of the dispersive and lossy response of metals, we believe that it should still be possible due to the flexibility of the scheme. In this case, focussing a laser spot onto a metal grating of a specified period can excite a surface wave with a particular k, as illustrated in Figure 5.1b.

Furthermore, to date topological photonic investigations have remained limited to two dimensions or less, while a range of remarkable electronic properties have been revealed in 3D topological insulators. Realising such behaviour for electromagnetic waves will represent a new research direction and we believe that metamaterials in particular hold the key to this possibility.

To conclude, we note that the work presented here provides just a glimpse of the great richness of effective medium theory. Due to the freedom gifted by metamaterials, far from a simple probe, light has become a unique conceptual arena in its own right, suitable for playing out simple yet intriguing tales.

Bibliography

1. C. Carson, The origins of the quantum theory. *Beam Line*, 6–19 (2000).

2. J. B. Pendry, A. J. Holden, W. J. Stewart, I. Youngs, Extremely Low Frequency Plasmons in Metallic Mesostructures. *Phys. Rev. Lett.* **76**, 4773–4776 (1996).

3. J. B. Pendry, A. J. Holden, D. J. Robbins, W. J. Stewart, Magnetism from conductors and enhanced nonlinear phenomena. *IEEE Trans. Microw. Theory Tech.* **47**, 2075–2084 (1999).

4. D. R. Smith, D. R. Smith, W. J. Padilla, W. J. Padilla, D. C. Vier, D. C. Vier, S. C. Nemat-Nasser, S. C. Nemat-Nasser, S. Schultz, S. Schultz, Composite Medium with Simultaneously Negative Permeability and Permittivity. *Phys. Rev. Lett.* **84**, 4184–4187 (2000).

5. V. Veselago, Electrodynamics of Substances. *Sov. Phys. USPEKHI*. **10**, 509 (1968).

6. C. G. Parazzoli, R. B. Greegor, K. Li, B. E. C. Koltenbah, M. Tanielian, Experimental verification and simulation of negative index of refraction using Snell's law. *Phys. Rev. Lett.* **90**, 107401 (2003).

7. J. Nemirovsky, M. C. Rechtsman, M. Segev, Negative radiation pressure and negative effective refractive index via dielectric birefringence. *Opt. Express*. **20**, 8907 (2012).

8. S. Xi, H. Chen, T. Jiang, L. Ran, J. Huangfu, B. I. Wu, J. A. Kong, M. Chen, Experimental verification of reversed cherenkov radiation in Left-Handed metamaterial. *Phys. Rev. Lett.* **103**, 194801 (2009).

9. J. B. Pendry, Negative refraction makes a perfect lens. *Phys. Rev. Lett.* **85**, 3966–3969 (2000).

10. R. Shankar, *Principles of Quantum Mechanics* (Plenum Press, 1994).

11. M. V. Berry, Quantal Phase Factors Accompanying Adiabatic Changes. *Proc. R. Soc. A Math. Phys. Eng. Sci.* **392** (1984), pp. 45–57.

12. D. Xiao, M.-C. Chang, Q. Niu, Berry phase effects on electronic properties. *Rev. Mod. Phys.* **82**, 1959–2007 (2010).

13. C. Kittel, *Introduction to solid state physics* (Wiley, 2005).

14. J. Zak, Berry ' s Phase for Energy Bands in Solids given the adiabatic form. *Phys. Rev. Lett.* **62**, 2747–2750 (1989).

15. M. Z. Hasan, C. L. Kane, Colloquium: Topological insulators. *Rev. Mod. Phys.* **82**, 3045–3067 (2010).

16. K. V. Klitzing, G. Dorda, M. Pepper, New method for high-accuracy determination of the fine-structure constant based on quantized hall resistance. *Phys. Rev. Lett.* **45**, 494–497 (1980).

17. D. J. Thouless, M. Kohmoto, M. P. Nightingale, M. Den Nijs, Quantized hall conductance in a two-Dimensional periodic potential. *Phys. Rev. Lett.* **49**, 405–408 (1982).

18. C. L. Kane, E. J. Mele, Quantum Spin Hall Effect in Graphene. *Phys. Rev. Lett.* **95**, 226801 (2005).

19. C. L. Kane, E. J. Mele, Z_2 Topological Order and the Quantum Spin Hall Effect. *Phys. Rev. Lett.* **95**, 146802 (2005).

20. M. Konig, S. Wiedmann, C. Brune, A. Roth, H. Buhmann, L. W. Molenkamp, X.-L. Qi, S.-C. Zhang, Quantum Spin Hall Insulator State in HgTe Quantum Wells. *Science.* **318**, 766–770 (2007).

21. D. Hsieh, D. Qian, L. Wray, Y. Xia, Y. S. Hor, R. J. Cava, M. Z. Hasan, A topological Dirac insulator in a quantum spin Hall phase. *Nature*. **452**, 970–974 (2008).

22. A. M. Turner, A. Vishwanath, Beyond band insulators: Topology of semimetals and interacting phases. *Contemp. Concepts Condens. Matter Sci.* **6**, 293–324 (2013).

23. X. Wan, A. M. Turner, A. Vishwanath, S. Y. Savrasov, Topological semimetal and Fermi-arc surface states in the electronic structure of pyrochlore iridates. *Phys. Rev. B*. **83**, 205101 (2011).

24. F. D. M. Haldane, Attachment of Surface "Fermi Arcs" to the Bulk Fermi Surface: "Fermi-Level Plumbing" in Topological Metals (2014) (available at http://arxiv.org/abs/1401.0529).

25. C. M. Bender, S. Boettcher, Real Spectra in Non-Hermitian Hamiltonians Having PT Symmetry. *Phys. Rev. Lett.* **80**, 5243 (1998).

26. C. M. Bender, D. C. Brody, H. F. Jones, Complex extension of quantum mechanics. *Phys. Rev. Lett.* **89**, 270401 (2002).

27. J. D. Jackson, *Classical Electrodynamics Third Edition* (Wiley, 1998).

28. S. A. Maier, *Plasmonics: Fundamentals and applications* (Springer, 2007).

29. Y. Zhao, D. R. Grischkowsky, 2-D terahertz metallic photonic crystals in parallel-plate waveguides. *IEEE Trans. Microw. Theory Tech.* **55**, 656–663 (2007).

30. N. Laman, D. Grischkowsky, Terahertz conductivity of thin metal films. *Appl. Phys. Lett.* **93**, 051105 (2008).

31. C. Menzel, C. Rockstuhl, F. Lederer, Advanced Jones calculus for the classification of periodic metamaterials. *Phys. Rev. A*. **82**, 053811 (2010).

32. J. White, Surface Plasmon Polaritons, (available at http://large.stanford.edu/courses/2007/ap272/white1/).

33. M. I. D'yakonov, New type of electromagnetic wave propagating at an interface. *Sov Phys JETP*. **67**, 714–716 (1988).

34. O. Takayama, L. Crasovan, D. Artigas, L. Torner, Observation of Dyakonov Surface Waves. *Phys. Rev. Lett.* **102**, 043903 (2009).

35. P. A. Belov, R. Marques, S. I. Maslovski, I. S. Nefedov, M. Silverinha, C. R. Simovski, S. a. Tretyakov, Strong spatial dispersion in wire media in the very large wavelength limit. *Phys. Rev. B*. **67**, 113103 (2003).

36. J. B. Pendry, A. J. Holden, D. J. Robbins, W. J. Stewart, Low frequency plasmons in thin-wire structures. *J. Phys. Condens. Matter*. **10**, 4785–4809 (1998).

37. L. V. Alekseyev, V. A. Podolskiy, E. E. Narimanov, Homogeneous Hyperbolic Systems for Terahertz and Far-Infrared Frequencies. *Adv. Optoelectron.* **2012**, 1–6 (2012).

38. P. A. Belov, Y. Zhao, S. Tse, P. Ikonen, M. G. Silveirinha, C. R. Simovski, S. Tretyakov, Y. Hao, C. Parini, Transmission of images with subwavelength resolution to distances of several wavelengths in the microwave range. *Phys. Rev. B*. **77**, 193108 (2008).

39. A. Tuniz, K. J. Kaltenecker, B. M. Fischer, M. Walther, S. C. Fleming, A. Argyros, B. T. Kuhlmey, Metamaterial fibres for subdiffraction imaging and focusing at terahertz frequencies over optically long distances. *Nat. Commun.* **4**, 2706 (2013).

40. H. N. S. Krishnamoorthy, Z. Jacob, E. Narimanov, I. Kretzschmar, V. M. Menon, Topological Transitions in Metamaterials. *Science.* **336**, 205–209 (2012).

41. S. S. Baturin, A. D. Kanareykin, Cherenkov Radiation from Short Relativistic Bunches: General Approach. *Phys. Rev. Lett.* **113**, 214801 (2014).

42. J. Yao, Z. Liu, Y. Liu, Y. Wang, C. Sun, G. Bartal, A. M. Stacy, X. Zhang, Optical Negative Refraction in Bulk Metamaterials of Nanowires. *Science.* **321**, 930 (2008).

43. A. J. Hoffman, L. Alekseyev, S. S. Howard, K. J. Franz, D. Wasserman, V. A. Podolskiy, E. E. Narimanov, D. L. Sivco, C. Gmachl, Negative refraction in semiconductor metamaterials. *Nat. Mater.* **6**, 946–950 (2007).

44. A. Poddubny, I. Iorsh, P. Belov, Y. Kivshar, Hyperbolic metamaterials. *Nat. Photonics*. **7**, 948–957 (2013).

45. A. Demetriadou, J. B. Pendry, Taming spatial dispersion in wire metamaterial. *J. Phys. Condens. Matter*. **20**, 295222 (2008).

46. M. G. Silveirinha, A. B. Yakovlev, Negative refraction by a uniaxial wire medium with suppressed spatial dispersion. *Phys. Rev. B*. **81**, 233105 (2010).

47. V. M. Agranovich, Y. N. Gartstein, Electrodynamics of metamaterials and the Landau–Lifshitz approach to the magnetic permeability. *Metamaterials*. **3**, 1–9 (2009).

48. Y. Liu, X. Zhang, Metamaterials: a new frontier of science and technology. *Chem. Soc. Rev.* **40**, 2494–2507 (2011).

49. T. J. Yen, W. J. Padilla, N. Fang, D. C. Vier, D. R. Smith, J. B. Pendry, D. N. Basov, X. Zhang, Terahertz magnetic response from artificial materials. *Science*. **303**, 1494–1496 (2004).

50. S. Zhang, W. Fan, N. C. Panoiu, K. J. Malloy, R. M. Osgood, S. R. J. Brueck, Experimental Demonstration of Near-Infrared Negative-Index Metamaterials. *Phys. Rev. Lett.* **95**, 137404 (2005).

51. C. M. Soukoulis, M. Wegener, Past achievements and future challenges in the development of three-dimensional photonic metamaterials. *Nat. Photonics*. **5**, 523–530 (2011).

52. N. Katsarakis, T. Koschny, M. Kafesaki, E. N. Economou, C. M. Soukoulis, Electric coupling to the magnetic resonance of split ring resonators. *Appl. Phys. Lett.* **84**, 2943–2945 (2004).

53. A. Schneider, A. Shuvaev, S. Engelbrecht, S. O. Demokritov, A. Pimenov, Electrically Excited Inverse Electron Spin Resonance in a Split-Ring Metamaterial Resonator. *Phys. Rev. Lett.* **103**, 103907 (2009).

54. H. D. Flack, Louis Pasteurs discovery of molecular chirality and spontaneous resolution in 1848, together with a complete review of his crystallographic and chemical work. *Acta Crystallogr. Sect. A Found. Crystallogr.* **65**, 371–389 (2009).

55. S. Zhang, Y. Park, J. Li, X. Lu, W. Zhang, X. Zhang, Negative Refractive Index in Chiral Metamaterials. *Phys. Rev. Lett.* **102**, 023901 (2009).

56. Z. Li, M. Mutlu, E. Ozbay, Chiral metamaterials: from optical activity and negative refractive index to asymmetric transmission. *J. Opt.* **15**, 023001 (2013).

57. J. B. Pendry, A chiral route to negative refraction. *Science*. **306**, 1353–1355 (2004).

58. E. Plum, J. Zhou, J. Dong, V. A. Fedotov, T. Koschny, C. M. Soukoulis, N. I. Zheludev, Metamaterial with negative index due to chirality. *Phys. Rev. B*. **79**, 035407 (2009).

59. A. V. Rogacheva, V. A. Fedotov, A. S. Schwanecke, N. I. Zheludev, Giant Gyrotropy due to Electromagnetic-Field Coupling in a Bilayered Chiral Structure. *Phys. Rev. Lett.* **97**, 177401 (2006).

60. T.-T. Kim, S. S. Oh, H.-S. Park, R. Zhao, S.-H. Kim, W. Choi, B. Min, O. Hess, Optical Activity Enhanced by Strong Inter-molecular Coupling in Planar Chiral Metamaterials. *Sci. Rep.* **4**, 5864 (2014).

61. V. A. Fedotov, P. L. Mladyonov, S. L. Prosvirnin, A. V. Rogacheva, Y. Chen, N. I. Zheludev, Asymmetric Propagation of Electromagnetic Waves through a Planar Chiral Structure. *Phys. Rev. Lett.* **97**, 167401 (2006).

62. E. Prodan, C. Radloff, N. J. Halas, P. Nordlander, A hybridization model for the plasmon response of complex nanostructures. *Science*. **302**, 419–422 (2003).

63. H. Liu, D. A. Genov, D. M. Wu, Y. M. Liu, Z. W. Liu, C. Sun, S. N. Zhu, X. Zhang, Magnetic plasmon hybridization and optical activity at optical frequencies in metallic nanostructures. *Phys. Rev. B*. **76**, 073101 (2007).

64. B. Luk'yanchuk, N. I. Zheludev, S. A. Maier, N. J. Halas, P. Nordlander, H. Giessen, C. T. Chong, The Fano resonance in plasmonic nanostructures and metamaterials. *Nat. Mater.* **9**, 707–715 (2010).

65. A. B. Khanikaev, C. Wu, G. Shvets, Fano-resonant metamaterials and their applications. *Nanophotonics*. **2**, 247–264 (2013).

66. S. Zhang, D. A. Genov, Y. Wang, M. Liu, X. Zhang, Plasmon-Induced Transparency in Metamaterials. *Phys. Rev. Lett.* **101**, 047401 (2008).

67. R. Taubert, M. Hentschel, J. Kästel, H. Giessen, Classical analog of electromagnetically induced absorption in plasmonics. *Nano Lett.* **12**, 1367–1371 (2012).

68. S. Zhang, Z. Ye, Y. Wang, Y. Park, G. Bartal, M. Mrejen, X. Yin, X. Zhang, Anti-Hermitian Plasmon Coupling of an Array of Gold Thin-Film Antennas for Controlling Light at the Nanoscale. *Phys. Rev. Lett.* **109**, 193902 (2012).

69. M. Lawrence, N. Xu, X. Zhang, L. Cong, J. Han, W. Zhang, S. Zhang, Manifestation of PT Symmetry Breaking in Polarization Space with Terahertz Metasurfaces. *Phys. Rev. Lett.* **113**, 093901 (2014).

70. A. Guo, G. J. Salamo, D. Duchesne, R. Morandotti, M. Volatier-Ravat, V. Aimez, G. A. Siviloglou, D. N. Christodoulides, Observation of PT-Symmetry Breaking in Complex Optical Potentials. *Phys. Rev. Lett.* **103**, 093902 (2009).

71. C. E. Rüter, K. G. Makris, R. El-ganainy, D. N. Christodoulides, M. Segev, D. Kip, Observation of parity–time symmetry in optics. *Nat. Phys.* **6**, 192–195 (2010).

72. Z. Lin, H. Ramezani, T. Eichelkraut, T. Kottos, H. Cao, D. N. Christodoulides, Unidirectional Invisibility Induced by PT-Symmetric Periodic Structures. *Phys. Rev. Lett.* **106**, 213901 (2011).

73. L. Feng, Y.-L. Xu, W. S. Fegadolli, M.-H. Lu, J. E. B. Oliveira, V. R. Almeida, Y.-F. Chen, A. Scherer, Experimental demonstration of a unidirectional reflectionless parity-time metamaterial at optical frequencies. *Nat. Mater.* **12**, 108–113 (2012).

74. S. Longhi, Bloch Oscillations in Complex Crystals with PT Symmetry. *Phys. Rev. Lett.* **103**, 123601 (2009).

75. H. Alaeian, J. A. Dionne, Parity-time-symmetric plasmonic metamaterials. *Phys. Rev. A*. **89**, 033829 (2014).

76. K. G. Makris, R. El-Ganainy, D. N. Christodoulides, Z. H. Musslimani, Beam Dynamics in PT Symmetric Optical Lattices. *Phys. Rev. Lett.* **100**, 103904 (2008).

77. A. Regensburger, C. Bersch, M.-A. Miri, G. Onishchukov, D. N. Christodoulides, U. Peschel, Parity–time synthetic photonic lattices. *Nature*. **488**, 167–171 (2012).

78. S. Longhi, PT-symmetric laser absorber. *Phys. Rev. A*. **82**, 031801 (2010).

79. H. Hodaei, M.-A. Miri, M. Heinrich, D. N. Christodoulides, M. Khajavikhan, Parity-time-symmetric microring lasers. *Science.* **346**, 975–978 (2014).

80. S. Pancharatnam, The propagation of light in absorbing biaxial crystals — I. Theoretical. *Proc. Ind. Acad. Sci. A*. **42**, 86–109 (1955).

81. S. Pancharatnam, The propagation of light in absorbing biaxial crystals — II. Experimental. *Proc. Ind. Acad. Sci. A*. **XLII**, 235–248 (1955).

82. C. Dembowski, B. Dietz, H.-D. Gräf, H. L. Harney, A. Heine, W. D. Heiss, A. Richter, Observation of a Chiral State in a Microwave Cavity. *Phys. Rev. Lett.* **90**, 034101 (2003).

83. C. Dembowski, H.-D. Gräf, H. L. Harney, A. Heine, W. D. Heiss, H. Rehfeld, A. Richter, Experimental Observation of the Topological Structure of Exceptional Points. *Phys. Rev. Lett.* **86**, 787–790 (2001).

84. C. Dembowski, B. Dietz, H.-D. Gräf, H. L. Harney, A. Heine, W. D. Heiss, A. Richter, Encircling an exceptional point. *Phys. Rev. E*. **69**, 056216 (2004).

85. Guide to Vector Version (sspropv, sspropvc), (available at http://www.photonics.umd.edu/software/ssprop/vector-version/).

86. Z. Li, M. Gokkavas, E. Ozbay, Manipulation of Asymmetric Transmission in Planar Chiral Nanostructures by Anisotropic Loss. *Adv. Opt. Mater.* **1**, 482–488 (2013).

87. J. Gu, R. Singh, X. Liu, X. Zhang, Y. Ma, S. Zhang, S. A. Maier, Z. Tian, A. K. Azad, H.-T. Chen, A. J. Taylor, J. Han, W. Zhang, Active control of electromagnetically induced transparency analogue in terahertz metamaterials. *Nat. Commun.* **3**, 1151 (2012).

88. X. Yin, M. Schäferling, B. Metzger, H. Giessen, Interpreting chiral nanophotonic spectra: The plasmonic Born-Kuhn model. *Nano Lett.* **13**, 6238–6243 (2013).

89. A. I. Nesterov, F. Aceves de la Cruz, Complex magnetic monopoles, geometric phases and quantum evolution in the vicinity of diabolic and exceptional points. *J. Phys. A Math. Theor.* **41**, 485304 (2008).

90. V. G. Kravets, F. Schedin, R. Jalil, L. Britnell, R. V Gorbachev, D. Ansell, B. Thackray, K. S. Novoselov, A. K. Geim, A. V Kabashin, A. N. Grigorenko, Singular phase nano-optics in plasmonic metamaterials for label-free single-molecule detection. *Nat. Mater.* **12**, 304–309 (2013).

91. H.-X. Cui, X.-W. Cao, M. Kang, T.-F. Li, M. Yang, T.-J. Guo, Q.-H. Guo, J. Chen, Exceptional points in extraordinary optical transmission through dual subwavelength metallic gratings. *Opt. Express*. **21**, 13368–79 (2013).

92. M. Kang, H.-X. Cui, T.-F. Li, J. Chen, W. Zhu, M. Premaratne, Unidirectional phase singularity in ultrathin metamaterials at exceptional points. *Phys. Rev. A*. **89**, 065801 (2014).

93. L. Feng, X. Zhu, S. Yang, H. Zhu, P. Zhang, Demonstration of a large-scale optical exceptional point structure. *Opt. Express*. **22**, 1760–1767 (2014).

94. W. Gao, M. Lawrence, B. Yang, F. Liu, F. Fang, B. Béri, J. Li, S. Zhang, Topological Photonic Phase in Chiral Hyperbolic Metamaterials. *Phys. Rev. Lett.* **114**, 037402 (2015).

95. J. J. D. Joannopoulos, S. Johnson, J. N. J. Winn, R. R. D. Meade, *Photonic crystals: molding the flow of light* (Princeton University Press, 2008).

96. T. F. Krauss, R. M. De La Rue, S. Brand, Two-dimensional photonic-bandgap structures operating at near-infrared wavelengths. *Nature*. **383**, 699–702 (1996).

97. T. F. Krauss, R. M. De La Rue, Photonic crystals in the optical regime - past, present and future. *Prog. Quantum Electron.* **23**, 51–96 (1999).

98. F. D. M. Haldane, S. Raghu, Possible Realization of Directional Optical Waveguides in Photonic Crystals with Broken Time-Reversal Symmetry. *Phys. Rev. Lett.* **100**, 013904 (2008).

99. Z. Wang, Y. Chong, J. D. Joannopoulos, M. Soljacić, Observation of unidirectional backscattering-immune topological electromagnetic states. *Nature*. **461**, 772–775 (2009).

100. A. B. Khanikaev, S. Hossein Mousavi, W.-K. Tse, M. Kargarian, A. H. MacDonald, G. Shvets, Photonic topological insulators. *Nat. Mater.* **12**, 233–239 (2012).

101. W.-J. Chen, S.-J. Jiang, X.-D. Chen, B. Zhu, L. Zhou, J.-W. Dong, C. T. Chan, Experimental realization of photonic topological insulator in a uniaxial metacrystal waveguide. *Nat. Commun.* **5**, 5782 (2014).

102. K. Fang, Z. Yu, S. Fan, Realizing effective magnetic field for photons by controlling the phase of dynamic modulation. *Nat. Photonics*. **6**, 782–787 (2012).

103. M. C. Rechtsman, J. M. Zeuner, Y. Plotnik, Y. Lumer, D. Podolsky, F. Dreisow, S. Nolte, M. Segev, A. Szameit, Photonic Floquet topological insulators. *Nature*. **496**, 196–200 (2013).

104. M. Hafezi, S. Mittal, J. Fan, A. Migdall, J. M. Taylor, Imaging topological edge states in silicon photonics. *Nat. Photonics*. **7**, 1001–1005 (2013).

105. L. Lu, L. Fu, J. D. Joannopoulos, M. Soljačić, Weyl points and line nodes in gyroid photonic crystals. *Nat. Photonics*. **7**, 294–299 (2013).

106. L. Lu, J. D. Joannopoulos, M. Soljačić, Topological photonics. *Nat. Photonics*. **8**, 821–829 (2014).

107. A. Tomita, R. Y. Chiao, Observation of Berry's Topological Phase by Use of an Optical Fiber. *Phys. Rev. Lett.* **57**, 937–940 (1986).

108. K. Y. Bliokh, A. Niv, V. Kleiner, E. Hasman, Geometrodynamics of Spinning Light. *Nat. Photonics*. **2**, 749–753 (2008).

109. K. Y. Bliokh, A. Aiello, Goos–Hänchen and Imbert–Fedorov beam shifts: an overview. *J. Opt.* **15**, 014001 (2013).

110. M. Durán-Sindreu, J. Naqui, F. Paredes, J. Bonache, F. Martín, Electrically Small Resonators for Planar Metamaterial, Microwave Circuit and Antenna Design: A Comparative Analysis. *Appl. Sci.* **2**, 375–395 (2012).

111. mathematics illuminated, (available at http://www.learner.org/courses/mathilluminated/images/units/4/1614.png).

112. E. J. Kane, C. L. Mele, A New Spin on the Insulating State. *Science.* **314**, 1692–1693 (2006).

113. Chirality. *Wikipedia*, (available at http://en.wikipedia.org/wiki/Chirality).

114. S. Smiley, 3 Guidlines For Choosing a Passive UHF RFID Antenna. *RFIDinsider*, (available at http://blog.atlasrfidstore.com/choose-right-rfid-antenna).

115. T. Kottos, Optical physics: Broken symmetry makes light work. *Nat. Phys.* **6**, 166–167 (2010).